Preliminary Design of an eVTOL Aircraft
(Versão final após defesa)

Marcos Filipe Andrade Nunes Rosa

Dissertação para obtenção do Grau de Mestre em
Engenharia Aeronáutica
(Mestrado Integrado)

Orientador: Prof. Doutor Miguel Ângelo Rodrigues Silvestre

Agosto de 2022

Acknowledgments

First of all, I would like to thank my supervisor, Professor Miguel Ângelo Silvestre, for all the teachings, incentives, corrections and overall support through all phases of this dissertation.

I would like to thank my colleague, Engineer Renato Machado, for the knowledge sharing and assistance.

I would also like to thank my girlfriend Alice and my friends João, Wagner, Marco, Nuno, for the assistance and motivation you guys provided me in this journey.

I would express my gratitude to my Godfather Agostinho Alberto and my grandmother Leonor Tavares, for the dedication and support . A special thank you to my parents, Osório Rosa and Albertina Andrade, for their dedication throughout my life, for providing me with education and for always inspiring and supporting me throughout life and associated challenges.

Resumo

O crescimento no incentivo de fontes de energia descarbonizada na indústria da aviação civil, desde a aviação de transporte até vigilância, leva a que novos conceitos de aeronaves sejam desenvolvidos para uma gama diferente de aplicações futuras e actuais como substuição de conceitos ultrapassados de aeronaves ainda em uso. A electrificação é o futuro para propulsão de aeronaves. A aeronave do tipo eléctrico com descolagem e aterragem vertical (eVTOL) tem amadurecido como alternativa para Mobilidade Aérea Urbana (MAU), no transporte de mercadorias e passageiros para curto e médio alcance.

Nesta dissertação, é proposto um projeto conceptual e preliminar de uma aeronave eVTOL. O design é um pequeno UAV otimizado para maximizar uma função objetivo, $F_{obj} = m_{pay} \frac{C_L}{C_D}$ para um maior alcance e capacidade de carga. Utilizou-se uma folha de cálculo Excel para fazer um estudo paramétrico da asa com a envergadura, corda aerodinâmica média (CAM) e coeficiente de sustentação como principais parâmetros de projeto da asa da aeronave. Foram testadas múltiplas combinações dos parâmetros e os critérios de seleção foram a função objetivo e CAM. Um compromisso entre os dois critérios foi alcançado ao selecionar uma asa com uma pontuação um pouco menor na função objetivo, mas um valor de CAM superior à corda ótima, isso foi a melhor escolha para a estrutura. O Prop Selector foi utilizado em combinação com a folha de cálculo para o projeto preliminar da hélice, implementou-se uma configuração de passo variável com as características principais da asa já conhecida. Estudou-se o desempenho da aeronave em condições de voo pairado e cruzeiro para selecionar o melhor diâmetro da hélice com os critérios desempenho da eficiência de tração em voo pairado (H) e efficiência global (η_{global}) para quantificar o passo apropriado a cada condição de voo e apurar a previsão do desempenho global da aeronave.

A previsão de desempenho, razão de subida, velocidade de cruzeiro, e alcance, revelou resultados promissores. O software XFOIL/XFLR5 foi utilizado para estudar a estabilidade longitudinal estática, e em seguida desenhou-se com Open VSP e CATIA V5 modelos CAD da aeronave e do mecanismo basculante dos rotores. Finalmente, foi feito o perfil da missão, em que é de interesse a fração de massa da bateria, e o consumo de energia para cada condição de voo, e com essas métricas as capacidades e limitações da aeronave são reconhecidas.

Palavras-chave

eVTOL, Projecto Preliminar, Asa Fixa, MAU, UAV, hélice de passo variável

Abstract

The growing demand for alternative clean energy sources for civil aviation industry, from transport to surveillance, prompts new aircraft configurations for a different range of future applications and replacement of outdated concepts of aircraft still in service. The electrification of aircraft is the future of aviation. The electrical Vertical Take-off and Landing (eVTOL) type of aircraft is growing in demand as an alternative for Urban Air Mobility (UAM), in short to mid-range transportation of goods and passengers.

In this dissertation, an eVTOL aircraft concept and preliminary design are proposed. The design is a small UAV optimized for $m_{pay} \frac{C_L}{C_D}$ aiming at longer flight ranges and carrying capacity. An Excel spreadsheet developed to proceed with the parametric study. The parameters considered are: Winspan, mean aerodynamic chord (MAC), and lift coefficient as the main design parameters for the aircraft wing. Multiple parameters combinations were tested and the selection criteria were the objective function and MAC. A compromise between the two criteria was achieved by selecting a wing with a slightly less score in objective function but a mean chord value higher than the optimal chord, which was better for the structure. Prop Selector was used in combination with spreadsheets for the preliminary propeller design, where a variable pitch configuration with the known wing main characteristics was adopted, in hover and cruise conditions to screen the best propeller diameter using the hover lift performance (H) and global efficiency (η_{global}) as the main performance parameters do optimize the propulsion of the aircraft. The selected diameter is studied in the climb condition and the ideal pitch of the propeller is predicted for the relevant flight conditions.

The performance parameters such as the rate of climb, cruise speed, and range were estimated, showing promising results. With XFOIL/XFLR5 software the static longitudinal stability was studied, and Open VSP and CATIA V5 CAD models of the aircraft, and tilt-rotor mechanism were made. Finally, the mission profile is devised, the battery mass fraction, and energy consumption for each flight condition is calculated, thus highlighting the capabilities and limitations of the aircraft.

Keywords

Contents

List of Figures

List of Tables

Acronyms

AOA	Angle of Attack
CAD	Computer Aided Design
CS	Certification Specifications
DMT	Actuator Disc Momentum Theory
DEP	Distributed Electric Propulsion
EASA	European Union Aviation Safety Agency
ESC	Electronic Speed Controller
FAA	Federal Aviation Agency
FW	Fixed Wing
MAC	Mean Aerodynamic Chord
NASA	National Aviation Space Agency
OEM	Original Equipment Manufacturer
PMS	Power Management System
RPM	Rotation per Minute
UAM	Urban Air Mobility
UAV	Unmanned Aircraft Vehicle
eVTOL	Electric Vertical Take-off and Landing
UBI	Universidade da Beira Interior
WTT	Wing Tip Tail

Nomeclature

Roman Symbols

$A[m^2]$	Rotor Disc Area
AR	Wing Aspect of Ratio
$b[m]$	Main Wing span
$b_{ref}[m]$	Reference wingspan
$c[m]$	Main Wing mean Chord
$C[kg/(kWh)]$	Specific Fuel Consumption
C_d	Drag Coefficient per unit Span
C_D	Drag Coefficient
C_{D_i}	Induced Drag Coefficient
C_{D_0}	Parasite Drag Coefficient
$C_{D_{foil}}$	Wing Drag Coefficient
$C_{D_{emp}}$	Tail Drag Coefficient
$C_{D_{fuse}}$	Fuselage Drag Coefficient
$C_{D_{0Resto}}$	Remaining Profile Drag Drag Coefficient
C_{D_V}	Volumetric Drag Coefficient
C_f	Friction Coefficient
C_l	Lift Coefficient per unit Span
C_L	Lift Coefficient
Cm	Pitching Moment Coefficient
C_P	Power Coefficient
$c_{ref}[m]$	Reference mean aerodynamic chrod
C_T	Thrust Coefficient
$D[N]$	Drag
$D_i[N]$	Induced Drag
$D_0[N]$	Parasite Drag
$D[cm]$	Disc Diameter
$e[cm]$	Oswald Factor
$E[min]$	Endurance
e_b	Non-linear Wingspan Exponent
e_c	Non-linear mean aerodynamic chord Exponent
$E_{con}[J]$	Energy consumption
E_{con}/E_{conT}	Energy consumption ratio
$E_s[Wh/kg]$	Battery Specific Energy
Fc_{var}	Chord Variation from the optimal chord
FF	Form Factor
$Floss_{opt}$	Objective Function difference from the optimal
$F_{obj}[kg]$	Objective Function
FOM	Figure of Merit
$H[N/kW]$	Hover Lift Performance
$I[A]$	Current

$I_0[A]$	Load Current
$I_{max}[A]$	Maximum Current
k	Lift Induced Drag Factor
$k_v[RPM/V]$	Specific Constant Velocity
l_f/d_f	Fineness Ratio
$L[N]$	Lift
$\dfrac{L}{D}$	Lift to Drag Ratio
$MTOM[kg]$	Maximum Take-off Mass
$m_{Bat}[kg]$	Battery Mass
$m_{ref}[kg]$	Reference Airplane Structure Mass
$m_{sys}[kg]$	Systems Mass
m_{bat}/m_{MTOM}	Battery Mass Fraction
m_{batcr}/m_{MTOM}	Battery Mass Fraction for Cruise
$m_{container}[kg]$	Container Mass
$m_{MTOW}[kg]$	Maximum Take-off Weight Mass
n	Load Factor
$P[W]$	Actual Power
$P_b[cm]$	Blade Pitch
$P_i[W]$	Induced Power
$P_{shaft}[W]$	Shaft Power
$P_{motor}[W]$	Motor Power
$P_r[W]$	Power Required
$P_a[W]$	Power Available
$q[Pa]$	Dynamic Pressure
$Q[Nm]$	Momentum Torque
$R[km]$	Range
$R[cm]$	Rotor Radius; Length of the Blade
$Re\sqrt{C_L}$	Reduced Reynolds
$ROC[m]$	Rate of Climb
$S[m^2]$	Planform Wing Area
$T[N]$	Thrust
$T/A[N/M^2]$	Rotor Disc Loading
$U_{nom}[V]$	Nominal Voltage
$U_{Bat}[V]$	Battery Voltage
$V[m/s]$	Airspeed
$v_i[m/s]$	Rotor Induced Velocity
$v_h[m/s]$	Velocity in Hover
$w[m/s]$	Rotor Induced Velocity in the far Wake
$v_s[m/s]$	Stall Speed
$v_{max}[m/s]$	Maximum Speed
$v_{cr}[m/s]$	Velocity in cruise
$v_{cl}[m/s]$	Velocity in Climb
$W_0[N]$	Initial Take-off Weight
$W_1[N]$	Final Weight

Greek Symbols

$\alpha[deg]$	Angle of Attack
$\alpha_0[deg]$	Zero Lift Angle of Attack
$\beta[deg]$	Blade Flap Angle
δ	Voltage from ESC
$\eta_{bat}[V]$	Battery Voltage Efficiency
η_m	Mechanical Efficiency
η_p	Propeller Efficiency
η_{global}	Global Efficiency
$\theta[deg]$	Pitch Angle
λ	Taper Ratio
$\mu[kg/(ms)]$	Fluid Viscosity
π	pi
$\rho[kg/m^3]$	Air Density
σ_s	Rotor Solidity
$\phi[deg]$	Roll or Bank Angle
$\gamma_c[deg]$	Climb Angle
$\gamma_d[deg]$	Descent or Glide Angle
$\psi[deg]$	Azimuth Angle of Blade
$\omega_{shaft}[rad/s]$	Shaft Rotation Speed
$\omega_{motor}[rad/s]$	Motor Rotation Speed
Ω	Non-Dimensional Rotor Speed

Chapter 1

Introduction

1.1 Motivation

In recent years the demand for electric propulsion and low to zero carbon emissions energy sources is growing in the aviation, automobile, and other engineering fields.

Urbain Air Mobility(UAM) is being discussed moreover as a solution to the issue of automobile traffic, specifically, over high-density and major cities, as alternative for fast transport in short-mid range flights for few passengers seat or cargo. A compromise between fewer carbon emissions aircraft and a UAM environment has pointed out the need to develop new alternative aircraft configurations. Henceforth, some experts in the aviation industry and companies expect the eVTOL to be a promising solution for the issues mentioned. Moreover, investment is being made in projects for eVTOL aircraft as it becomes a growing trend [1, 2].

The global market for eVTOL aircraft was estimated to be USD 8.5 billion in 2021, projected to reach USD 30.8 billion by the year 2030 [3]. The growth of eVTOL applicability is expected to increase as more breakthrough in the reliability of renewable energies succeeds. Specifically, as the battery enhancements come forth to improve stability, durability and higher energy density or the development of other renewable energy alternatives as hydrogen and even fusion nuclear energy. One deterrent to eVTOL growth lies in the certification, license and a clear EASA regulations or FAA regulations developed for the operation of this aircraft[2].

 The driving growth of projects and newer concepts in recent years for this concept lies in how promising the applications for this type of aircraft with featured capabilities in terms of clearance, noise and green energy use. The technology is still in recent development since most examples of this aircraft in the market under application are small UAVs, such as the Tron F90, for surveillance and transport with an MTOM lower than 50kg. The larger eVTOL are usually reliant on hybrid propulsion, utilizing fuel cells and batteries for the sustainability of flight. Moreover, most products under recreation operations have a passenger limit of one or two, Kitty Hawk Cora, and Blackfly alike are examples. Another ambitious project is the Lilium Jet which intends to carry six passengers with a fair range capability.

Companies such as Uber, Bell, Boeing, NASA, Airbus, Rolls Royce, E-Hang, and others are competing for the future market share of these aircraft. Investment and limited

certifications for operations exist mostly in North America and China. As time and space are allowed, eventually, the public opinion about the reliability and demand for this type of aircraft is coming worldwide. Subsequently, advancements and technology refinement will help for future implementation in a broader global scale environment. Altogether, eVTOL is one of the most prominent aircraft configurations with the prospect of replacing helicopters in short- mid-range transportation, specifically for the UAM application, since helicopters are not a suitable alternative. Henceforth, developments and studies of this aircraft are needed for this prospect to become a reality in the next decades.

1.2   Objectives

The main objective is to introduce an new preliminary design of an eVTOL aircraft, to become a UAV product with a take-off mass close to 10kg or even a scaled-down prototype for UAM application.

Select an apropriate affordable brushless motor for this eVTOL is also intended and to give a special focus into the propeller by selecting the most suitable diameter and studying the variable pitch propeller behaviour for the hover, climb and cruise phases while trying to maximize the global efficiency of the propulsion system in all these flight phases.

1.3   Thesis Outline

This thesis has five chapters divided as follows:

• Chapter 1 introduces the topic of the disseration, the motivation and objectives.

• Chapter 2 provides a literature review with two sections. The first section is fundamentals that provides the theoretical fundations for the methodolghy. And the second section is the state of art which includes a brief history of the rotorcraft vehicles until the first VTOL achievement, a battery tecnology review, eVTOL UAM aplications and at last a performance comparison of the proposed design against the eVTOL UAV available in the market.

• Chapter 3 presents the methodology implemented to do the wing sizing, develop a preliminar variable pitch propeller, and prove the aircraft statical longitudinal stability of the aircraft.

• Chapter 4 discusses the results obtained from the adopted methodology. The limitations on wing sizing are analyzed, and verify the benefits of a variable pitch propeller. It is also present the aircraft performance and mission profile.

• Chapter 5 presents the conclusions overview and accomplishments. Future Work suggestions are also included.

Chapter 2

Literature Review

2.1 Fundamentals

2.1.1 Aerofoil

An aerofoil is defined as the cross-section of the wing. It influences the performance features such as take-off and landing, cruise speed, stall speed, stability, and others. Depending on design requirements and the role of the aircraft, the aerofoil may be adapted or newly designed for its specific application.

For the aerofoil to produce an aerodynamic force (lift) perpendicular to its direction of motion, a small resistance force (drag) is created (see figure 2.1). And the airflow over the upper surface increases its speed resulting in a pressure reduction. That generates a force (lift) perpendicular to the chord[4].

Equations (2.1) , (2.2), (2.3) represent the aerodynamic forces of the aerofoil. Where l is lift force per unit span, d is the drag force per unit span, $\bar{c}$ is the mean aerodynamic chord, ρ is the air density, V the airspeed, and C_l and C_d the lift and drag coefficients per unit span.

$$l = \frac{1}{2}\rho V^2 \bar{c} C_l \tag{2.1}$$

$$d = \frac{1}{2}\rho V^2 \bar{c} C_d \tag{2.2}$$

$$\frac{l}{d} = \frac{C_l}{C_d} \tag{2.3}$$
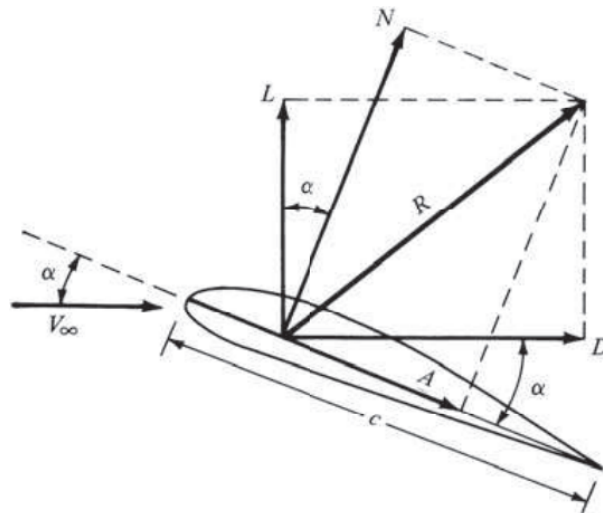
Figure 2.1: Aerofoil cross-section[5]

Lifting surfaces that use aerofoils include wings, tailplanes, fins, winglets, propeller blades and helicopter rotor blades. Control surfaces (e.g. ailerons, elevators and rudders) are shaped to contribute to the overall aerofoil section of the wing or tailplane[6]. The objective of aerofoil design is to achieve the best compromise between lift, drag, pitching moment and room to place the needed structure for the flight envelope that intends to operate.

An aerofoil has important geometrical parameters to understand and manage. They are[6]:

-**Chord** is the distance between the leading edge and trailing edge of the aerofoil.

-**Wing span** is the distance from one wing-tip to the opposite wing-tip.

-**Mean Camber Line** is the line of equal distance between the upper and lower surfaces of the aerofoil.

-**Leading Edge** is the foremost edge facing the oncoming air.

-**Trailing Edge** is the aftmost edge where the airflow leaves the aerofoil.

-**Thickness** is the maximum distance perpendicular to the chord between the upper surface and the lower surface of the aerofoil.
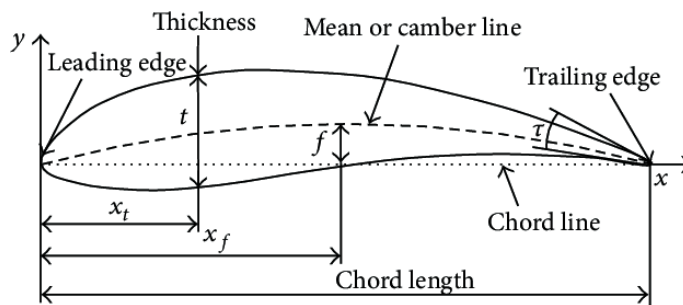
Figure 2.2: Aerofoil Geometry[7]

6

2.1.1.1 Thickness Ratio

The thickness ratio($\frac{t}{c}$) is an important parameter for aerofoils. It significantly affects, the weight and structure shape of the wing. According to Jenkinson, the thickness ratio will vary along the wingspan to adapt to the local flow and structural requirements. As e.g., the wing bending moment and shear force increase gradually from the tip to the root of the wing[8]. Hence, diminishing the thickness from root to tip is an advantage for less weight and profile drag.

Furthermore, the thickness ratio has relevant aerofoil aerodynamical effects. From Figure 2.3 is , one can conclude that the increase in thickness ratio enhances the aerodynamic coefficients of the aerofoil. However, the drag coefficient will also increase and, at some point will make it less efficient for the aerofoil.
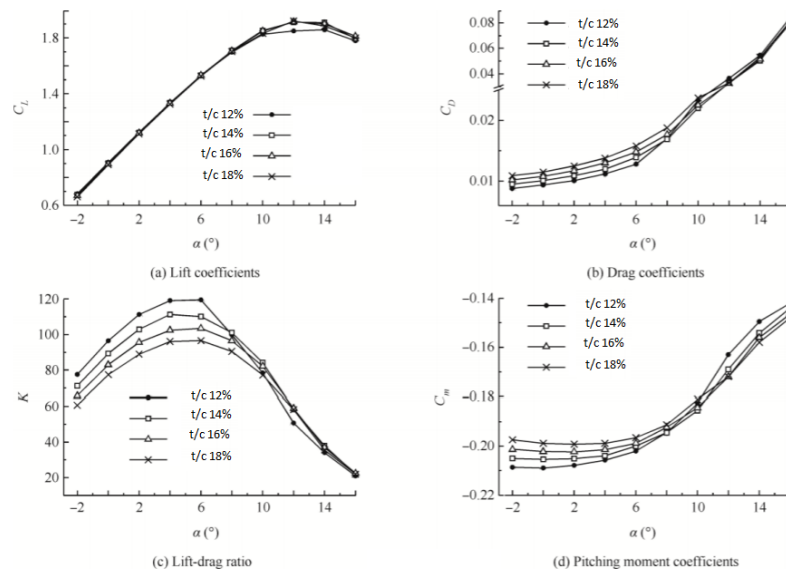
Figure 2.3: Thickness ratio influence on the aerofoil aerodynamic behaviour[9]

2.1.1.2 Reynolds Number

The Reynolds number points the characteristics and behaviour of a two-dimensional flow in interaction with an aerofoil. The flow around the aerofoil can be either laminar or turbulent depending on certain conditions. When is flow laminar it has an organized and linear behaviour interacting with aerofoil. When the flow is turbulent, has a non-linear behaviour, and has very chaotic and complex motion. The Reynolds number is a non-dimensional parameter that relates the ratio of the inertia forces to the viscous forces in a flow interacting with a body[10]. The Reynolds number for an aerofoil is defined by Equation (2.4), where μ is the dynamic viscosity, U_∞ is the free-stream velocity. It is noticeable that Reynolds has a higher magnitude when either free-stream speed increases, the chord increases or both. Generally, a flow maintains the laminar regime flow when interacting with a smooth wall (or aerofoil surface) and has no adverse pressure gradient until the Reynolds number reaches near 10^5[10]. To this point, the small disturbances

start amplifying and the flow transitions to the turbulent regime.

$$Re = \frac{\rho U_\infty c}{\mu} \qquad (2.4)$$

Figure 2.4 shows different flying creatures and aircraft's typical ranges speed and Re flying ranges. In the Re$>10^6$, it is where light aircraft and commercial airplanes operate (see Figure 2.4). In this regime, the boundary layer transition from laminar to turbulent does not cause flow separation from the aerofoil and subsequently reattachment. Thus, it increases aerodynamic performance for the wing and avoids a drag coefficient increase due to laminar separation bubbles[11]. In the case of low Reynolds mumber (Re$<5*10^5$) it operates model aircraft, homebuilt aircraft types with relatively small wing chords and low speeds of operation. When the aerofoil Reynolds number falls within 10^4 and 10^6, a laminar separation of the boundary layer exists before the trailing edge which is caused by the inability of laminar boundary layer to withstand intense adverse pressure gradients[12]. When the separation occurs at moderately Low Reynolds, the separated flow can become turbulent, recovering and reattaching [12] (see figure 2.5). This reattachment creates a laminar circulation bubble. That prevents the stall of the aerofoil to happen. Consequently, the bubbles produce higher aerofoil drag coefficients. Hence, Low Reynolds aerofoils have a smaller performance than High Reynolds aerofoils as a result of an increase in drag coefficient when the laminar separation bubbles exist [11].
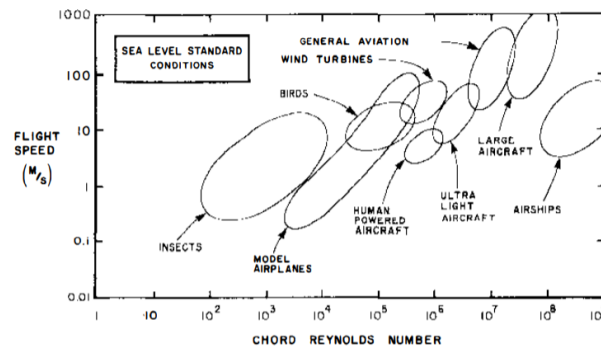
Figure 2.4: Reynolds Number Spectrum of Aircraft Operation[12]
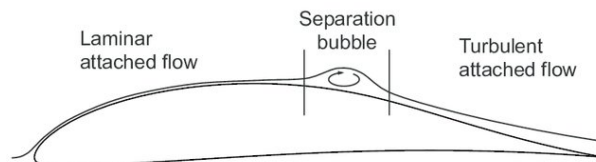
Figure 2.5: Laminar Separation Bubble[13]

2.1.1.3 Aerofoil Aerodynamic Coefficients

The aerodynamic coefficients define the aerodynamic behaviour for the profile aerofoil. They are the lift coefficient per wingspan (C_l), drag coefficient per wingspan (C_d), and

8

pitching moment coefficient (C_m). These parameters are a function of Reynolds number, angle of attack and Mach number (only in compressible flow, M>0.3). Since the span is a wing parameter, the aerodynamic forces are shown in Equations (2.5)(2.6)and(2.7) divided by the wingspan, becoming the profile forces(l,d,m). The dynamic pressure (q_∞) represents the dynamic pressure of the airflow.

$$C_l = \frac{L/b}{q_\infty c} \qquad (2.5)$$

$$C_d = \frac{D/b}{q_\infty c} \qquad (2.6)$$

$$C_m = \frac{M/b}{q_\infty c^2} \qquad (2.7)$$

2.1.2 Wing Geometry

The wing geometry mostly influences the aerofoil choice and the planform. The wing planform is defined by its mean aerodynamic chord, wingspan, aspect ratio, taper ratio, and sweep. Other parameters such as the incidence, twist, dihedral, and wing location, are parameters that affect the wing aerodynamic, weight, and stability. In Figure 2.6 the wing planform is represented with the main parameters, reference wing area (S), wingspan (b), the aspect ratio (A), the taper ratio (λ) these parameters are further discussed in this section.
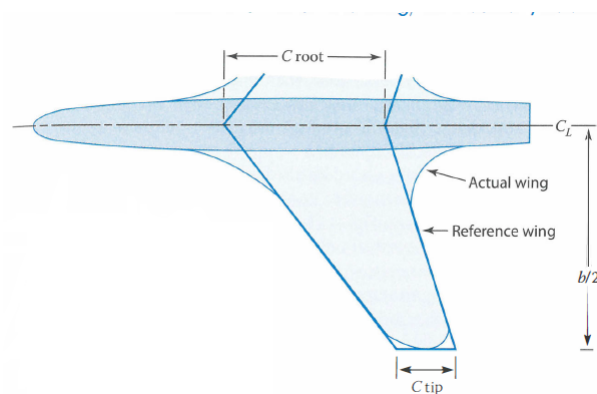
Figure 2.6: Wing Geometry Planform[14]

2.1.2.1 Aspect Ratio

The aspect ratio is the ratio between the square of wingspan and the wing area according to Equation (2.8). The aspect ratio affects the weight and aerodynamic features. Early wing designs were rectangular, so the aspect ratio is then the wingspan divided by wing chord[14].

$$AR = \frac{b^2}{S} \tag{2.8}$$

In the generation of lift in a real three-dimensional wing, the airflow from the lower surface and higher pressure moves to the upper surface towards the lower pressure. It occurs when air around the wing tip[14]. As shown in figure 2.7, this behaviour reduces the pressure difference between the lower and upper surface of the wing, thus diminishing the lift generation near the tip[14]. This effect is called wing-tip vortex and produces an induced drag (drag due to lift) affecting the wing performance.
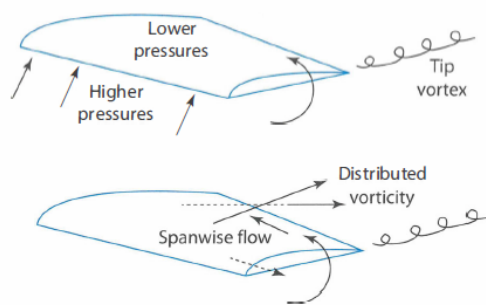
Figure 2.7: Wing tip vortices[14]

A high aspect ratio wing, the wing-tips are further away, causing the effect of the wing-tip vortex where a lift loss is inflicted and the induced drag is increase. For that reason, in many cases in commercial aviation, winglets are set to push the vortex further from the wing structure.

The induced drag depends on the wingspan when the wing area is the same, the span will be inversely proportional to the square root of the aspect ratio[14].

A high aspect ratio wing has a higher lift coefficient when compared with the counterpart. Though, a low aspect ratio wing results in a more manoeuvrable aircraft. Furthermore, a low aspect ratio wing has a stalling angle, a higher angle of attack when compared with a high aspect ratio.

The structure construction is more expensive, and heavy for a high aspect ratio wing when compared with a low aspect ratio. Consequently, the wing location may be compromise in case is designed a high aspect ratio wing due the mounting, torsion box arragement. Altogether, the choice between high or low aspect ratio relies on the design requirements and aircraft role.

2.1.2.2   Taper Ratio

The taper ratio (λ) is the ratio between the tip chord and the root chord of a wing as

shown in Equation (2.9). The taper ratio affects the lift distribution along the wingspan. Proven by Prandtl wing theory, the minimum induced drag for a wing with a given span occurs when the planform (i.e., wing loft load distribution) is elliptical [14]. The taper ratio varies between 0 to 1. A rectangular wing $\lambda = 1$ while a delta wing $\lambda = 0$ a trapezoidal wing has a typical value in the interval $0.4 < \lambda <= 0.6$[15].

$$\lambda = \frac{c_{tip}}{c_{root}} \tag{2.9}$$

An elliptical shape wing is more expensive and complex to construct[14]. The issue is overcome by replacing it with a tapered wing to diminish the effects of the wing-tip vortex, thus minimising the induced drag. Therefore, the lift distribution for a tapered wing is closer to an elliptical planform wing. Although a tapered wing results in a smaller induced drag wing with better lift distribution, it has shortcomings. It has higher costs and a more complex wing structure, as spars need to adapt to the wing's non-linear shape. Another problem is the tip stall, as a consequence of the small Reynolds number near the tip (due to small chord tip compared with the root chord), [16]. The c_l will reach near maximum value at the tip making stall possible; and when it happens the one wing-tip that stalls will cause a sudden roll of the aircraft from loss of lift[16]. These problems can be partially solved through the use of washout[16]. Unlike the tapered wing, a rectangular wing stall is first close to the wing root. A tapered wing design must compromise induced drag reduction, lift distribution and tip stall.

2.1.3 Airplane Stability and Control Surfaces

The Aircraft flight control are used to control the direction and attitude of the aircraft and performs any manoeuvring on an aircraft in flight. The flight control systems subdivides into what refers to as primary and secondary flight controls. Primary flight controls require safely control of an aircraft during flight and consist of ailerons, elevators (or, in some installations, stabilators) and a rudder. Secondary flight controls intend to improve the aircraft performance characteristics or to relieve excessive control loading. It consists of high lift devices such as slats and flaps as well as flight spoilers and trim systems[4].

The movement of any of the primary flight controls causes the aircraft to rotate around the axis of rotation associated with the control surface. The ailerons control motion around the longitudinal axis (roll), the elevator controls rotation around the lateral axis (pitch) and the rudder controls movement around the vertical axis (yaw)[6].
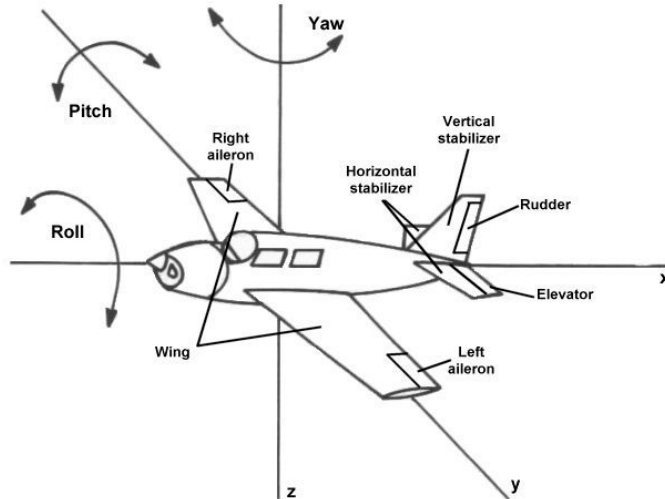
Figure 2.8: Airplane Control Surfaces and Axis[17]

The aircraft must be stable and controllable. Stability refers to the capability of a system to return to the equilibrium state after disturbance[18]. The stability concerns two parts that are static stability and dynamic stability. An airplane is statically stable when a force or moment created through disturbance is pushed to correction in the direction of the aircraft's original equilibrium state, and in equilibrium for which linear and angular acceleration is zero[14, 19]. Dynamic stability occurs when motions of the aircraft will return in time, it undergoes linear and angular accelerations to overcome the perturbations on the aircraft to the equilibrium state[14, 19].

The static stability does not imply that dynamic stability is achieved as well. If forces restoring the static original state are very high, an oscillation with great amplitude occurs as time passes. The aircraft though statically stable can diverge to a point of no return for its dynamic stability as represented in figure 2.9[14].
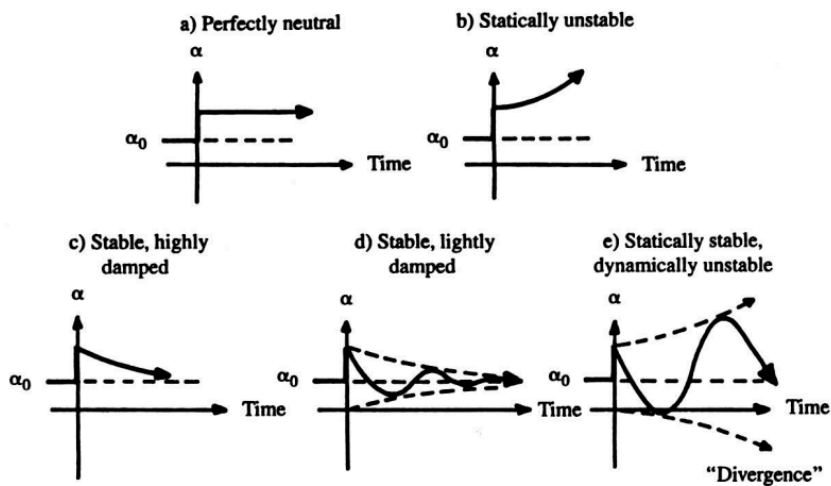
Figure 2.9: Static Stability and Dynamic Stability[14]

Furthermore, the static stability is divided into longitudinal, and latero-directional stability. Among the various contributors to the pitching moment about the centre of gravity

(CG) of the airplane is the lift through the wing aerodynamic centre, the wing pitching moment about the aerodynamic centre, the moment arm of the horizontal tail times its lift and the thrust line of the engine distance to the CG times the thrust. For an airplane to be statically stable in pitch, every time it experiences a change in the angle of attack, it must generate a pitching moment to oppose that change. The pitching moment (C_m) vs angle of attack or lift coefficient plot must have a negative slope and the point where the pitching moment is zero it is marked the neutral point. When the CG is shifted forward from neutral point, makes the airplane more statically stable. On the other way around, there is a rear CG location limit, where the slope becomes null, corresponding to the neutral point location.

The static margin is an important parameter for the longitudinal static stability of an airplane. This parameter represents the distance between the neutral point(x_{np}) and $x_{C.G}$ expressed as a percentage of the mean aerodynamic chord of the wing (see equation (2.10))[14]. When the static margin value is negative, the C.G is behind the neutral point, so the airplane is statically unstable. Generally, the static margin varies between 5 % and 15 % for commercial aircraft and can be higher for general aviation aircraft [14]. Figure 2.10 demonstrates the influence of the C.G position, relative to the neutral point, on the pitching moment as a function of lift coefficient. Correspondingly, the higher the of static margin, the more negative the slope of the pitching moment curve, thus, improving the longitudinal static stability.

$$SM = \overline{x_{np}} - \overline{x_{C.G}} \tag{2.10}$$
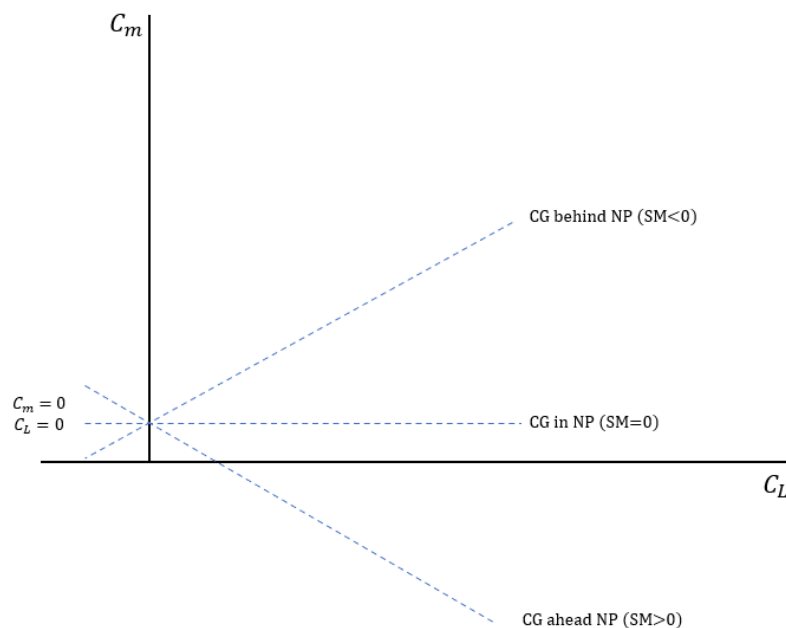
Figure 2.10: Static Margin

2.1.4 Actuator Disc Theory (Momentum Theory)

The actuator disc theory is a mathematical model for the lifting rotor in vertical flight. Therefore, it determines the influence of the actuator disc on the flow over a hovering or climbing situation, the induced velocity and the minimum power for a given thrust (P/T), according to the altitude air density and rotor disk diameter. However, there are losses of power not accounted for in this simple model. "Figure of Merit" is the parameter of efficiency that accounts for the minimum required power to hover in relation to the actual required power to hover[20, 21]. The following conditions are assumed for this theory[20] :

- Uniform inflow

- Non finiteness of no. of blades

- No Swirl in the wake

- No unsteady flow

- No tip losses due to vortices
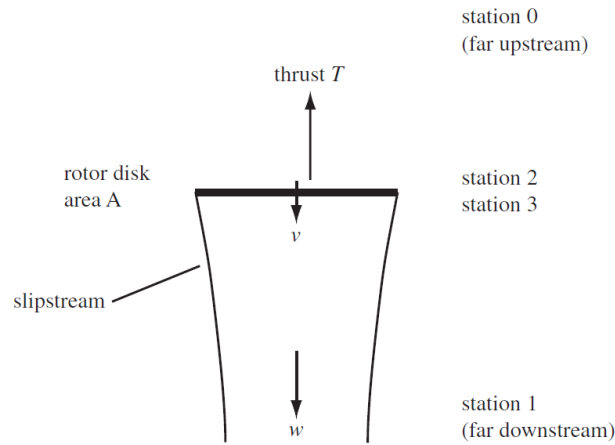
Figure 2.11: Actuator Disc Theory[22]

As a result of these assumptions, the actuator disc theory gives a first estimation of the wake-induced flow and thus the minimum ideal induced power (see Equation (2.11)) of the rotor[22].

The induced power (P_i), thrust (T), disk area (A) and induced velocity in hover (v_h) situation results in equations:

$$P_i = T\sqrt{\frac{T}{2\rho A}} \tag{2.11}$$

$$v_h = \sqrt{\frac{T}{2\rho A}} \tag{2.12}$$

In the momentum theory analysis in climb condition is represented in Figure 2.12. The velocity in the far wake is represented in Equation (2.15) and when climb rate is high the power approaches only the climb power TV[22].

$$v = -\frac{V}{2} + \sqrt{(\frac{V}{2})^2 + v_h^2}$$ (2.13)

(2.14)

$$V + \omega = V + 2v = \sqrt{V^2 + 4v_h^2}$$ (2.15)

The momentum theory model for vertical climb cannot be used in the descent condition, where V < 0 m/s (Figure 2.12). Since in descent the free stream velocity is directed upward, accordingly, the far downstream wake is above the rotor disc. In the momentum theory result for the induced velocity in descent[22], the net velocities at the disc and far downstream are computed in equations (2.16) to (2.18).

$$v = -\frac{V}{2} - \sqrt{(\frac{V}{2})^2 + v_h^2}$$ (2.16)

$$V + v = \frac{V}{2} - \sqrt{(\frac{V}{2})^2 + v_h^2}$$ (2.17)

$$V + \omega = V + 2v = -\sqrt{V^2 - 4v_h^2}$$ (2.18)
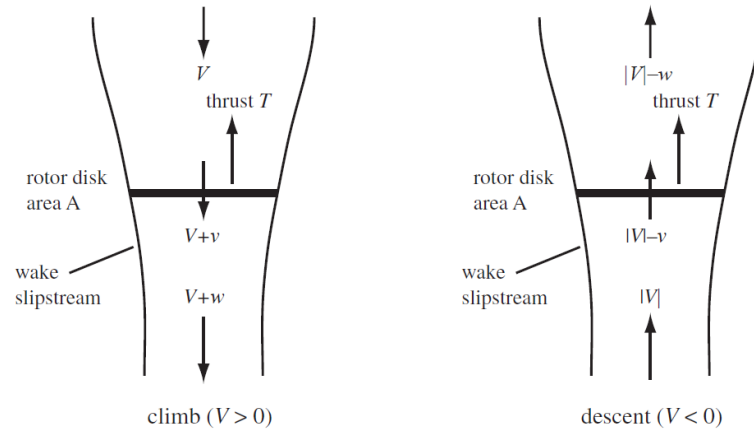
Figure 2.12: Momentum Theory in Climb (Left side) and Descent (Right Side)[22]

The induced power estimated in the momentum theory is about 65% below peak efficiency of the actual power thus acceptable for gross estimation of the power output (see Table 2.1)[22].

Table 2.1: Power losses [22]

Power component	[%]	Off Peak Efficiency[%]
Ideal Induced Power	74 to 78	65
Profile Power	10 to 19	25
Nonuniform Inflow	5 to 7	6
Swirl in the Wake	less than 1	less than 1
Tip Losses	2 to 4	3

2.1.4.1 Autorotation

The autorotation is used in emergency situations to land safely the rotorcraft rotorcraft in a power failure situation, to continue to produce thrust equal to the rotorcraft weight, thus having a safe descent for emergency landing [20]. The aircraft with low disc loading have higher hover efficiency making them more able to safely operate in vertical flight and use autorotation for an emergency landing. That is why helicopters are capable of autorotation due to bigger disc areas than other rotorcraft for example the Tilt-Rotors as V-22 Osprey cannot perform autorotation due to much higher disc loading. This issue affects the aircraft since the design consists in having a smaller disc area to achieve better cruise performance, weight reduction and other airplane manoeuvres. Though, it diminishes the vertical flight performance and its safe operation. Some aircraft designs use the redundancy of applying more motors in case of failure and some cases use Distributed Electric Propulsion (DEP), which means many small motor-propeller for safety in failure, or have STOL capabilities in case of an unsafe environment for VTOL.

2.1.5 Propeller Configuration

The role of a propeller is to transfer the mechanical rotational power generated at the motor shaft into forward thrust at a given airspeed through the acceleration of a mass of air flowing into the propeller disc on its lifting surfaces (blades)[23]. Three main variables influencing the propeller performance are diameter, the number of blades, and the blade pitch. A propeller operates not in isolation but must be designed to fit the aircraft motor requirements. A poorly chosen propeller-motor combination causes less performance, or may struggle to get airborne.
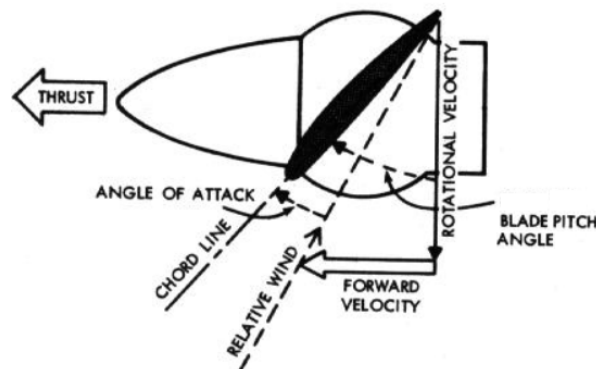
Figure 2.13: Propeller blade representation (adapted from [24])

The propeller diameter is often desired as high as the motor can support. High diameter helps for hover mode for better hover lift efficiency but airplane mode at high speeds can be very inefficient. The higher the diameter, the higher the inertia and the higher the tip speed[23]. When tip speed reaches near sonic levels, the potential to have a windmill effect occurs, to avoid that, the disc diameter must be study for limitations as airspeed increases through the blade.

The number of blades affects the thrust and efficiency. Hence, considering thrust per number of blades, generally the fewer blades design result in more efficient propeller disc [23]. Generally, small UAV applications using a two-blade configuration is a good compromise of thrust and efficiency. However, increasing the number of blades is the best solution to efficiently extract the desired thrust from a motor where a propeller with fewer blades cannot reach the required thrust for operation and in cases where vibration and noise are also an issue.

The propeller pitch refers to the distance that the propeller advances through the air during one revolution. A fine pitch means it will move forward through the air a short distance every revolution (low advance ratio) whereas a coarse pitch moves forward through the air a large distance every revolution (high advance ratio)[23]. Thus for hover mode, a fine pitch is recommended. But for airplane mode when in cruise operation due to high speeds a coarse pitch is the most efficient configuration. In climb operation a pitch higher than the fine pitch for take-off but less coarse pitch than the cruise is required.

2.1.6 Fixed Pitch Propeller

In Section 2.1.5 the pitch relevance to the design of the free propeller is described. The fine pitch and coarse pitch are interchangeable in a variable pitch propeller. However, in a fixed propeller , an ideal blade pitch is selected to operate through all flight states. It is designed based on the motor angular speed (ω_{motor})(RPM) and airspeed combination where the propeller is operating[23]. At different airspeeds and motor RPM regimes, there is less thrust available from the propeller.

As to compensate, manufacturers sometimes design a fine fixed pitch propeller for take-off and climb, and a coarse fixed pitch propeller for cruise available for the same airplane. Although simple to operate, however, a fixed pitch propeller must align several factors such as motor RPM, airspeed, relative airflow, blade pitch, diameter, number of blades, blade chord and length, and emitted sound levels. Therefore, the use of this propeller type for a configuration is inefficient due to the different modes of flight that the aircraft must operate in.

2.1.7 Variable Pitch Propeller or Collective Pitch

A variable-pitch propeller can gradually change the blade pitch during flight, from the pilot input or command (UAV)[23]. A blade adjusts to its optimum value for the phase of

flight, be it takeoff, climb or cruise. In some installations, it is possible to feather the propeller as well. Varying the blade pitch is effective since pitch changes to values resulting in better flight performance in horizontal and vertical flights.
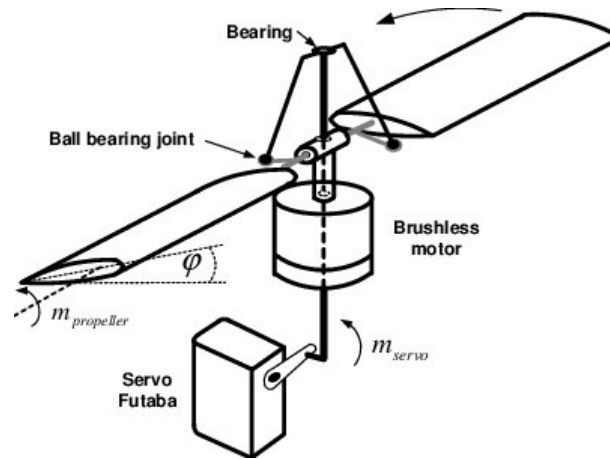
Figure 2.14: Variable Pitch of a Tail Sitter[25]

As shown in figure 2.14, small UAVs use servos and bearings to achieve a fine or coarse pitch state depending on the sensors input. For manned aircraft, it can be automatic, manual.

A variable-pitch propeller has usually a thinner and more flexible blade consequently, construction and design increase in complexity. It also adds more load to the motor. It has more parts integrating the whole system whilst adding more complexity, maintenance and cost when compared with the fixed-pitch propeller.

2.1.8 Performance

The performance of aircraft is the study of the capabilities, trade-offs and limitations of a design on its flight and mission. In this section, important parameters for better flight such as the Range, the flight speeds(v_s, v_c, v_{max}), Endurance, the rate of climb (ROC), angle of climb, figure of merit (FOM), hover lift efficiency are discussed.

2.1.8.1 Range

The range of an aircraft is defined as the distance the aircraft can fly from take-off to landing at the expense of the available energy consumption. For applications such as transport of passengers and cargo from short to long-range, this parameter is a crucial indicator of performance and in the case of the for operation as a UAM application.

The range for electric airplanes is different than for the typical fuel propeller-driven airplane. Therefore an evolution from the Bréguet Range Formula (Equation (2.19)) for fuel propeller-driven airplane to an electric propeller-driven supplied by a battery

was elaborated Equation (2.20) to adjust for the electric flight different conditions as follows[26, 27], where: C is the specific fuel consumption, W_0 is initial take-off weight, W_1 final weight. E_s is the battery specific energy, n_{global} is the mechanical and propulsive efficiency.

$$R = \frac{n_p}{C} ln \left(\frac{W_1}{W_0} \right) \frac{L}{D} \tag{2.19}$$

$$R = E_s n_{global} \frac{1}{g} \frac{m_{bat}}{m_{MTOW}} \frac{CL}{CD} \tag{2.20}$$

The range of a fully electric aircraft depends on the available energy. Nonetheless, the battery weight remains constant throughout the flight in opposition to fuel supplied in engines as shown in Equation (2.19) loses weight as the fuel depletes. Henceforth, relevant parameters to study are battery specific energy, total propulsive efficiency and aerodynamic efficiency. Therefore, the range for an electric aircraft increases all three parameters, particularly the E_s because the higher its value, the lower the battery weight for a given battery energy. For the same battery weight fraction it is possible to achieve a higher range.

In Figure 2.15 three different aerodynamic efficiencies $\frac{L}{D}$ and, $n_{global} = 0.75$, illustrate how increasing significantly the E_s results in much higher range for different battery mass ratios.
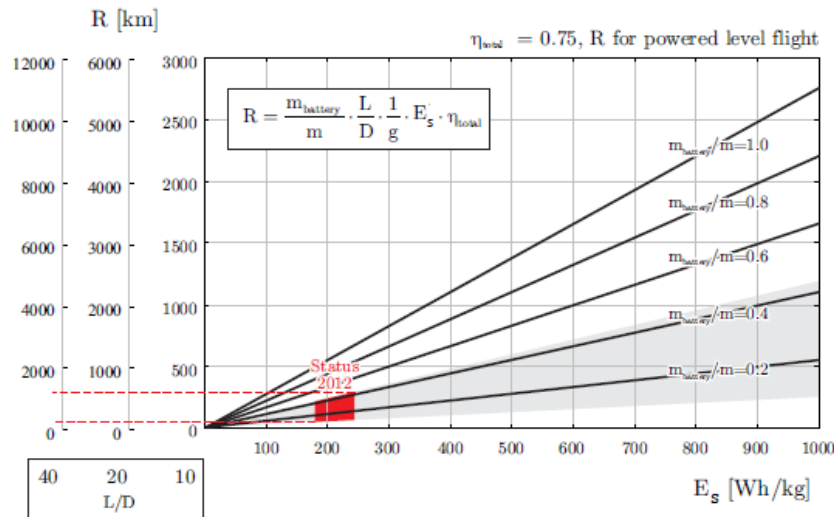
Figure 2.15: Range in function of Specific Energy Density [27]

2.1.8.2 Endurance

The endurance refers to the flight time that the aircraft remains airborne from the take-off to landing. It is crucial for airplane applications such as surveillance, and other designs that focus more on flight time. Within all conditions, the endurance is described

in the general Equation for range (2.20) by relating with the airspeed. For the same range, the endurance is inversely proportional to airspeed.

The $\frac{CL^{\frac{3}{2}}}{CD}$ is an efficiency parameter of endurance maximised to increase flight time. In high lift devices where the lift coefficient is higher while airspeed is diminished (see Equation (2.23)) it is utilized this parameter. For the Equation (2.22) computed when joining Equation (2.20) and (2.6) to find the endurance of an electric aircraft for a given battery.

$$R = v_\infty E \tag{2.21}$$

$$E = \frac{1}{\sqrt{\frac{2MTOW}{\rho_\infty S}}} E_s n_{global} \frac{1}{g} \frac{m_{bat}}{m_{MTOW}} \frac{CL^{\frac{3}{2}}}{CD} \tag{2.22}$$

2.1.8.3 Flight Speeds

Regarding this section is discussed the most significant flight speeds in straight-level flight. The stall speed(v_s), cruise speed,(v_c), and maximum speed(v_{max}). Figure 2.16 shows that it is critical to improve the aerodynamics and propulsion to achieve a better flight envelope. The required power (P_r) relates to the drag force times the airspeed , and the available power (P_a) is the thrust times the airspeed. As the available power increases and required power decreases we can fly from a range of multiple cruise speeds to selected, ones that are efficient for the airplane.
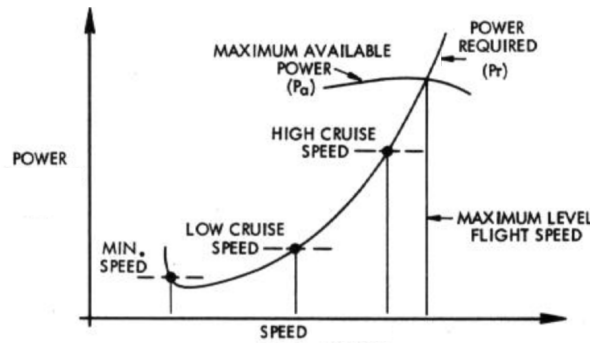
Figure 2.16: Power vs Flight Speeds (adapted from [28])

The stall speed is the minimum speed to operate the aircraft in cruise flight before stalling the aircraft. Since the speed is inversely proportional to the square root of lift coefficient, the lower its value, the higher the maximum lift coefficient of the aircraft. Equation (2.23) is an airspeed Equation with relation to the lift coefficient. Nonetheless, for the stall speed is not a problem because it operates in hover mode, near zero airspeed velocity.

$$v_s = \sqrt{\frac{2W}{\rho S C_{Lmax}}} \tag{2.23}$$

The cruise speed occurs when near or at the best $\frac{L}{D}$ ratio. Depending on how high it can become at the maximum speed, its value is much higher performing at the speed with the smallest drag coefficient in a cruise condition.

The maximum speed is defined at the power available limitation, thus, $P_A = P_R$, or when flight speed is so high that vibration can cause damage to the aircraft due to structural limitations(flutter). Usually, high flight speeds occur when the lift coefficient is at the lowest or near the lowest point for the aircraft operation.

2.1.8.4 Climb

The rate of climb (ROC) describes the instantaneous vertical velocity that depends on the altitude, the weight of the aircraft and the difference of power available and power required. For airliners, ROC must be sufficiently high to achieve cruising altitude within a reasonable time whereas for military applications, fighters must have a very high ROC for intercepting a foe as quickly as possible. Manoeuvring is very beneficial to a high climb rate[29] to reach a given altitude in the shortest possible time.
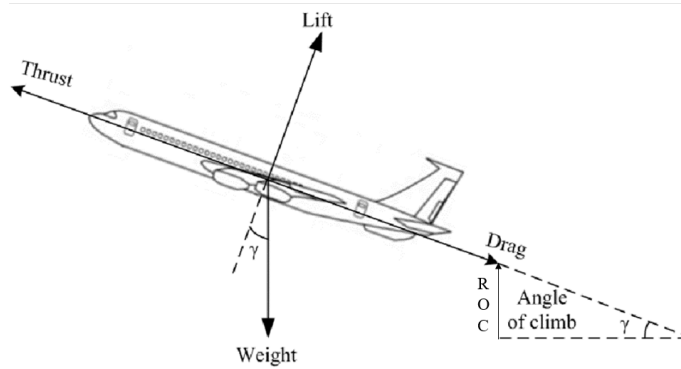
Figure 2.17: Airplane Climb[30]

The influence of the $\frac{P_A}{W}$ and wing loading($\frac{W}{S}$), demonstrates how much the weight of the airplane influences this parameter[29]. Since required power is a parameter that depends on the aircraft aerodynamics, from Equation (2.24) when breaking down the required power, it results in Equation (2.25), which gives a better view of the weight effect on the rate of climb. Thus, the lower the MTOW of the aircraft, the better ROC, and lower wing loading also increases the ROC. Or as, an alternative, increasing the power available when the MTOM or wing loading are restricted.

$$ROC = \frac{P_A - P_R}{W} \tag{2.24}$$

$$ROC = \frac{P_A}{W} - \left(\frac{C_D}{C_L^{\frac{3}{2}}} \right) \sqrt{\frac{2W}{\rho S}} \tag{2.25}$$

Another parameter related to the ROC is the angle of climb. Geometrically it represents the difference between the pitch angle and the angle of attack for the aircraft. Since the ROC is a vertical speed, applying the Pitagoras Theorem, ROC is the opposite side of the angle of climb (γ_c) (see figure2.17). Then the direction of relative wind and sine of the climb angle equals the ROC (see Equation (2.26)).

$$V \sin \gamma_c = ROC \tag{2.26}$$

2.1.8.5 Hover Performance

The figure of merit (FOM) is the ratio of the ideal induced power (P_i) to the actual power needed to hover the rotorcraft (P) (Equation(2.27)). These parameters and the disc loading are compared to give us a first impression of the rotorcraft's broader characteristics.

$$FOM = \frac{P_i}{P} \tag{2.27}$$

Since the FOM, is from a hovering rotor, it is appropriate to define Equation (2.28) where the useful power (C_P) is that required to produce a static thrust (C_T) [22]. The FOM can also represent the contributions of the induced power and profile power to the rotor power, written as Equation(2.29).

$$FOM = \frac{C_T^{\frac{3}{2}}}{C_P} \tag{2.28}$$

$$FOM = \frac{C_{Pi}}{(C_{Pi} + C_{P0})} \tag{2.29}$$

Usually, the profile power C_{P0} contributes at least 10% to 20% of the total power, and the induced power C_{Pi} around 10% to 15% higher than the ideal power[22]. The highest value for the figure of merit is close to 0.75[22].

The other two performance parameters are the disc loading and Hover Lift Efficiency($\frac{T}{P}$). Disc Loading($\frac{W}{A}$) measures how much lift is produced by the unit area of the disc, therefore, the higher values are those of aircraft like F-35 or Harrier. The lower the disc loading, the closer to the helicopter is the design. Figure 2.18 shows that the hover lift efficiency increases as the disc loading decreases.
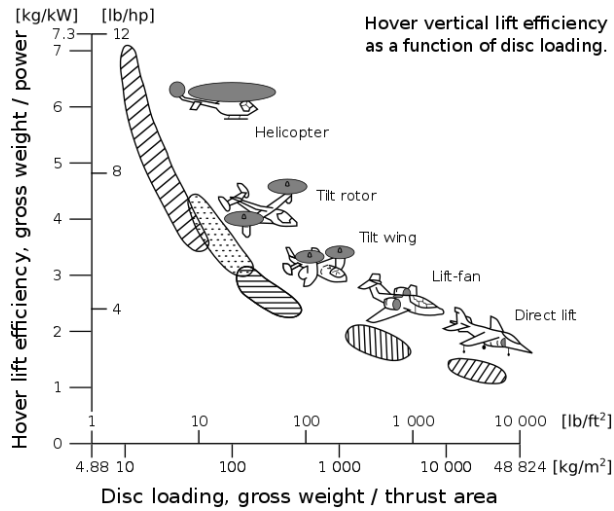
Figure 2.18: Disc Loading vs Hover Lift Efficiency [31]

2.2 State of the art

2.2.1 Brief history

The introduction of rotorcraft vehicles and then the application of the helicopters represent the first step for the conception of the aircraft. In the development of rotorcraft in the XX century, the engineer Juan de La Cierva came up with the creation of the "flapping hinge". That invention served as the foundation of the development of autogiro (see Figure 2.19) and helicopters. After the "autogiro" Juan de la Cierva further developed the rotor hub system for the autogiro which he called the "autodynamic rotor".

Figure 2.19: Autogiro C.30 G-ACFI[32]

This system replaced the airplane control surfaces[20], providing various functionalities employing torque, inertial, and aerodynamic forces acting on tailored rotor blades rotating about the inclined flap, drag, and feather hinges. Additional functionality was provided by mechanical means within the hub actuated by those same forces or via a cockpit control. The autodynamic rotor achieved much of its functionality by coupling blade motion about two or more of the feather (x), drag (y), and flap (z) axes. The value of the coupling could be positive or negative relative to the respective axis [32].

23
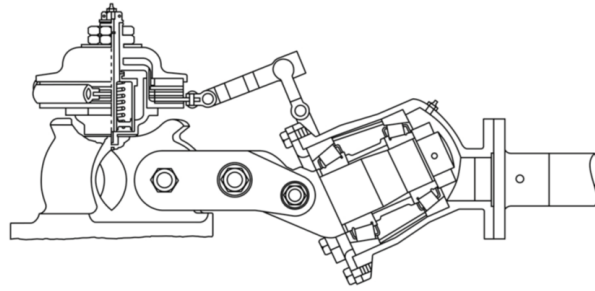
Figure 2.20: Autodynamic rotor tested on the C.30 G-ACFI[32]

Following World War II, significant progress was made again in research of helicopter dynamics and stability. It led directly to machines that were less stressful to fly and correspondingly safer. The Bell 47 based on the research of Arthur Young was the first helicopter certified in 1946. The Sycamore of 1952 (Figure 2.21) was designed by Hafner, it is the first certified British helicopter. It was remarkable for its performance in flight and also its light control forces that did not require power assistance[33].

Figure 2.21: Sycamore[33]

During the 1950s and 1960s, after the development of the early helicopter designs, great research effort was made for the conception of an aircraft able to fly in the cruise like an airplane and able to take-off and land vertically like a helicopter. This coined the term VTOL aircraft[34]. The XV-3 was a remarkable attempt to create this type of aircraft. Unfortunately, the instability caused by adverse environmental effects or failure, as well as high vibration was unable to be solved with the traditional analyses and experimentation of the time, the project needed further testing. Beyond the achievement of the XV-3 project was the prospect of performing an in flight conversion of a helicopter for take-off and landing to an airplane in a safer controllable setting[31].

Figure 2.22: XV-3[31]

During the 1970s, the XV-15 tilt rotor research started. This project overcame many of the issues unsolved with the XV-3 and contributed to the future development of tilt rotors as JVX/V22 Osprey in the 1990s[31].

Augusta Westland 609 Leonardo (known as BB609) is a tilt-rotor VTOL being developed from 1996 with the concepts and features inherited from the XV-15 research project[31]. Unfortunately, a tragic accident happened in 2015, prior to the aircraft certification, during a high speed dive test, two pilots died resulting in an investigation of the crash. The accident report concludes that oscillation on the yaw control evolves to an excessive yaw angle. That forced its prop-rotors to hit its wings multiple times and damaged the hydraulic and fuel line, following an in-flight breakup and fire[35]. Subsequently, a redesign was demanded and consequently halted the certification from FAA. It is expected to be certified this year (2022) by FAA as probably the first civil tilt-rotor aircraft in the market.

Figure 2.23: August Westland AW609[36]

In the last decade the tilt-rotor concept and the application of tilt-rotor in the military branch was first achieved with Bell V2 Osprey, and soon will come the Bell V280. In Section 2.2.4 recent examples of concepts for electric VTOL already developed are given,

though, almost all do not have flight certifications for civil operations.

2.2.2   Electric Flight

The recent demands for electrification in general aviation, meaning the use of cleaner energy sources versus fossil fuel mandate improvements in its capability and reliability for that to come to fruition. In recent years more investment in battery technology is being made. Many projections indicate that batteries are one of the most reliable sources of clean energy for electric vehicles and other industrial machines. However, significant technical limitations are not yet overcome to make batteries the main source of energy for the future, in this case, the unique and reliable energy storage to power a big electric aircraft as the eVTOL.

The battery is a device used to convert the energy stored within molecules to useful energy by an electrochemical process. It is assembled from one or more electrochemical cells, arranged in a specific configuration depending on the electrical output requirements. Energy is released from internal chemical reactions through an electrolyte between two electrodes, an anode and a cathode. The cathode is the external positive terminal(+), while the anode is the external negative terminal(-)[37].

As noted, batteries could be classified as primary, which are those that cannot be recharged and reused, and secondary batteries, those that can be recharged and reused. Batteries belonging to the first category are zinc-carbon cells, heavy duty zinc-chloride cells, alkaline cells, lithium and silver batteries, mercuric oxide cells and zinc-air cells. Batteries belonging to the second category are, e.g. lead-acid batteries, nickel-cadmium batteries, nickel-metal-hydride batteries, rechargeable alkaline cells, lithium-ion batteries, lithium-ion polymer batteries, lithium-air batteries and lithium-sulphur batteries[37].

Many concepts exist for electric propulsion systems which they differ in energy storage and conversion. The main focus is on battery based systems and fuel cell based systems. Both systems are under constant development, driven by mobile applications like automobiles, and aerospace. Most of these developments are currently aiming at further increase the energy density capabilities above Li-ion cells ($120 - 220\frac{Wh}{kg}$ for some combinations)[38, 39].

In aerospace applications, the use of lithium-ion battery types is much more common. The lithium-ion battery has attracted the most attention due to its superior performance. However, it is harder to combine all the desired properties such as high energy content, power capabilities and long cycle life into a single technology and the existing lithium-ion battery has reached its limit of advancement.
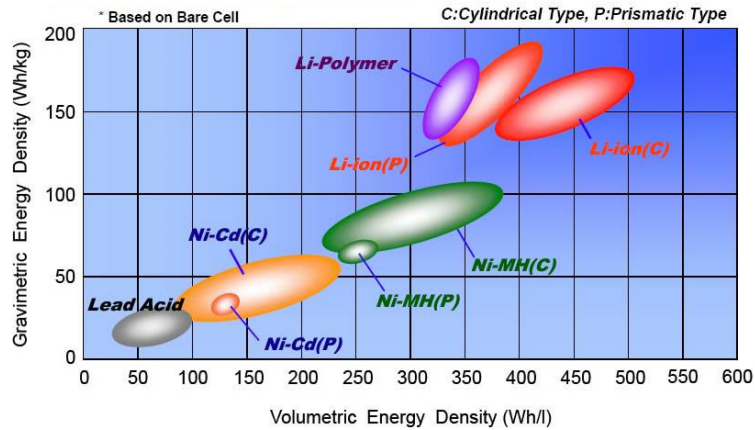
Figure 2.24: Gravimetric and volumetric cells comparison[40]

Figure 2.24 reveals reasons for the lithium combination becoming used extensively in the field. Not only it is much lighter for the same energy amount but also more compact, thus requiring less volume for application than its counterparts. Weight and volume are crucial for transport aviation since the aircraft is optimized to carry as much payload as possible. Henceforth, lithium batteries will stay fulfilling the energy demand for many devices until safer, durable and especially higher "specific energy density" energy alternatives are developed and tested as a reliable replacement. Moreover, a significant effort is made to enhance the energy density of this battery as much as possible, however, the theoretical limit is soon to be achieved (around $\approx 250 \frac{Wh}{kg}$).

Unfortunately, the application of electric propulsion in aeronautics has yet severe issues dealing with the mass specific energy density and volumetric specific energy. Compared with fuel or Kerosene, currently the most advanced battery system presents 60 times less mass specific energy, and 18 times less volumetric specific energy [27].

Meanwhile, other newer combinations such as lithium-air, zinc-air, lithium sulphur, magnesium, and tin-based technologies, with their specific properties, seem to offer promising solutions, though their durability and lifetime are still under the lithium-ion batteries, therefore, not yet useful for aircraft applications. Furthermore, the commercial exploitation of these batteries has been hampered by a series of difficulties such as self-discharge and low life cycle.[41]. Table 2.2 some of the rechargeable batteries types are presented along their respective characteristics.

Table 2.2: Battery types comparison

Type Battery	Cells Volt	Specific Energy [Wh/kg]	Energy Density [kWh/m^3]	Specific Power [W/kg]	Cycle Life	Self Discharge Rate(Month)	Efficiency [%]
Lead-acid[37]	2	1-60	30-60	300	250-1000	17%	80-90
Ni-Cad[37]	1.2	20-0	25	150-300	600-1200	10-20%	85
Ni-MH[37]	1.2	1-100	80-100	220	600-1200	2.9%	88
Li-ion[39] LFP	3.2	120	-	-	1000-2000	1%	98-99
Li-ion[39] NMC	3.7	220	-	-	1000-2000	1%	-
Li-Sulphur[39]	2.15	200-550	-	-	≈ 50	8-15%	-
Li-Metal[38] (Li-MnO2)	3	230-270	520-535	-	-	-	-
Li-Air[42]	3.3	150-6000	30-1000	-	-	-	-

Furthermore, the development of solid state batteries is showing great potential as an alternative for use and replacement in many fields where lithium battery is commonly used. That is positive since the increase in demand, especially for the automobiles, and policies in action over developed world for decarbonization in the next decade is projected to cause shortages of lithium metal and driving the need to create new sites for the exploration of the resource.

2.2.3   Challenges for Helicopters and eVTOL

The eVTOL aircraft has expectations to replace in some decades the helicopter for some applications in short-range transportation of passengers and cargo in Urban areas when crucial limitations on battery source such as mass specific energy, are overcome (see Section 2.2.2). Due to the prospect of the eVTOL having advantages over the helicopter such as a cost-effective vehicle in terms of energy or power demand, achieving greater speed than helicopter, lower cost production and maintenance and operator cost. Yet, helicopters are technologically mature, reliable and well accepted by the public.

Helicopters are having a steady decline in demand (see Figure 2.25), even before the pandemic, due to demand from the customers and users for the transition to more lightweight aircraft, and better operational efficiency. Furthermore, the budget reduction from developed countries to helicopter production and design is discouraging the growth of this aircraft market. That is pressing manufacturers and developers to innovate for lighter helicopters with the least power consumption, or in cases such as Bell, to invest in eVTOL projects for possible replacement of the helicopter in similar operations[43, 1].

OEM DELIVERIES 2010 - 2018
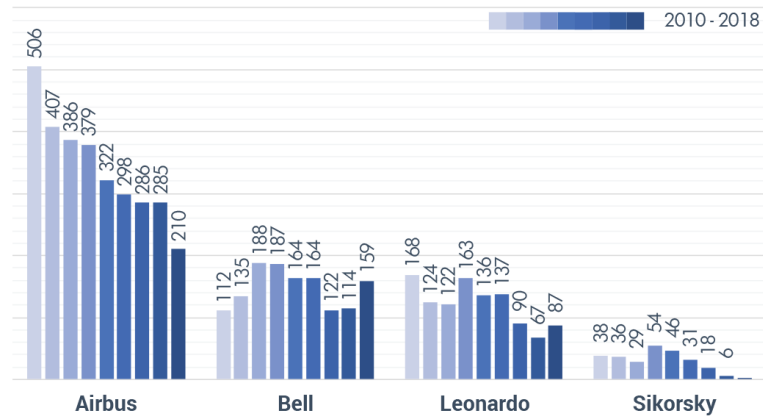
Figure 2.25: Helicopter Demand Decline[44]

The required technology developments are demonstrated by introducing battery-powered electric propulsion systems to small and medium-sized aircraft, since currently battery capacity to sustain electric powered airplanes are limited to small vehicles with up to two passengers due to low endurance and yet limited for short-range. To power larger aircraft much further improvement in battery technology is needed. Compared with today's technology, specific energy and the specific energy density have to be increased at least by a factor of 10 to become suitable for the industry to invest and pressure the legal entities to certify this aircraft type for application in larger (regional) aircraft market[27].

Although the UAM market has the potential to grow as a market study in 2020 made by Research Dive (see Figure 2.26) shows good prospects for the next decade. Applications are air taxis, personal air vehicles, cargo air vehicles, and air ambulances, among others. This is expected to offer opportunities to players in the helicopter market, who have the design and manufacturing capabilities to produce this aircraft and to increase their market share. Companies such as Uber have collaborated with various OEMs, like Bell, Karem Aircraft, and Boeing, to commercialize the urban air mobility concept by 2023. When commercialized, this concept is expected to enable passengers to share air services between cities and suburbs, and eventually within cities[3].
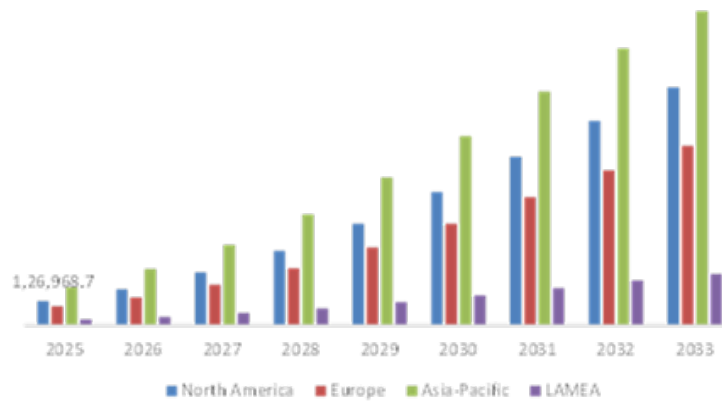
Figure 2.26: Global growth in demand for [45]

2.2.4 eVTOL UAM Applications

As discussed in Section 2.2.1, Tilt rotors are the predecessors for the eVTOL and some of its configurations. The main difference lies in not being "electric" and just VTOL fully reliable on fuel. These have engines on the tip of the wings, making them less stable and complex to operate. These also have an average higher P/W ratio, justifying their reliability on fuel propulsion systems for decent mid-range cruise flight. However, the cons are the high consumption and maintenance a consequence of design features, lower hover performance compared to the helicopter, lower forward flight performance against the propeller airplane, and airworthiness issues. Those reasons undermine the progression of the tilt-rotor as a commonly utilized aircraft configuration with more applications especially in civil aviation [46].

In recent years, many eVTOL concepts have been surging and developing. Yet, due to the limitations described in Section 2.2.2 , there is still more progress for this aircraft to achieve introduction in civil applications as a common reality. The definition of an eVTOL has been broadly used and depending upon the aviation industry background, some eVTOL configurations are considered or not as such. Some are hybrid VTOL concepts or the wingless multi-rotors alike. Nevertheless, the most acceptable definition for is an aircraft with the following main features:

- Must use an electric propulsion system to power the aircraft;
- Must perform take-off and landing vertically but cruising and most manoeuvrers in an airplane configuration.

Many companies and startups have started developing and testing different electric VTOLs. The website Electric VTOL News, published by the Vertical Flight Society, classifies eVTOLs in the following categories:
- Vectored Thrust;
- Lift + Cruise;

- Wingless;
- Hoverbikes;
- eHelos (conventional electric helicopters).

Even though the common definition of includes wingless aircraft, in practice, that is far from the truth. Those requirements are fundamental for an airplane with rotor mode configuration. Therefore the two main categories for eVTOL regarding the propulsion system configuration are:

-Vectored Thrust;

-Lift + Cruise.

The vectored thrust has a fixed-wing for an efficient cruise and propulsion system integrated to sustain both VTOL and cruise flight. The lift + cruise eVTOLs have a fixed-wing for an efficient cruise and separate propulsion systems for both VTOL and cruise flight[34]. In Figure 2.27, a compilation made by Vertical Society that shows a wheel of fortune summarizing the many concepts in the market and the developers of some of those eVTOL aircraft for UAM applications.

Figure 2.27: Wheel of concepts. Right side outside the red line are fixed-wing configuration [47]

Mentioning some VTOL fixed-wing configurations, recent examples are Opener Black-Fly V3, Kitty Hawk Heaviside and Lilium Jet. Those three are remarkably distinct in the propulsion system, number of PAX(passengers), speed and range.

The Blackfly is an eVTOL made by Opener, it is a one-seat short-range tail sitter, vectored-thrust propeller aircraft with 64km range. Already flown over 2,300 times, advantages of being ultralight, simple, and disassembled and reassembled with ease. It

makes it promising for recreation or single passenger short distance transportation[48], and it is already certified as PART 103. The Kitty Hawk Heaviside is a vectored thrust propeller aircraft developed by Kitty Hawk. It is a single-seat with eight tilt propellers. It is 100 times quieter than a helicopter, nevertheless faster and lighter. It has a range of 160 km and a 354 km/h cruise speed. It uses distributed electric propulsion (DEP) to provide safety redundancy. Hence, if some propellers fail, others can sustain flight for a safe emergency landing. Another reliable feature is that it can land as an airplane [49].

The Lilium Jet 5 seater is an ambitious configuration that uses a vectored thrust configuration integrating ducted fan jet electric motors, supplied by fuel cells and battery. That is an unique configuration where Lilium Jet is its pioneer. This configuration has a top speed of 300 km/h and a range of 300 km. Compared with multicopter aircraft, that consumes much of their energy sustaining the cruising flight operation, Lilium Jet can rely on the lift generated by the fixed-wing and requires less than 10 % of its maximum 2,000 hp when in cruise flight. Lilium jet also reduces complexity, and structure weight by adopting a canard configuration [50, 51]. Lilium Jet is in the prototype phase working on getting the EASA and FAA certifications.

Figure 2.28: Opener Blackfly V3[48]

Figure 2.29: Kitty Hawk Heaviside[49]

Figure 2.30: Lilium Jet 5 seater[51]

Table 2.3 presents some performance and wing parameters of some UAM eVTOL designs. The three examples above were representations from a variety of configurations designed by numerous companies. From jet and electric propulsion to DEP, the list of concepts and models developed is extensive, to define the best configuration for the role of UAM.

Table 2.3: eVTOL Models Comparinson

UAM	MTOM/Payload [kg]	Wingspan [m]	Range [km]	$v_c r$ [knots]	Pax
XTI Trifan600[52]	2404/816	11.5	1240	300	6
S4[53, 54]	1815/-	10.7	241.4	173.9	5
Kitty-Hawk-Cora[55]	-/181	11	100	95.59	2
Opener Blackfly V3[48]	255.4/113.4	4.1	64.37	69.52	1
Lilium Jet[50]	-/-	-	300	161.63	5
Kitty-Hawk Heavyside[49]	-/-	6	160.93	191.2	1
Bell Nexus 4EX[56, 57]	3175/-	12.2	97	130.35	5
Archer Maker[58]	1497/-	12.2	96	130.35	2
ALIA-250c[59, 60]	2721.5/-	15.24	463	145.8	5

Table 2.4: VTOL's Aircraft Specifications

Model	Energy Source	MTOM [kg]	Span [m]	Range [km]	Endurance [min]	v_{cr} [$\frac{m}{s}$]	MTOM/ b [$\frac{kg}{m}$]
Kuzgun[61]	Battery	4.7	2	26.60	25	20	2.35
FW-VTOLUAV[62]	Battery	3.688	1.7	56	30	30	2.17
KapetAir[63]	Battery	6.5	3.3	120	120	16.67	1.97
ALTI Ascend[64]	Hybrid	10	2	450	360	20	5.00
Quantum Systems TRINITY[65]	Hybrid	5	2.394	100	98	17	2.09
Heliplane[66]	Battery	8.5	2.7	72	60	20	3.15
Vector[67]	Battery	7.4	2.8	108	120	15	2.64
CW 15[68]	-	16.5	3.54	108	90	20	4.66
Sentaero BVLOS[69]	Battery	8.165	2.299	88.51	72	20.11	3.55
CT-05[70]	Battery	6	1.8	109.2	91	20	3.33
SLA-2[71]	-	6.8	2.4	99	75	22	2.83
Standard EOS C VTOL[72]	Battery	14,2	5	120	120	18	2.84
TiltRotor[73]	-	15,351	2.268	100	55	30	6.77
Swift[74]	-	9	2.6	97	90	18	3.46
PLASMAFALCON 1.11 / VTOL[75]	Battery	6.6	1.11	100	57	50	5.95
5487FB8/10-146[76]	-	30	4.21	360	240	25	7.13
5487FB8/10-107[77]	-	15	3	160	105	26	5
CW-20[78]	-	25	3.2	300	180	27,78	7.81
DZ-20[79]	Fuel	24	3.2	540	360	25	7.5
Quantum Systems Tron F90+[80]	Battery	14	3.5	160	120	22	4
Penguin B VTOL[81]	Fuel	30	3.9	720	480	25	7.69
SkyEye Sierra[82]	Battery	12.5	3.1	195	180	18	4.03
WingtraOne GEN[83]	Battery	4.5	0.125	56	59	16	36
Great Shark[84]	Battery	20.3	3.2	270	180	25	7.19
AeroeVTOL UAV	Battery	10	2.14	148	87	29	**4.67**
AeroeVTOL UAV (Future)	**Battery**	**10**	**2.14**	**387**	**220**	**29**	**4.67**

2.2.5   eVTOL UAV

Although the previous section discusses UAM applications and eVTOL concepts, this section includes models developed for the UAV market. Since the present work is focused in the design of an eVTOLUAV.

Table 2.4 lists some eVTOL and VTOL UAVs in the market for this dissertation. The models presented have a MTOM<50 kg, which ranks small UAVs. Most of the models are rolled for surveillance applications and few are experimental designs.

The aircraft specified on the list have a MTOM range between 4-30 kg. The proposed eVTOL developed in this work has a MTOM near 10 kg, moreover a Li-ion battery with a common $E_s = 120\,Wh/kg$ it is implemented. Is also study to the case of implementing a Li-ion battery with future capacity $E_s = 250\,Wh/kg$ [27]. The design is named "AeroeVTOL UAV", and among other aircraft shown in the table 2.4 was plotted for comparison and to visualize the trend line for some performance parameters.

Figure 2.31 shows a trend for the aircraft with smaller wingspan also to have smaller MTOM. The wingspan for the "AeroeVTOL UAV" is smaller than the trend for the same MTOM resulting in, higher cruise speed, maximum speed, and better aerodynamic efficiency at higher airspeeds. The stall speed increases, though for this configuration type it is not detrimental. The other aircraft have worse cruise speed due to lower wing loading than "AeroeVTOL UAV" (Figure 2.32). Since they are optimized for endurance, sacrificing speed for flight time, that explains most having a bigger wingspan.
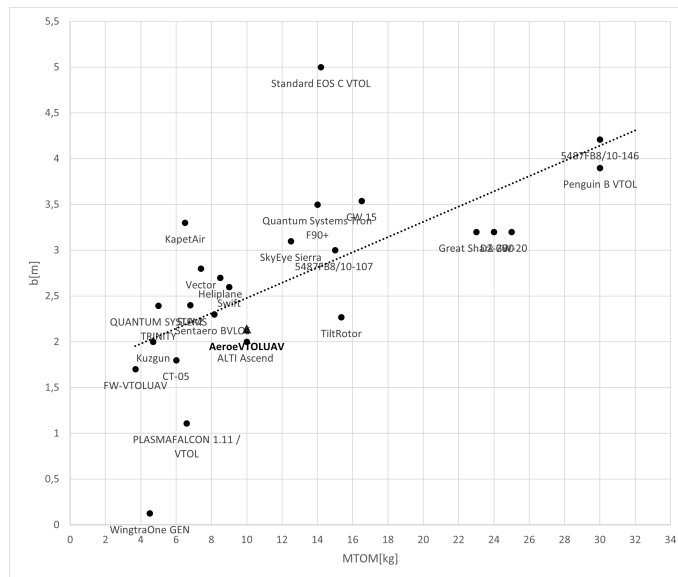
Figure 2.31: Scatter plot of Wingspan vs MTOM of the VTOLs presented in table 2.4
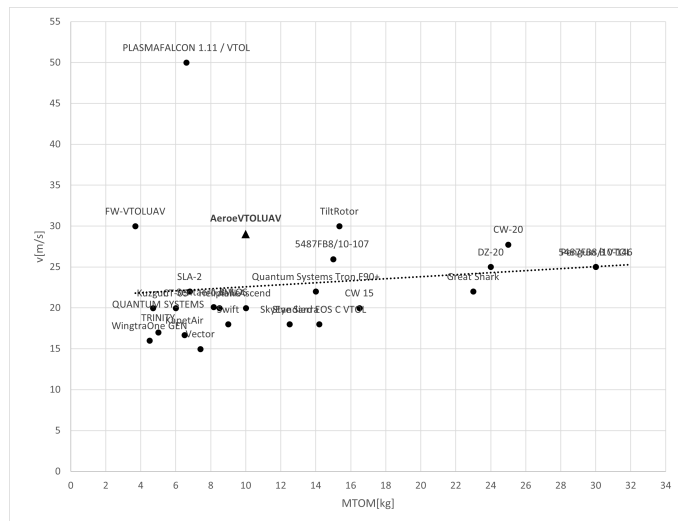
Figure 2.32: Scatter plot of Cruise Speed vs MTOM of the VTOLs presented in table 2.4

The endurance graph(see Figure 2.33) is relevant because most aircraft are for surveillance purposes. The high wing loading of the "AeroeVTOL UAV" with E_s = 120 Wh/kg results in higher speed and power consumption. Furthermore, it shows lower endurance than the trend, but compensates it with better high speed than the trend. In the case of fuel powered VTOL, since they have higher supply of energy for having higher power density

than the counterparts. That results in significant increase in range and endurance.
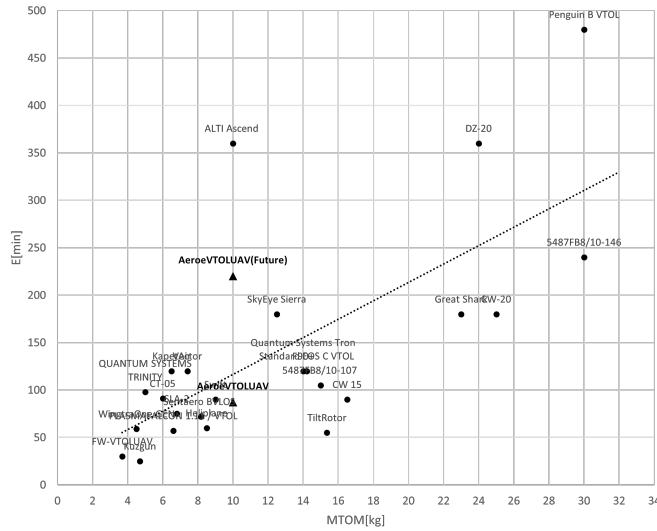
Figure 2.33: Scatter plot of Endurance vs MTOM of the VTOLs presented in table 2.4

The range performance of Figure 2.34 also shows promising results. This aircraft design has a higher range than the trend for its MTOM and using a common Li-ion battery of E_s = 120 Wh/kg. It is though surpassed by fuel engine VTOL counterparts. The design concept is to optimize C_L/C_D, since the range is the most crucial performance parameter. The aircraft has a higher speed, and wing loading than the trend line, and most of them operate in surveillance roles. In the case of "AeroeVTOL UAV Future" it has a lot more energy to consume, thus it is capable to reach further. Therefore it is able to achieve higher cruise speed and range than most of the eVTOL.

Figure 2.34: Scatter plot of Range vs MTOM of the VTOLs presented in table 2.4

Chapter 3

Methodologhy
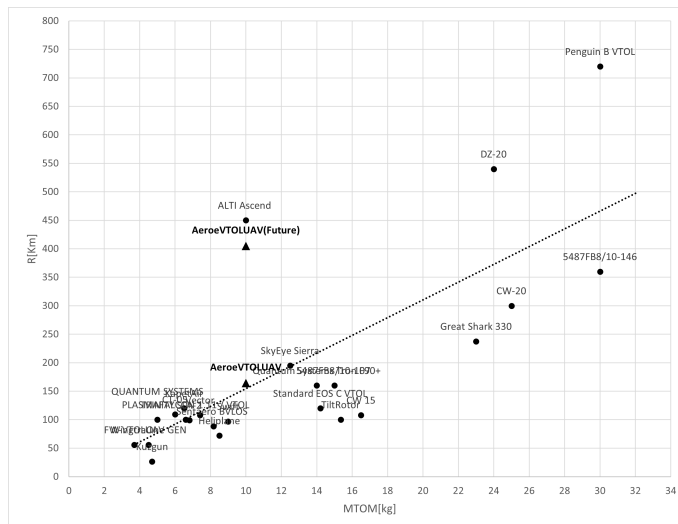
This chapter describes the methodology implemented from the conceptual design to the preliminary design.

In a summarized format, this dissertation has proceeded in the following stages:

1. Introduction of the eVTOL aircraft concept and objectives defined for the proposed aircraft design;

2. Determination of the problem-solving strategy to achieve the defined objectives;

3. Presentation of a literature review to set the theoretical fundamentals needed for the dissertation, historic background and a state of art regarding eVTOL, a study of the current battery technology capabilities and limitations, a brief market study for the helicopter and eVTOL and a framework of the eVTOL UAV project developed in relation with similar eVTOL UAV for the purpose of comparing the results and improve over some crucial design parameters;

4. Parametric study of the wing, first implementing a morphing aerofoil model, then the development of drag model accounting for the parasite and induced drag regarding all components, and obtain the empty mass initial results. Then iterating the program to obtain the optimal wingspan and optimal chord and then selecting a suited compromise of both parameters to define the wing;

5. Propulsion study using Prop Selector for the selection of propeller diameter and pitch values regarding hover lift performance (H) for the hover condition and the propeller global efficiency for cruise and climb conditions;

6. Tail sizing, and static stability study using XFLR5 for estimation of the trim angle of attack, a refined aerodynamic model and plots of C_m vs C_L, C_L vs V and the static margin;

7. Creation in OpenVSP software of the CAD geometry of the preliminary aircraft design;

8. Furthermore, development in CATIA V5 of an accurate CAD design for the transition device. Definition of a mission profile and execution of a performance study for the designed eVTOL.

3.1 Conceptual Design

This section reveals the methodology for the conceptual design phase of the eVTOL UAV aircraft. The adopted concepts are explained along with the main features of the design. These are then studied throughout the preliminary design to analyse the design capabilities and limitations. The figure 3.1 showcases the algorithm steps from the concept to the preliminary design, and the mission profile proposed for eVTOL UAV.

A simplified approach for the main configuration is adopted from the start. The designed aircraft is intended to be a prototype to test the performance capabilities of the eVTOL aircraft. Hence, many design choices were adopted within a flexible selection since the preliminary design mostly focused on the aerodynamics, propulsion, and performance of the aircraft.
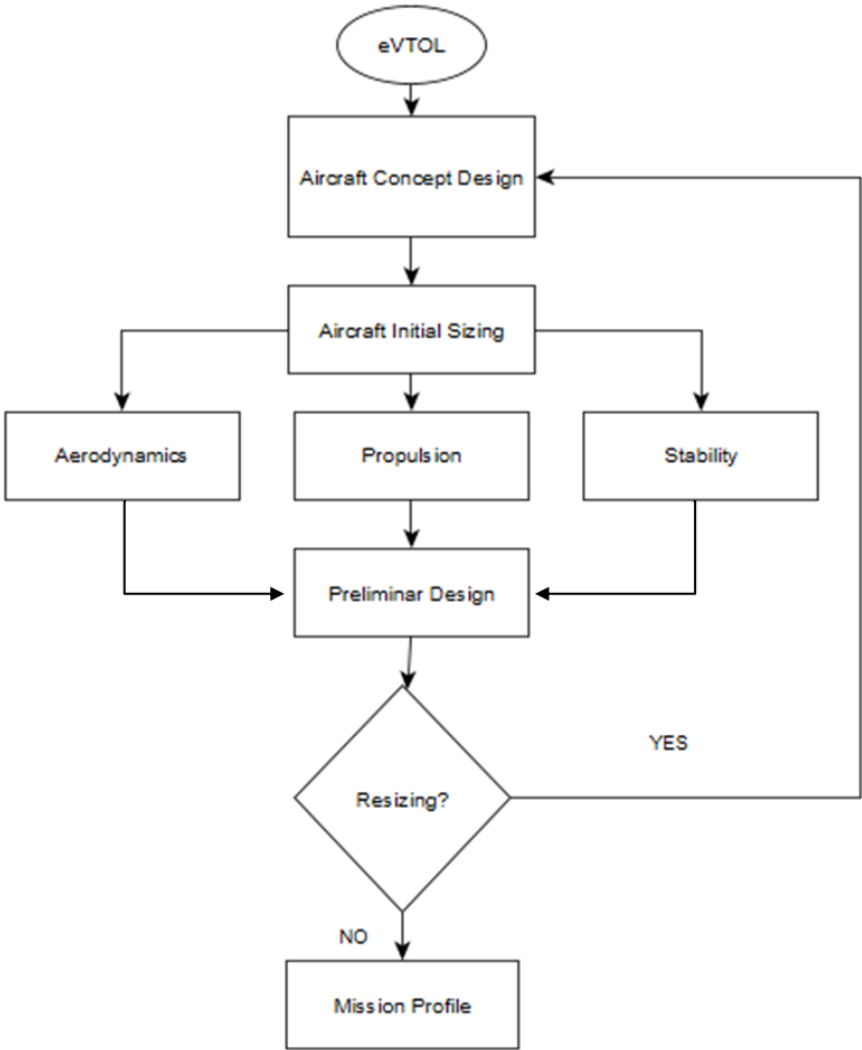

Figure 3.1: eVTOL Design Diagram

The design concepts implemented in the Aero eVTOLUAV are:

a) High wing for better lift distribution, latero-directional stability and clear space for cargo in the fuselage. With the following characteristics:
- Slightly tapered wing for structural reasoning, stability and manoeuvrability, less weight;
- Small wing incidence in line with the flow of minimal interference drag caused by the fuselage on the wing lift distribution;
- Simplified torsion box construction;
- High wing loading ratio for higher cruise speed, more range, and higher stall speed but the aircraft does VTOL therefore is not a crucial issue;
b) A bi motor tractor propeller configuration in the wings and pusher motor propeller at the back of the fuselage. Hence, a tricopter propulsion that also allows:
- Simple transition from the rotor to propeller configuration for the three electric motors;
- Vectored thrust system where all motors work in all stages of flight including the hover, climb and cruise conditions simultaneously;

c) A fully electric energy system, relying on a battery for sustainability. That is the case for a flexible propulsive system, with a small footprint and suitable for the mission profile. The battery mass is divided into three packs, distributed as two in the booms for the forward motors and one battery pack in the back of the fuselage, close to the electric motor. Figure 3.2 represents the framework of the proposed propulsion system. It is two tractor electric motors-propellers on the front and one pusher electric motor on the aft position. The front motors spin in opposite directions, hence, it is a tricopter configuration instead of the general quadcopter configuration. Two main reasons for the configuration lie in the operational effectiveness and decreased drag. In a quadcopter, at least motors are not required in the cruise condition. Keeping propellers stopped increases drag, and the tricopter is simpler.
- A flight controller responsible for the power management system (PMS), system monitoring, and pilot command is implemented. In case a battery pack fails, the energy from the others is supplied by a power bus.
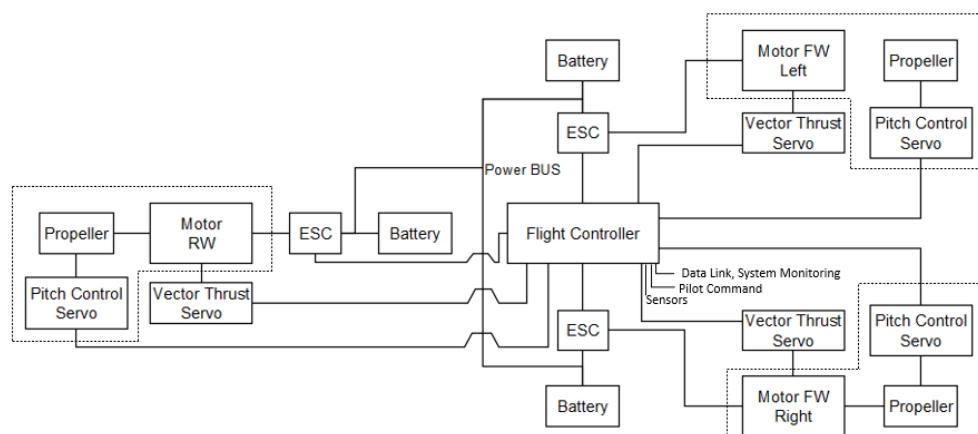

Figure 3.2: Propulsion System

d) Landing skid gear for airframe ground collision protection, smaller drag.

e) The booms are positioned near the outer panel section of the wing to diminish the effect of the front rotor disc-propeller interaction with the wings and fuselage.

f) Length of the fuselage is half the span of the main wing as most gliders.

g) The front motors booms extent to the back as tail booms to support the individual tail surfaces;

h) Inverted V-Tail mounted as the configuration wing tip tail (WTT). This configuration helps generating forward force and diminishing the induced drag[85]
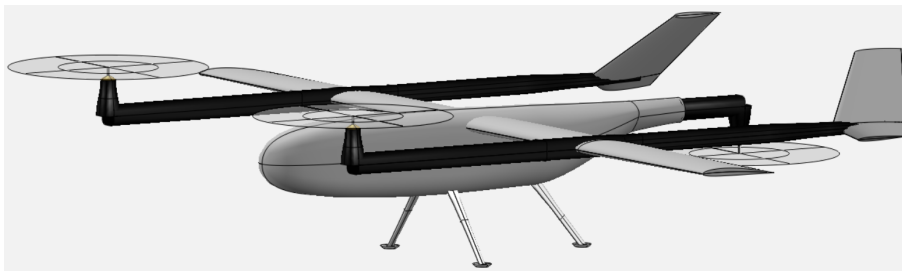
Figure 3.3: Aero eVTOL UAV ISO view

3.1.1 Software Tools

-Microsoft Excel

Microsoft Excel is a software that utilizes spreadsheets for organizing data, programming, data analysis and calculations. For the present work, this software was extensively used for calculations, iterations, graphs, and table comparisons.

-XFLR5

XFLR5 is an open source software created by André Deperrois and it was initially developed to serve as a friendly user interface version of the XFOIL code[86, 87]. Currently, beyond aerofoil analysis and design using the XFOIL code, XFLR5 also allows the aerodynamic and stability analysis of finite wings and fixed wing aircraft such as sailplanes and small UAVs, all operating in low Reynolds Number[86]. In this dissertation XFLR5, is used for static stability aerodynamic performance analysis.

-Open VSP

OpenVSP is a parametric aircraft geometry open source software tool created by NASA that allows the designer to create a 3D model of an aircraft defined by common engineer-

ing parameters[88]. This model then can be processed into formats suitable for engineering analysis. This software was utilized for development of the conceptual design and CAD model.

-CATIA V5

CATIA V5 , is a multiplatform software for CAD,CAM, CAE, 3D modelling and PLM made by Dassault Systèmes. This software is utilized for development of the preliminary design model of the frontal tilt rotor mechanism of the aircraft.

-Prop Selector

Prop Selector is a software made by Brian R. Gyles that allows the estimation of parameters as thrust, power, propeller efficiency and others for small aircraft propellers with two to four blades[89]. For the input the program utilizes the altitude, airspeed, RPM, number of blades, blade pitch and propeller diameter. The estimations does not account for the blade geometry, therefore an ideal geometry is assumed. The propeller data comes from NACA Technical Note 698[90]. Prop Selector was utilized for the estimation of the blade pitch, thrust, and shaft power and its variations through different flight conditions, in order to select the most suitable propeller diameter and pitch for the aircraft.

3.2   Aerodynamics and Stability

3.2.1   Aerofoil Theoretical Model

Generally, the aerofoil is chosen before the conception and aerodynamics study on the wing. That specifically limits the wing "sizing" to aerofoil's characteristics and may lead to unwanted results and step-backs over the design. Therefore a theoretical aerofoil model developed by Silvestre[91] is implemented with the effect of the lift coefficient, on the aerodynamic efficiency of the aerofoil function of Reynolds number hence, by implementing it into the parametric study of the wing, it is possible to estimate the wing drag coefficient, and lift distribution for our wingspan (b) and mean aerodynamic chord ($\bar{c}$), together without selecting initially an existing aerofoil. It is implemented through Equation (3.1). Subsequently, an existing aerofoil is selected or designed to match the performance results predicted by the model for the same wing planform. The Reduced Reynolds number ($Re\sqrt{C_l}$) is utilized to take into consideration that the Reynolds number decreases with increasing values of C_L, owing to decreasing airspeeds.

$$\frac{C_l}{C_d} = 58 \sin(1.4 C_l^{0.7}) \left(\frac{\log(Re\sqrt{C_l})}{\log(100000)} \right)^{5.5} \tag{3.1}$$

$$Re = \frac{\rho V_\infty \bar{c}}{\mu} \tag{3.2}$$

The air viscosity is $\mu = 1.789 * 10^{-5} kgm^{-1}s^{-1}$
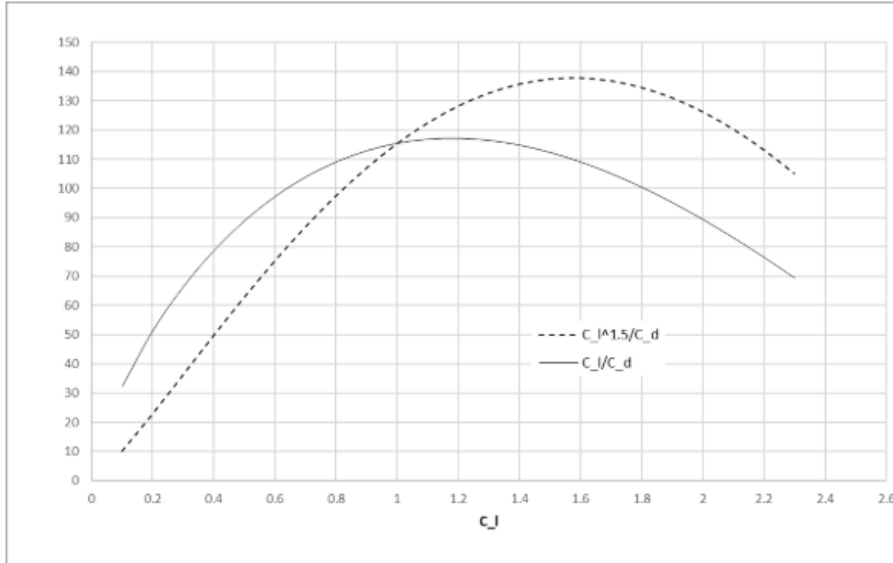
Figure 3.4: Morphing Aerofoil[91]

3.2.2 Drag

Drag is a crucial and complex parameter to study and estimate rightfully without wind tunnel testing or other expensive means. The drag study is usually divided into two groups: drag due lift (D_i) and parasite drag (D_0). To distinguish both drags were estimated through their respective coefficient as follows:

$$D = 0,5\rho V_\infty^2 S C_D \tag{3.3}$$

$$C_D = C_{D_i} + C_{D_0} \tag{3.4}$$

$$C_{D_i} = \frac{C_L^2}{\pi A e} \tag{3.5}$$

The parasite drag coefficient (C_{D_0}) on the aircraft components is estimated through empirical methods and observations. In a preliminary design it is suitable to go through empirical data and statistics. Thus, to obtain a close approximation for the contribution of parasite drag from the main airframe parts such as wing ($C_{D_{foil}}$), fuselage ($C_{D_{fuse}}$), tail ($C_{D_{emp}}$), and smaller components ($C_{D_{0Resto}}$) such as antenna, gimbal and others.
The parasitic drag coefficient equations are:

$$C_{D0} = C_{D_{foil}} + C_{D_{emp}} + C_{D_{fuse}} + C_{D_{0Resto}} \tag{3.6}$$

$$C_{D_{foil}} = f(C_L, Re) \tag{3.7}$$

42

$$C_{D_{fuse}} = C_f FF \frac{V_{fuse}^{\frac{2}{3}}}{S_{Ref}} \tag{3.8}$$

$$C_{D_{emp}} \approx 0,15 C_{D_{foil}} \tag{3.9}$$

$C_{D_{foil}}$ is dependent on the Reynolds number and the lift coefficient of the morphing aerofoil (Equation (3.7)). Equation (3.7) takes into account the incidence drag coefficient CD_i, caused by the lift generated on the main wing. The interference drag is included on the wing. This was assumed accordingly to Hoerner's book [92], which considers the interference drag relative to the wing area covered by the fuselage. That is represented Figure 3.5.
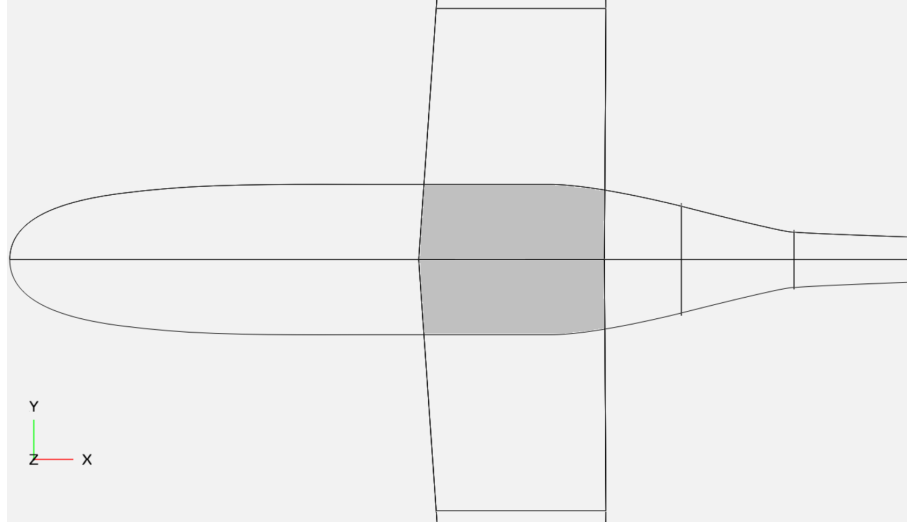
Figure 3.5: Interference Drag assumption.

For the estimation of the fuselage drag ($C_{D_{fuse}}$) Snorri, and Hoener methods are adopted [93, 94, 92] to compute form drag and friction drag. The method is based on the airship drag estimation, which relies on the fuselage body volume(V_{fuse}), concerning the reference wing area $V_{fuse}^{\frac{2}{3}}/S_{Ref}$ and the volumetric coefficient drag (C_{D_v}) [95]. C_{D_v} accounts for the friction drag and form drag of the fuselage. Although, the body has the volume required for the battery+payload inside the fuselage. Is then consider the fuselage volume as a box that encased it, so that is simplified the geometry, thus, simplifying calculations for the fuselage drag. Through these, mass $m_{container}$ that represents a mass of the box that encase the fuselage, and a reference density ρ_f are used to estimate the volume, V, for the fuselage compared with the geometric measure drawn in the Figure 3.6.
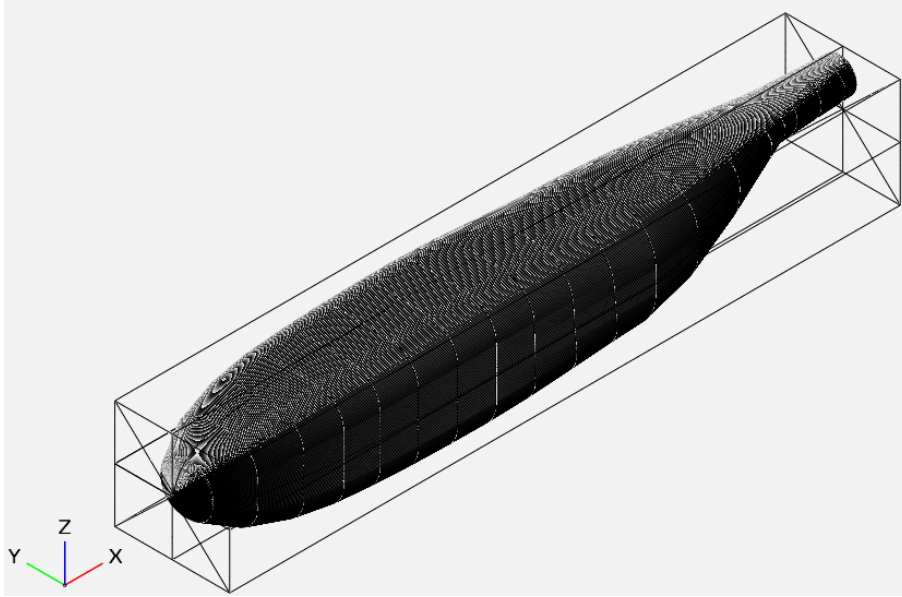
Figure 3.6: Container volume representation. Created in OpenVSP

The friction coefficient (C_f) was estimated for a turbulent flow regime (Equation (3.10)), used based on Raymer [14] empirical analysis. In most aircraft, the flow over the total wetted surface of the fuselage is turbulent, and the laminar flow may exist on the front 10 % to 20 % of the wing[14]. A carefully designed composite aircraft, such as the Piaggio GP 180, may exhibit laminar flow over 50 % of the wing and over 20 % to 35 % of the fuselage. Raymer 1992 suggests estimating the proportion of laminar flow for the aircraft in question in order to calculate a mean skin-friction drag. Although, in this aircraft, due to the small size and, thus, Reynolds number, it may have a significant part of the fuselage in the laminar regime, the friction coefficient Equation (3.10) is for the case of fully turbulent regime.

The form factor (FF) is also very relevant to find $C_{D_{fuse}}$ value. It is most reliant on the fineness ratio of the fuselage. Based on Gotten studies which have shown that the higher the fineness ratio, the higher the friction drag in relation to the form drag[96], especially with a fineness ratio (l_f/d_f) above 6. Therefore a $l_f/d_f = 6$, is given to avoid higher fuselage drag due to friction. Equation (3.11) is the rearranged Hoener empirical equation for form drag[95]. Another note is that most empirical equations such as Hoerner, Snorri, and Raymer do not estimate accurately the fuselage drag when the fineness ratio is under 5[96]. The length of the fuselage was obtained, through statistical trends estimated for other existing small UAV fuselages.

Altogether, $C_{D_{fuse}}$ results in Equation (3.8). Thus fuselage drag still has an important contribution to the drag of the entire aircraft, an increase in the amount of payload adds more container space, therefore a bigger fuselage must be constructed, resulting in more drag.

44

$$C_f = \frac{0,455}{((\log Re))^{2,58}(1 + 0,144M^2)^{0,65}} \tag{3.10}$$

$$FF = 4(l_f/d_f)^{\frac{1}{3}} + 6(l_f/d_f)^{-\frac{7}{6}} + 24(l_f/d_f)^{-\frac{8}{3}} \tag{3.11}$$

The tail drag $C_{D_{emp}}$ is considered 0.15 $C_{D_{foil}}$. Since tail parasite drag accounts on average for around 10 % to 15 % of total parasite drag of the wing, and the tail geometric characteristics are not known yet.

The remaining profile drag, $C_{D_{0Resto}}$ accounts for other interference drag on the aircraft, nacelles, propeller drag, antenna, landing gear, tail boom etc. For simplification $C_{D_{0Resto}}=35\%C_{D_{fuse}}$ is considered.

3.2.3 Wing Geometry

The morphing aerofoil presented in Section 3.2.1 places the aerofoil characteristics for the aircraft to estimate the wingspan b, the wing mean chord ($\bar{c}$), and lift coefficient C_L. Thus, as an initial guess, it is unknown what is the best combination of those parameters for the wing design to be selected. An objective function is then required to guide the parametric study over the result analysis and selection of wingspan and mean chord value. The selected objective function for this parametric study was the lift-to-drag ratio times the payload mass for the aircraft $m_{pay}\frac{C_L}{C_D}$. Since the aircraft's role is payload transportation, it is enhanced for the best range. This allows improvements in aerodynamic efficiency and increase in carrying capacity.

Multiple combinations of mean aerodynamic chord, wingspan and lift coefficient are studied. Hence the ideal value for the aerodynamic chord and a wingspan are estimated. That results in the highest score of the objective function. Figure 3.7 introduces the steps implemented to achieve the optimal mean chord and wingspan as well as lift coefficient.

Firstly, four chords were input and each had the wingspan variation in 40 partitions from a range $[b_0; b_{40}]$. Since first iteration onwards, a C_L from a range of $[0.4; 2]$ is selected[91]. Then, the best chord is selected as the one with the highest $m_{pay}\frac{C_L}{C_D}$. Afterwards, the value for the wingspan that matched previously with the best chord but now with the chord varying in 40 partitions $[c_0; c_{40}]$ are calculated. These iterations are repeated until a combination for the wingspan and chord that results in the best $m_{pay}\frac{C_L}{C_D}$ is reached. Equations (3.12), (3.14) , (3.15) are utilized to study these parameters.

$$i, j, k = 0, .., 40 \tag{3.12}$$

$$c_j = c_{min} + j \left[\frac{c_{max} - c_{min}}{j_{total}} \right] \tag{3.13}$$

$$b_k = b_{min} + k \left[\frac{b_{max} - b_{min}}{k_{total}} \right] \tag{3.14}$$

$$C_{Li} = C_{Lmin} + i \left[\frac{C_{Lmax} - C_{Lmin}}{i_{total}} \right] \tag{3.15}$$

Furthermore, a table with combinations of multiple wingspan, mean chord and lift coefficient is created (see Section 4.1). After assembling enough combinations, the actual optimal wingspan, and mean chord combination with the best objective function result among the many combinations with each different lift coefficient is selected. Relevant graphs like the $\frac{CL}{CD}$ vs C_L and objective function are plotted to help in the selection of the design span, chord and lift coefficient.
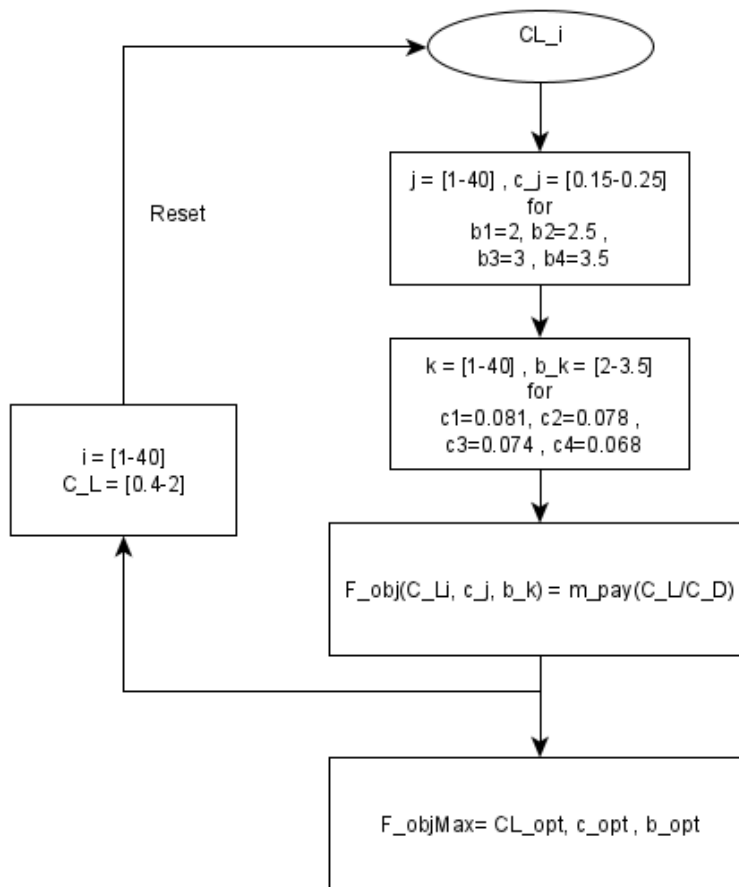

Figure 3.7: Parametric study schematic for wing design

46

Although, the main objective is to find the best wingspan, mean chord and aerofoil design lift coefficient, the selected design point from the parametric study data may result in an unpractical wing to be built due to high aspect ratio, and consequently, a too short chord (see Section 4.1). Hence, two parameters $Floss_{opt}$ and Fc_{var} are introduce to measure the losses:

$$Floss_{opt} = 1 - \frac{m_{pay}\frac{C_L}{C_D}}{\left(m_{pay}\frac{C_L}{C_D}\right)_{opt}} \tag{3.16}$$

$$Floss_{opt} <= 0.15 \tag{3.17}$$

$$Fc_{var} = 1 - \frac{\bar{c}}{\bar{c}_{opt}} \tag{3.18}$$

$$AR <= 15 \tag{3.19}$$

3.2.4   Empty Mass Model

The empty mass model is implemented to estimate the mass function of the size and payload of the aircraft [91]. Therefore, all parameters in Equation (3.20) are determined through structural construction tests, known aircraft statistical data, and material used for the structure[91].

$$m_{empty} = m_{ref}\left(\frac{\bar{c}}{c_{ref}}\right)^{e_c}\left(\frac{\bar{b}}{b_{ref}}\right)^{e_b} + m_{sys} \tag{3.20}$$

This model estimates the mass of the aircraft structure depending on the wing geometry and accounts for the initial guess for the mass of the systems (wires, sensors, propeller, etc), m_{sys}. The m_{ref} is a reference airplane structure mass with the same structure concept (same construction concept and materials), b_{ref} and c_{ref} are the respective span and mean chord. The exponents e_{bref}, e_{cref}, represent the non-linearity of the empty mass function with the airplane span and chord [91].

3.2.5   Stability

3.2.5.1   Tail Sizing

The aircraft stability study begins with the tail volume coefficient estimation. The volume coefficients (c_{VT} and c_{HT}) are set through statistical data of common airplanes, and L_{VT} and L_{HT}, represent the tail arms ,i.e. the distance from a quarter of chord of the wing to a quarter of the chord for each tail surface(see Equation (3.21) and (3.22))[14]. This concept is a first approximation to guess whether the aircraft may achieve or not a stable condition. Later on, more suited analyses to conclude that the aircraft will operate in stable condition are necessary.

Figure 3.8 shows the projected areas method used for the V-Tail sizing. Since the tail volume coefficients would come from statistical data of general airplanes values, the tail arm is assumed as 60 % of the length of the fuselage as proposed by Raymer [14]. Then both tail area surfaces S_{VT} and S_{HT} are estimated with the following Equations (3.21) and (3.22):

$$S_{VT} = \frac{c_{VT} b_W S_W}{L_{VT}} \tag{3.21}$$

$$S_{HT} = \frac{c_{HT} \bar{c}_W S_W}{L_{HT}} \tag{3.22}$$
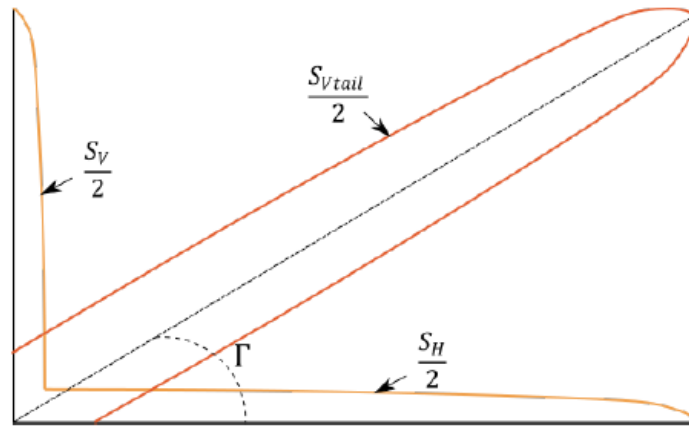
Figure 3.8: V-Tail projected areas method[97]

Both projected areas are estimated and then converted into the V-Tail surface area of the aircraft. In theory, the V-Tail is equivalent using 'Pythagoras theorem' to the square root of both square surface areas resulting in near 70 % of the resulting tail surface area (Equation (3.23)). However, according to NACA 823 report [98], the V-tail surface area must be larger than whatever is estimated in theory to maintain the same efficiency, resulting in Equation (3.24).

The dihedral angle from the surface areas is estimated, since the V-Tail is the sum of both projected areas, the dihedral angle (Γ) is the square inverse tangent of those surface areas projected (see Equation (3.25)).

$$S_{V_{tail,theory}} = \sqrt{S_H{}^2 + S_V{}^2} \tag{3.23}$$

$$S_{V_{tail}} = S_H + S_V \tag{3.24}$$

$$\Gamma = \arctan^2 \left(\frac{S_V}{S_{V_H}} \right) \tag{3.25}$$

Moreover, the V-tail span and mean chord are estimated for its geometric shape. The aspect ratio of the horizontal tail should always be less than half the aspect ratio of the wing. Yet, the aspect ratio is unknown. An approximated value for the aspect ratio from Raymer data for the horizontal and vertical tail from general airplanes[14] it is then assumed. Since lower aspect ratio wings generally stall at higher angles of attack, the horizontal stabilizer should have a significant lower aspect ratio depending on the wing such that the elevator is capable of stall recovery after the wing has stalled[99]. Thus, following this condition to the V-Tail, the assumptions then result in Equations (3.26), (3.27).

$$b_{V_{tail}} = \sqrt{S_{V_{tail}} A_{V_{tail}}}$$ (3.26)

$$\bar{c}_{V_{tail}} = \frac{b_{V_{tail}}}{A_{V_{tail}}}$$ (3.27)

Henceforth, a wing and plane analysis using XLFR5 software to find the actual aerofoil is performed, a more precise aerodynamic efficiency prediction and study the pitching moment coefficient in function of the lift coefficient, seek the trim AOA condition, and overall behaviour of the aircraft within the fixed wing mode in longitudinal static stability.

3.2.5.2 Transition of Vertical Flight to Horizontal Flight

In order to improve the transition phase from vertical flight to horizontal flight, it is imperative to seek the shortening of the transition time phase as much as possible. A fast transition reduces energy consumption significantly when possible, to turn over a stable mode with safety, either fixed-wing or VTOL mode.

The eVTOL configuration is significantly complex to study and it is uncertain to improve its transition phase in preliminary design stage . Hence, the focus is on optimized level-flight performance, such as cruise speed, range, and aerodynamics efficiency. Since most of the flight operation occurs the FW mode conditions. This design approach consequently may result in relatively poor flight characteristics when operating in the transition mode due to lack of study and optimization in this flight stage.

It is intended that the transition phase is dependent on a control system for airworthiness throughout this phase. The capability for near-ground landing operations is also relevant in VTOL to FW wing mode. An Extended State Observer (ESO) control module of the Active Disturbance Rejection Control (ADRC) assists in altitude fluctuation reduction in a fast mode transition. This device allows the aircraft to improve lateral stability at low altitudes and in limited airspace and clearance. [100]. Figure 3.9 represents the a concept CAD model of the tilt rotor mechanism. Is desired a streamline body to reduce friction drag and weight with a coupled system inside the cage. It will rely on servos causing momentum into a transition arm to switch modes. It will also need a damping system to calibrate for small angles when in vertical flight, so that the aircraft hover can maintain

equilibrium.
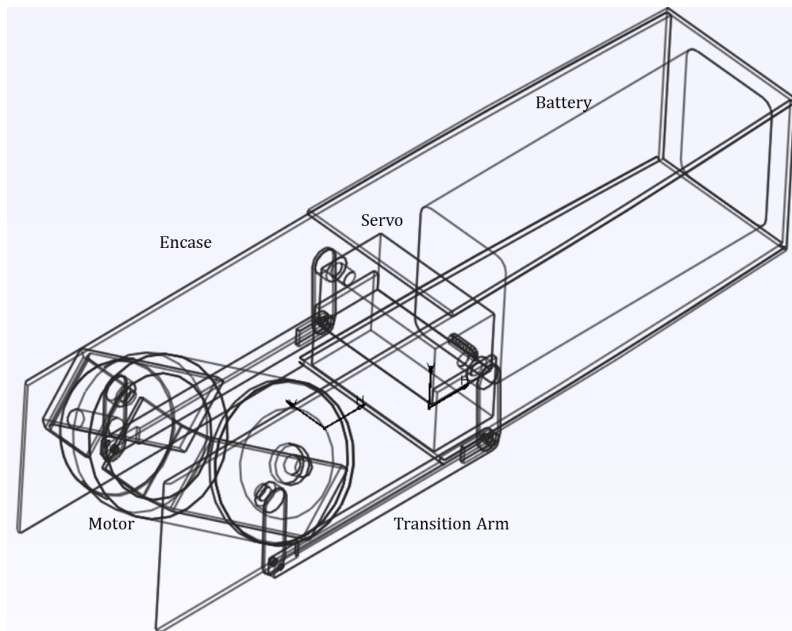
Figure 3.9: Tilt Rotor Mechanism

The propulsion configuration of a tricopter system has to account for the dissymmetry of torque. It has two motors producing anti-clockwise torque and one operating clockwise. There is a lack of counterbalancing in the yaw axis if all are perpendicular to the horizontal axis (in 90◦). Thus the deflection angle for the transition shaft device supporting the forward motors in the vertical flight phase is estimated. To maintain a balanced torque and a steady vertical flight phase (Figure 3.10).
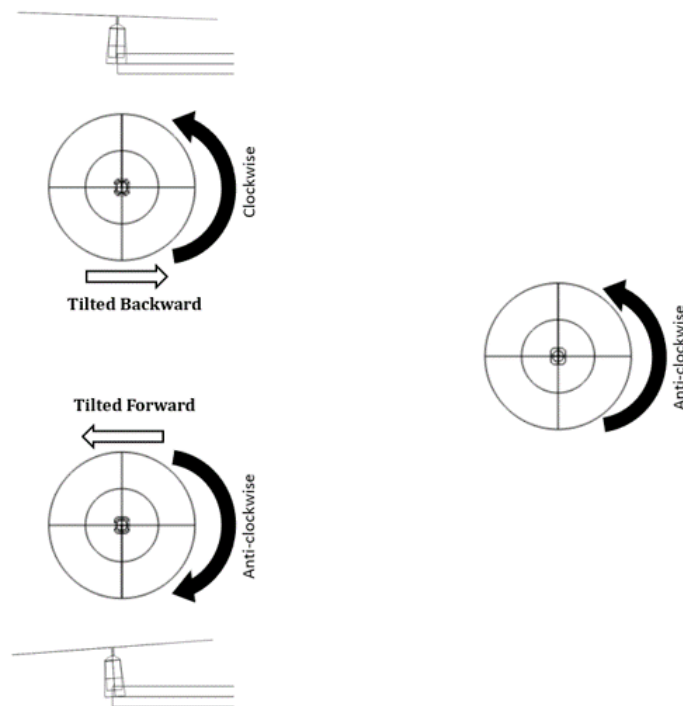
Figure 3.10: Dissymmetry of torque and frontal rotors equilibrium tilt angle

3.3 Propulsion

The aircraft propulsion was defined through the study of its propeller's main parameters that are the disc diameter and blade pitch coupled to the electric motor. The electric motor must supply enough power output for the VTOL operation and work with low disc loading and motor rpm with efficiency. Therefore the electric motor selected was AXI GOLD Line 2835 (see motor specifications Appendix A.1).

The "sizing" of the propeller, hence, the diameter and blade pitch of the propeller and the resulting thrust (T), P_{shaft}, motor angular speed (ω_{motor}), are estimated using *"Prop Selector"* software. Three different conditions were studied, when operating the aircraft in VTOL mode, in hover and two conditions were in the fixed-wing mode in cruise and full power climb. Equation (3.28) and (3.29), are the general constraints implemented for the simulation to work. The output coming from the software are the shaft power and motor and must match with the calculations made in the spreadsheet.

$$\omega_{shaft} = \omega_{motor} \tag{3.28}$$

$$P_{shaft} = P_{Motor} \tag{3.29}$$

In the propulsion modelling, the two parameters P_{Shaft} and ω_{shaft} are calculated and considered inputs from the electric motor specifications. In the first stance, the input for the "Prop Selector" becomes a guessing diameter, blade pitch, and ω_{motor}. The outputs are T, P_{shaft}, and the propeller efficiency (η_p). The following equations describe the calculations in the spreadsheet for the necessary parameters. Where U_{bat} refers to the battery voltage, U_{nom} is the nominal voltage proportional with the battery efficiency (η_{bat}) . For the motor torque (Q) it is necessary to find the induced voltage (U_i), effective current (I_{eff}) with the motor specific constant velocity (k_v) and no-load current (I_0). As result, Q with the ω_{motor} calculates the shaft power output (P_{motor}) estimated from the spreadsheet (see Equation (3.35)).

$$U_{bat}[V] = \eta_{bat} U_{nom} \tag{3.30}$$

$$U = U_i + I_{eff}R \tag{3.31}$$

$$U_i = \frac{1}{kv}\omega_{motor} \tag{3.32}$$

$$I_{eff} = \frac{U - U_i}{R} \tag{3.33}$$

$$Q = \frac{I_{eff} - I_0}{kv} \tag{3.34}$$

$$P_{Motor} = Q\omega_{motor} \tag{3.35}$$

The global efficiency (see Equation 3.39) is considered the most important parameter for the propulsive system. Through global efficiency maximization, the best blade pitch for a propeller diameter is selected according to the airspeed. The hover lift perfor-

mance (H), defines the best blade pitch and diameter for the hover condition (see Section 4.3).Equation (3.40) is obtained from electric power(P_{ele}) from Equation 3.37 with the input T. The global efficiency(η_{global}) accounts: the efficiency from the motor (η_m) and propeller (η_p).

$$\eta_p = \frac{T v_{\text{inf}}}{P_{Shaft}} \tag{3.36}$$

$$P_{elef} = I_{eff} U_i \tag{3.37}$$

$$\eta_m = \frac{P_{Shaft}}{P_{elef}} \tag{3.38}$$

$$\eta_{global} = \eta_m \eta_p \tag{3.39}$$

$$H = \frac{T}{P_{ele}} \tag{3.40}$$

The propeller design must sustain the three flight conditions, it is a priority for the designed propeller, the operation in VTOL mode due to the higher energy consumption. The methodology used to select the best propeller pitch and diameter changes according to the flight mode, though the same propeller diameter must be selected for both flight modes. Hereafter, the blade pitch must differ to fulfil the power and global efficiency requirements for all flight conditions, resulting in a variable pitch configuration. A variable-pitch propeller configuration fits better for efficiency and flexibility when operating in different flight regimes.

Diagram 3.11 represents how the propeller diameter and its blade pitch are selected for VTOL mode. The constraints in Equations (3.28) and (3.29) are implemented, and new are introduced to the algorithm as follows:

$$T = T_{hover} = \frac{W_{MTOM}}{n_{motors}} \tag{3.41}$$

$$I/I_{max} <= 0.95 \tag{3.42}$$

$$V < V_{max} \tag{3.43}$$

The first condition is that the thrust fixed of each propeller equals one-third of the aircraft's weight since it is in hover. Then the power shaft and resulting (H), for a diameter with a range of different blade pitches are calculated. The higher the current becomes, the higher the electric power and the heat from the electric motor. To avoid much strain and damage to the electric motor, the electric current is limited by the throttle to satisfy the condition in Equation (3.42). Voltage above the motor specifications results in excessive ω_{motor}. Thus it must always be lower than V_{max}. Meantime the best propeller pitch is estimated for each diameter and compared to the best H for each diameter in a plot of hover lift parameter versus blade pitch (P_b).
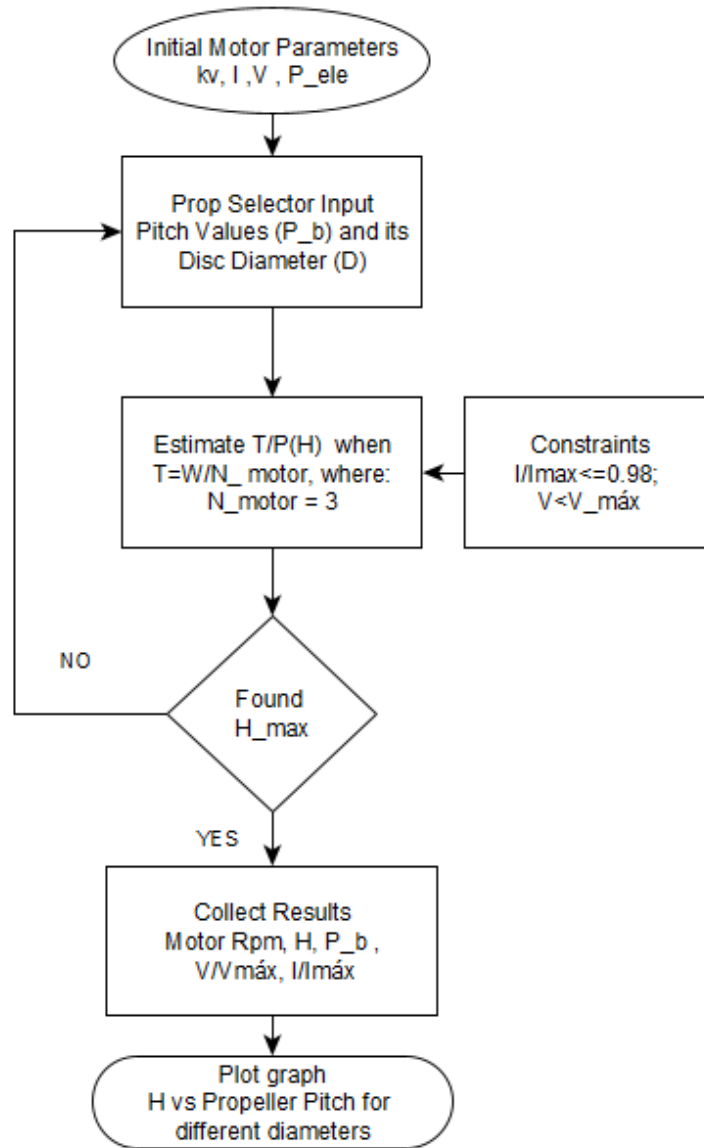
Figure 3.11: Propulsive Rotor Diagram

In this stage the diameter is almost chosen. The best diameter must have fair results in H and n_{global} in FW mode. The best compromise between the two will become the selected propeller diameter. In the FW mode, the best pitch was studied for the range of airspeed $\left[0; 64\frac{m}{s}\right]$.

The propulsive steady flight study diagram in Figure 3.12, describes the algorithm implemented for estimation of the propeller pitch and diameter in the fixed-wing mode, cruise condition. Furthermore, the results are plots of the global efficiency function of airspeed and respective blade pitch versus the airspeed. The constraints in Equations (3.28) and (3.29) are implemented along with Equation (3.44)

$$T_{req} = D \tag{3.44}$$
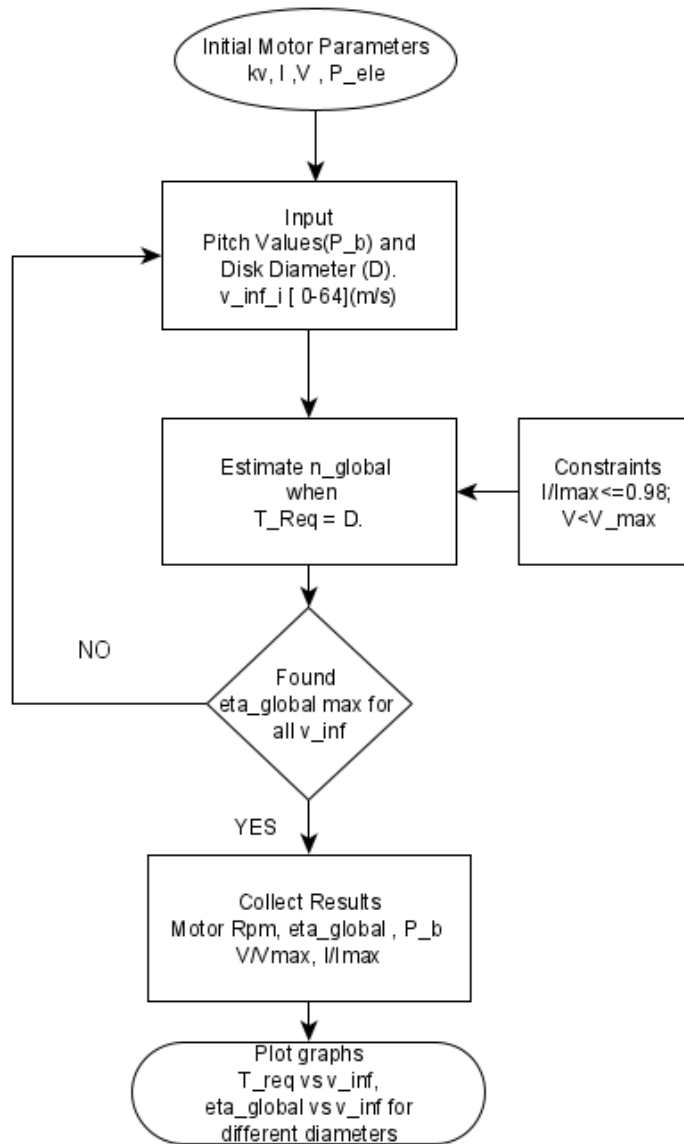
Figure 3.12: Propulsive Cruise Steady Flight Diagram

The condition of Equation (3.44) is implemented since, in the cruise flight, the thrust required is known as the aircraft in cruise from the Section 3.2.2 and is equal to the thrust available generated by the three propellers. Hereafter, the parameters shaft power and global efficiency are calculated for different airspeeds.

Subsequently, the diameter was selected to match between both flight regimes from the diameter range that was calculated. Then the plots of H vs P_b and n_{global} vs v_∞ for hover and cruise flight are plotted respectively. Frequently the best cruise propeller in global efficiency has a lower disc diameter than the best rotor diameter in H (see Section 4.3).

The climb condition was studied using the algorithm shown in Figure 3.13. The objective is to find the maximum available thrust versus airspeed and its power for the climb flight. In addition, the results for the global efficiency and propeller pitch function of air-

speed are plotted. Therefore, the constraints introduced correspond to Equations (3.28), (3.29) and (3.45).

$$I = I_{max} \tag{3.45}$$

The electric current must be at the maximum value allowed for the motor since with this constraint the maximum power available to climb at a given airspeed is achieved. Afterwards, the graph of thrust available related to the airspeed, global efficiency in climb versus airspeed, and the propeller pitch in climb versus airspeed are plotted.
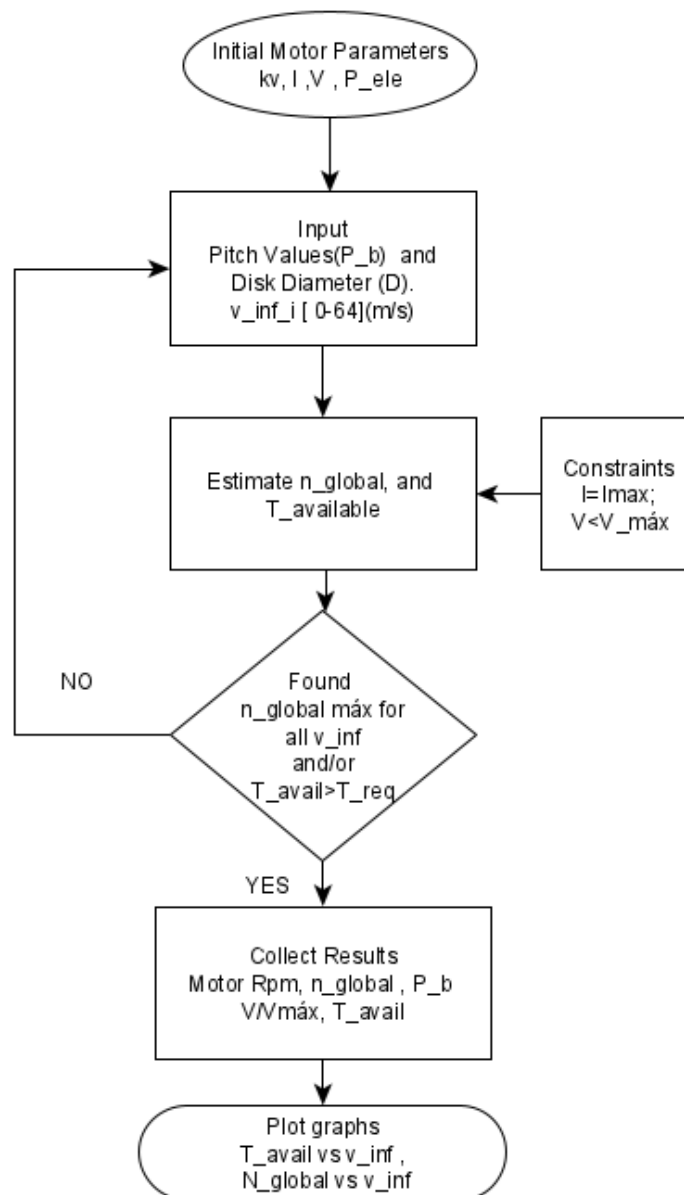
Figure 3.13: Propulsive Climb Flight Diagram

Chapter 4

Results/Discussions

4.1 Aerodynamics

In this section the results from wing sizing will be discussed along with the study of the static longitudinal stability of the aircraft.

Table 4.1 presents wingspan and mean chord, iterated multiple times for the selection of the most suitable wing size. It is seen that the best objective function (F_{obj}) is achieved on iteration 9. Furthermore, it is complicated to build a wing with an aspect ratio (AR) above 20, especially with such a very short chord. Accordingly, the structural integrity could be an issue. Moreover, the booms attached at the outer wing would have less area for support, therefore, the connection between wing structure and the boom, could be weak. Hence, the combination of iteration 19 with AR around 10, resulting in a mean chord much more reasonable is selected as the design point of the aircraft wing. The $Floss_{optimal}$ of 12 % means that the F_{obj} at this iteration is 12 % lower than the $(F_{obj})_{optimal}$.

Table 4.1: Wing iterated for best objective function

IT	c [m]	b [m]	C_L	F_{obj} [kg]	V [$\frac{m}{s}$]	AR	W/S [$\frac{kg}{m^2}$]	$Floss_{opt}$	Fc_{var}
1	0.0515	2.335	2	53.1	25.802	45.34	83.15	0.1004	-0.348
2	0.0560	2,4075	1.8	55.719	25.686	42.99	74.17	0.0560	-0.291
3	0.0585	2.4225	1.7	56.73	25.779	41.41	70.56	0.0389	-0.259
4	0.0615	2.4375	1.6	57.553	25.837	39.63	66.70	0.0249	-0.221
5	0.0650	2.445	1.5	58.194	25.916	37.62	62.92	0.0141	-0.177
6	0.0690	2,4575	1.4	58.654	25.97	35.62	58.97	0.0063	-0.126
7	0.0738	2.45	1,3	58.934	26.108	33,22	55.34	0.0015	-0.066
8	0.0768	2,4525	1.25	59.003	26.086	31.95	53.12	0.0004	-0.028
9	0.0790	2.4475	1.2	59.027	26.269	30.98	51.72	0.0000	0.0000
10	0.0825	2.44	1.15	59.001	26.299	29.58	49.68	0.0004	0.044
11	0.0860	2.4375	1.1	58.924	26.351	28.34	47.70	0.0017	0.088
12	0.0935	2.4125	1	58.614	26.642	25.80	44.33	0.0070	0.183
13	0.1025	2.3875	0.9	58.072	26.962	23.29	40.86	0.0161	0.297
14	0.1150	2.35	0.8	57.269	27.213	20.43	37.00	0.0297	0.455
15	0.1225	2.335	0.75	56.755	27.319	19.06	34.96	0.0384	0.550
16	0.1500	2.25	0.6	54.68	28.119	15.00	29.63	0.0736	0.898
17	0.1625	2.215	0.55	53.771	28.439	13.63	27.78	0.0890	1.057
18	0.1775	2.1775	0.5	52.727	28.784	12.27	25.87	0.1067	1.246
19	0.1975	2.14	0.45	51.524	29.014	10.84	23.66	0.1271	1.500
20	0.2200	2.08	0.4	50.137	29.576	9.45	21.85	0.1506	1.784

The empty mass model adopted some exponential values that did not adapt correclty to the wing characteristics. Though there is a loss in performance, it is accepted since the

chord selected difference from the optimal chord (Fc_{var}) increases 150 % and such value c=0.1975 m of iteration 19 versus c=0.079 m of iteration 9 being a far more reasonable value allowing enough room for the wing structure. As seen, the cruise speed (v_{cr}) respective to C_L/C_D also increases from 26.26 m/s to 29 m/s.

Figure 4.1 shows the graphical representation of F_{obj} vs C_L corresponding to the data of table 4.1. Note that each C_L value design point corresponded to the b, c combination that maximizes F_{obj}. It seems that the lift coefficient always improves F_{obj}. However, when reached C_L=1.2, which also coincides with the maximum aerodynamic efficiency of the morphing foil model, F_{obj} starts decreasing gradually as the lift coefficient increases (see Figure 4.1).
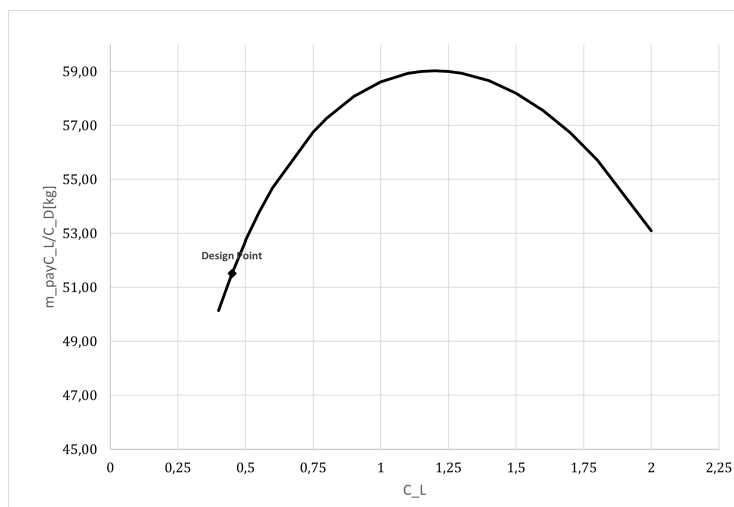

Figure 4.1: Objective Function vs C_L

Figure 4.2 shows the pattern, clearly observed previously in Figure 4.1. The chord variation is slim around lift coefficients near 1.2 but increases dramatically when the design lift coefficient is reduced below 1, but a modest decrease in F_{obj} is observed. Some factors that may contribute to this are the morphing aerofoil model behaviour being affected by the corresponding higher Reynolds number of a larger wing chord. However though F_{obj} decreases for lower lift coefficient, the chord increases at a higher pace. Therefore, the compromise must be that MAC has a higher value to prevent problems to implement the wing structure, and the trade-off for lowering F_{obj} was selected as the design point mark in the graph for a more suitable mean chord value.

The wingspan has the least effect on the result of F_{obj}, since the mean chord significantly influences the Reynolds number (see Equation (3.2)), along with the lift coefficient, both influence the most F_{obj}. Figure 4.3 shows F_{obj} in relation to the wingspan. Increasing the wingspan also increases F_{obj}, resulting in the chord diminishing gradually, and eventually reaching maximum F_{obj} at C_L=1.2 but then the wingspan decreases as the chord gets extremely small at very high lift coefficients, where the structure mass model penalizes the payload by estimating an increasingly high empty mass for the aircraft(see

appendix A.2).

A shorter wingspan for a limited chord adds wing loading , which also increases cruise speed for the aircraft. Nevertheless, the corresponding stall speed increase for higher wing loading, in this case, is not an issue because the aircraft is of the VTOL type.

The chosen compromise design point brings down the empty mass, resulting in more payload for the aircraft. That explains why F_{obj} is not so penalized when the chord increases dramatically at low design lift coefficient. The wingspan decreases and diminish significantly the F_{obj} value in comparison with $(F_{obj})_{opt}$.
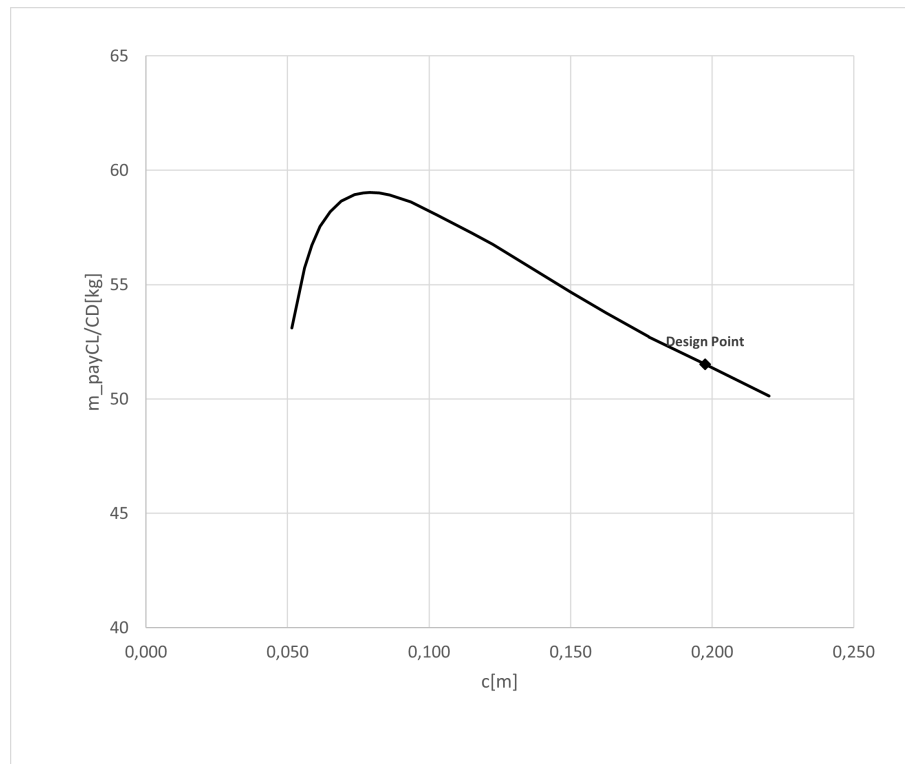

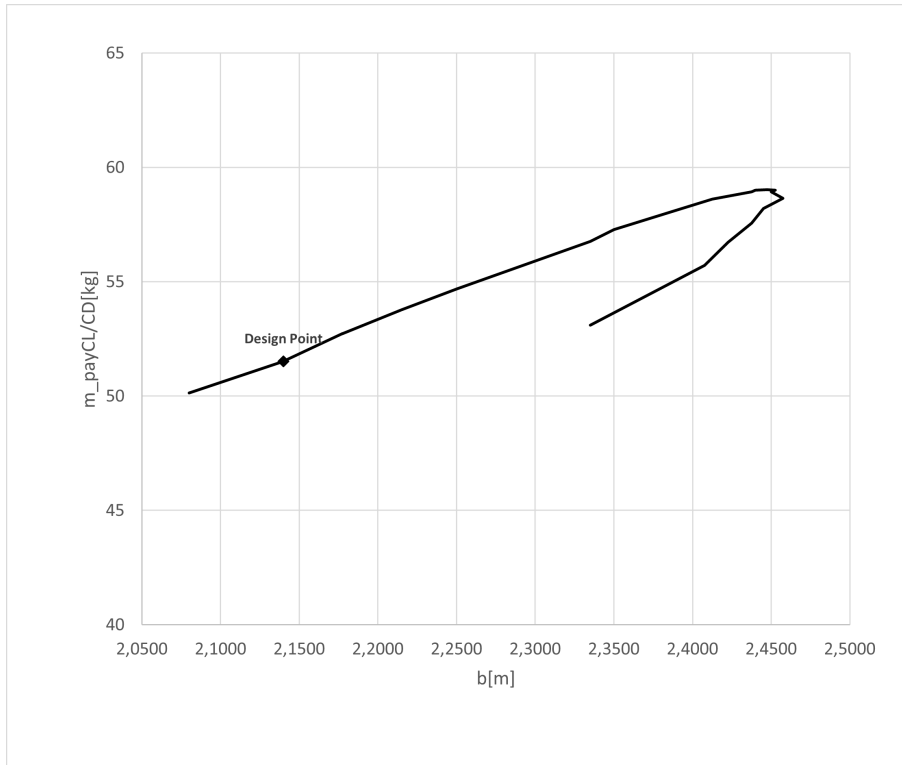Figure 4.2: Objective Function vs MAC

Figure 4.3: Objective Function vs Wingspan

At this stage the morphing aerofoil is still used to estimate the wing performance. A real aerofoil is chosen based on the design point aerofoil characteristics: $Re\sqrt{C_L}$, $\frac{C_l}{C_d}$ and c_l. Hence, the real aerofoil was selected from a list of some known aerofoils and chosen the one with the most similar characteristic values to those predicted by the morphing aerofoil model function. These characteristics were: aerofoil best $\frac{C_l}{C_d} > 75$ with c_l=0.6 at $Re\sqrt{C_L}$ = 263214.5. Hence, the most similar aerofoil from the list in comparison was the Selig 9000 (the black curve), and thus, chosen for further analysis.
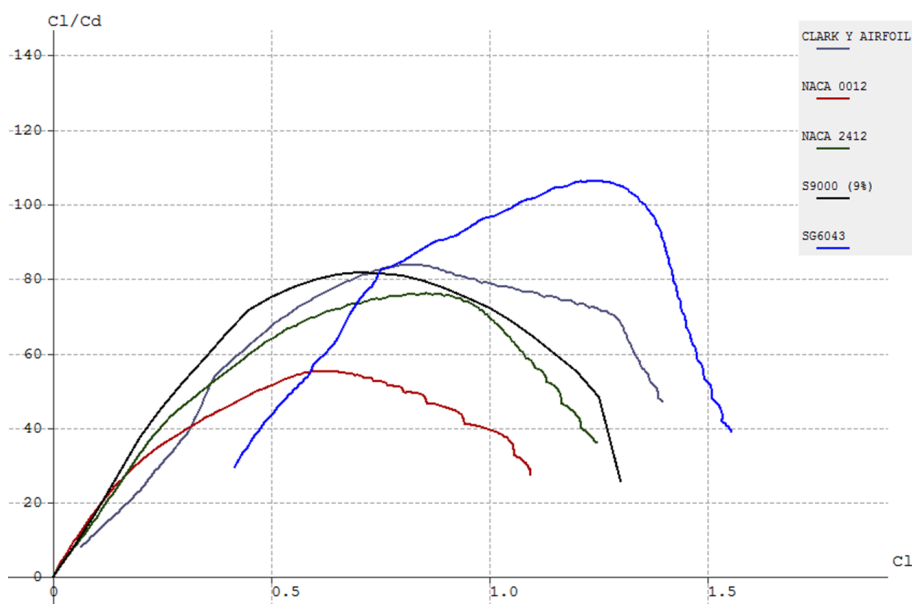

Figure 4.4: C_l/C_d vs c_l plot predicted by XFOIL.

4.2 Static Longitudinal Stability

The tail sizing is completed in this section. It is then introduced into XLFR5 to start the C.G positioning. The tail arm is 0.7 m and the tail volume coefficient is 0.5.

The C.G estimation is found based on the weight and device positions on the aircraft. It assumes a weight value for main components and the battery packs since these are the heaviest components, divided by three packs placed near each motor-propeller of the aircraft, all three packs combined are 4 kg.

The results from XFLR5 show that the selected aerofoil is working and adapted to the morphing aerofoil applied early. In Figure 4.5 the behaviour of the pitching moment related to the aircraft lift coefficient is plotted. The values of C_M are negative after angle of attack reaches around 1 degree (Figure in Appendix A.11), for C_L larger than 0.6. Thus, C_m is zero and the aircraft is in equilibrium when C_L is 0.6. The pitching moment curve shows an almost linear behaviour and the aircraft is trimmed for a flight speed of about 22 m/s. Therefore, it is necessary to modify the incidence angle on the V-tail to reduce the the trim lift coefficient, bringing the trim condition to when C_L is around 0.30 (lower line in the graph). At that lift coefficient, the flight speed is near 29 m/s, which increases the actual range of the aircraft (as shown in Section 4.4).

Furthermore, the aircraft neutral point was found close to x=572 mm, resulting in a static margin of approximately 10 %. It is purposely arranged for this value, so that manoeuvrability and stability in steady flight would be balanced. Henceforth, the C.G position is at 32 % the quarter of the chord.

So, deflecting the tail incidence angle from $0°$ to $1.5°$, changed the trim flight condition to lift coefficient near 0.3, thus, cruise speed near 29 m/s. However, such adjustment of tail incidence angle is considering, in theory, an all moving tail. In practical application a flap surface area near 30 % of the tail chord is more likely to be implemented.
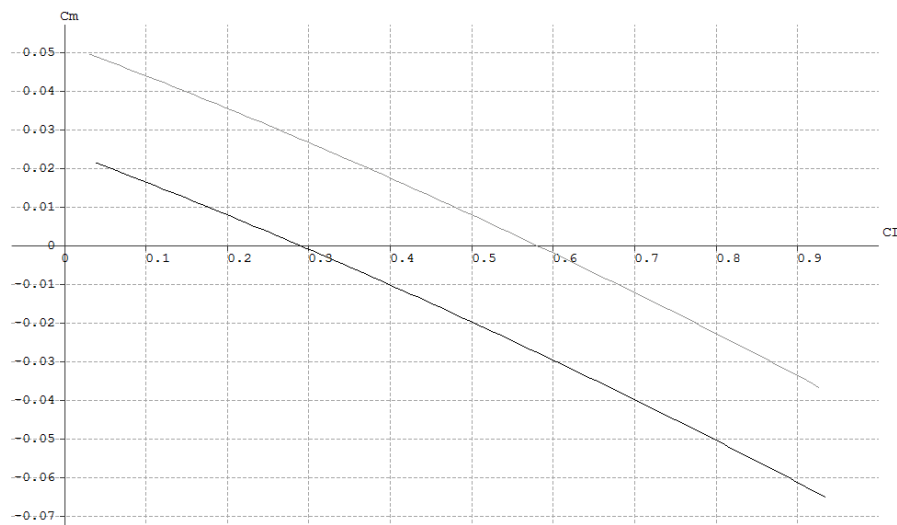

Figure 4.5: Cm vs C_L plot from XFLR5. Cm = 0 at C_L = 0.6 (gray curve), Cm = 0 at C_L = 0.3 (black curve).
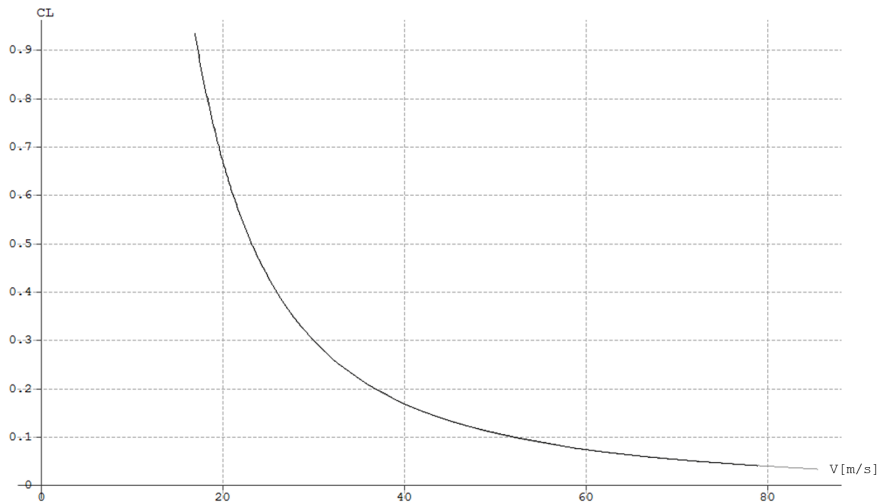
Figure 4.6: Cm vs V plot from XFLR5

4.3 Propulsion

This section shows the results and selection of the propeller's two geometric parameters, the diameter with variable pitch value for each flight condition.

Figure 4.7 plots with the resulting blade pitch throughout multiple diameters. One can see that the bigger the disc diameter, the better is hover lift efficiency, H. However, when reached a point where the current demand is very high for the chosen diameter, or the motor ω_{motor} is too low to be efficiently operating, the efficiency starts to drop rapidly.

The diameter of 50 cm is the best in hover because it produces the same thrust with less power due to having lower disc loading than the competing smaller disc diameters. The 40 cm disc diameter has much higher disc loading and consequently, less H. Although, it demands less electric current, it also increases the voltage needed to operate, resulting in more electric power demand for the same thrust produced and consequently, in lower H.

The results indicated that the best disc diameter is between 40-50 cm. The results in the hover condition compared with the cruise flight condition will make it possible to define the design disc diameter value.
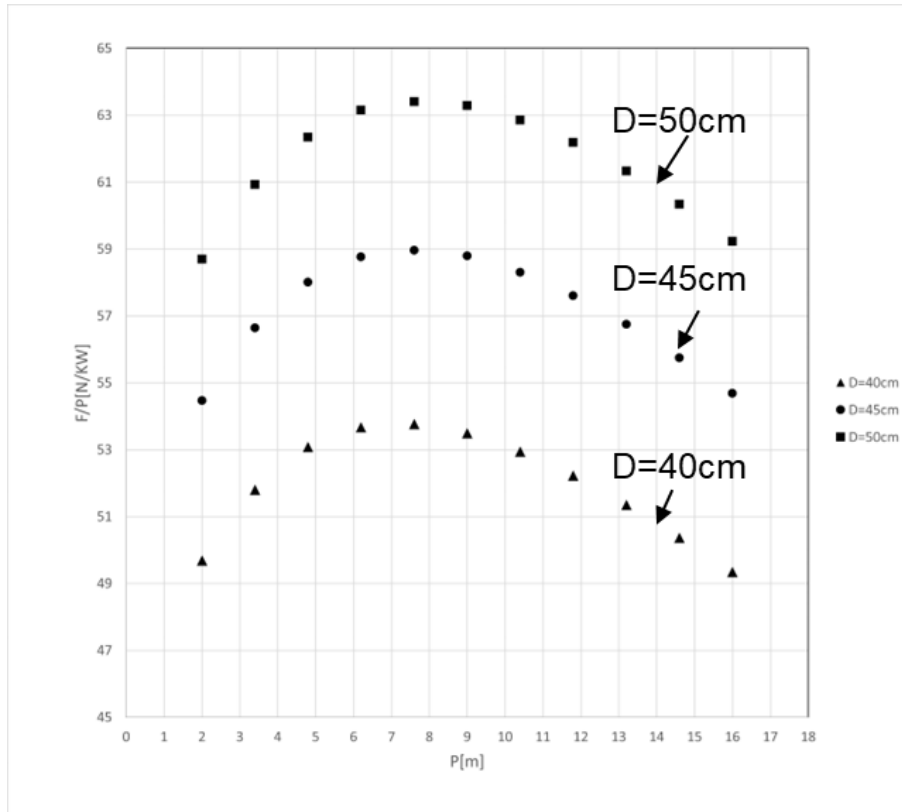
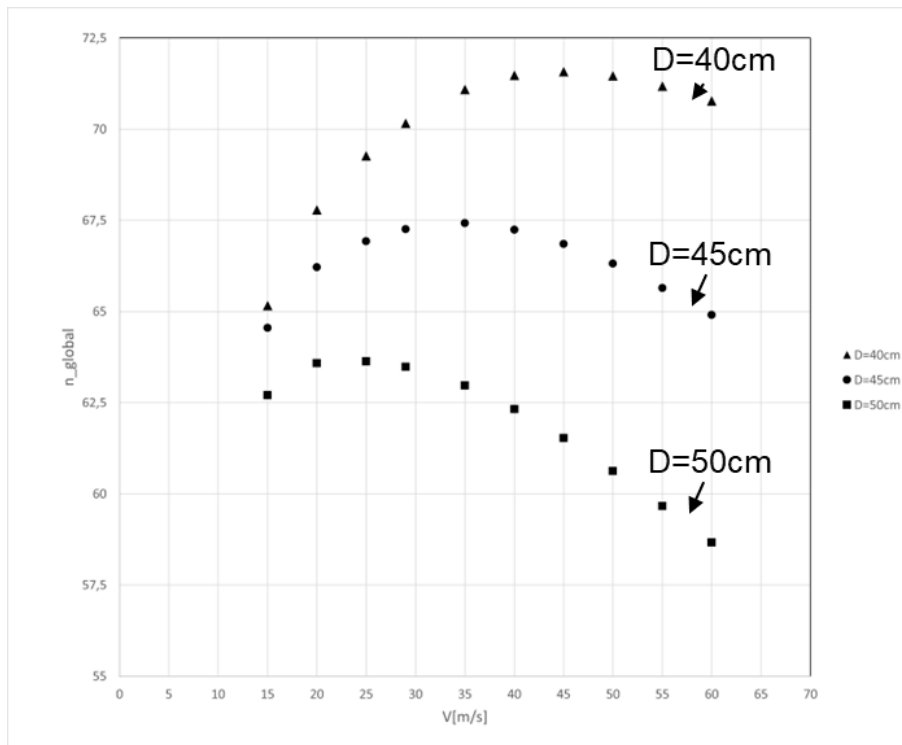Figure 4.7: Hover Lift Efficiency vs Blade Pitch in different diameters

Figure 4.8: Global efficiency in cruise vs Airspeed in different diameters

Figure 4.8 shows that using the 45 cm diameter is the best compromise considering both scenarios. Despite that, the 40 cm results in the best disc diameter for high speed

in cruise. Though, the 45 cm disc diameter is the best compromise for both modes of operation because it has the best hover efficiency and makes the cruise global efficiency peak close to the aircraft objective function peak design value, v_{cr} 30m/s (see Figure 4.8). Hereafter, the 45 cm disc diameter is selected, thus, the final aircraft performance predictions were made with this value.

Figure 4.9 describes the aircraft required thrust in cruise flight in relation of the airspeed. The minimum point reflects the speed for the lowest thrust demand, which is the cruise speed of the aircraft and on this stage, $\left(\frac{L}{D}\right)_{max}$.
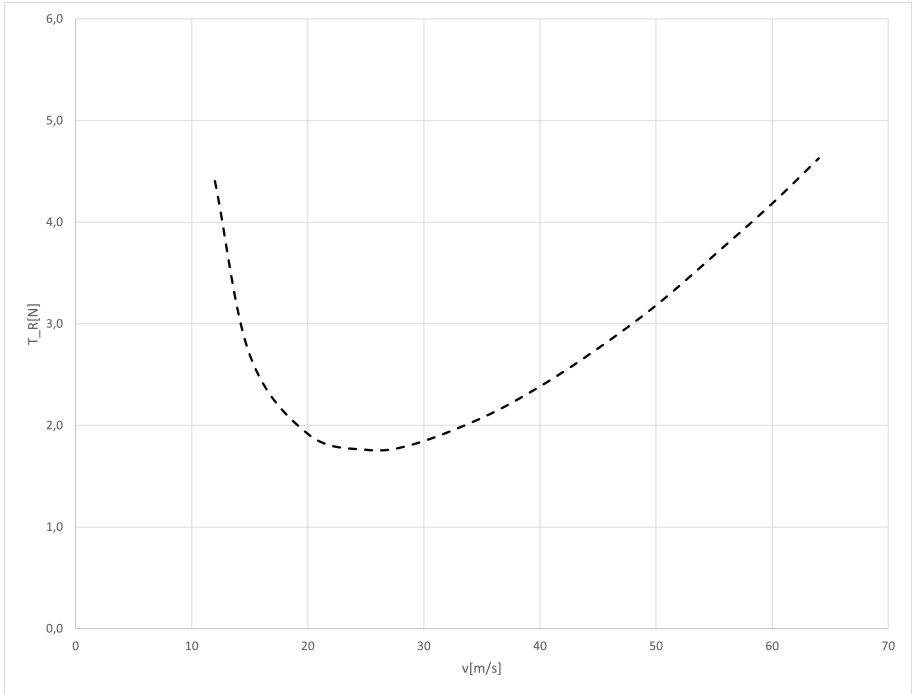
Figure 4.9: Thrust required

Figure 4.10 describes the thrust generated by the propulsion system available in function of airspeed when the throttle is set to maintain the maximum motor electric current $I = 69A$, corresponding to a climb flight condition. It demonstrates that the propeller of airspeed when the throttle is set to maintain the maximum motor electric current I=69A, corresponding to a climb flight condition. Thrust as airspeed increases, the corresponding global propulsive efficiency versus airspeed in shown in Figure 4.12, where it is observed that when maximum throttle is used, the global efficiency almost not affected by the height current draw but the corresponding airspeed increases significantly.

Figure 4.10: Thrust Available

Figure 4.11 shows the blade pitch in the function of airspeed for the required thrust. The variable pitch trend is to increase to a coarse pitch values as the airspeed increases. An increase of the motor RPM was also observed as the airspeed increases.

Figure 4.11 also represents the variable blade pitch for available thrust at different speeds assuming I_{max}. Interesting results for the pitch behaviour are plotted. Since airspeed gra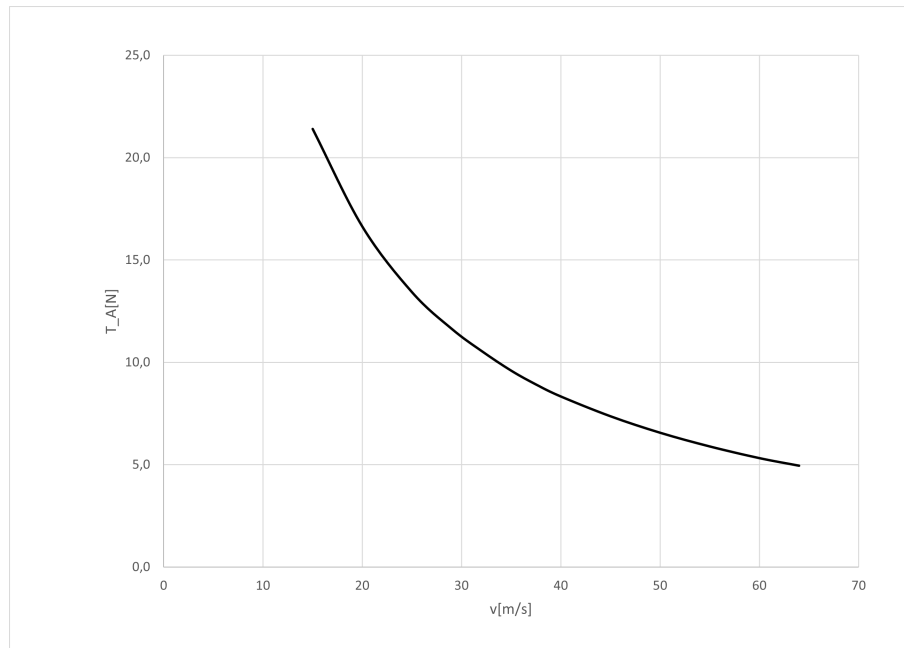dually increases, the pitch becomes more coarse, whereas, the ω_{motor} are observed in the data to gradually decrease. It is observed that to draw the maximum current, the throttle is greatly increased in comparison with the required thrust condition, thus, the pitch for maximum available thrust is smaller for the same airspeed because the motor is turning at much higher ω_{motor} .

The variable pitch in both flight conditions increases with the airspeed (see Figure 4.11), for the cruise condition with a parabolic behaviour, whereas, the climb condition presents a linear behaviour. For the cruise condition, the pitch increases as a parabolic function with values of pitch higher than the counterpart, thus, presenting a coarse pitch. Nevertheless, no significant change occurs in the global efficiency of the propeller system.
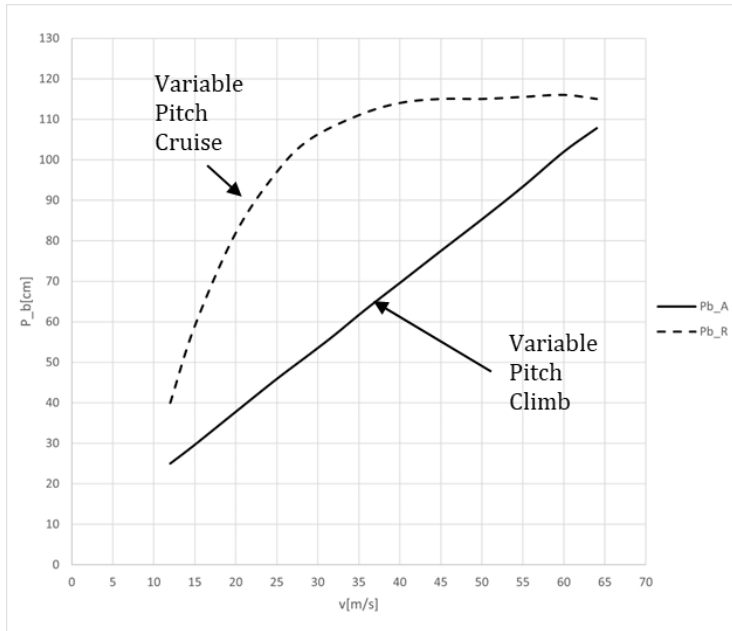
Figure 4.11: Variable pitch in cruise and climb vs airspeed

Figure 4.12 shows the global efficiency for both conditions of flight, cruise and climb with a fixed pitch and variable pitch propeller. In the cruise condition the shaft power is significantly lower than in the climb condition, and so is the thrust, hence, the power output formula is ($\eta_p T V_\infty = P$). The fixed pitch curves assume a $P_b = 22\ cm$, which is the highest value for a fixed pitch propeller to operate in all flight conditions (VTOL,cruise, climb) effectively . The variable pitch propeller is optimized to iterated until reaches the maximum n_{global} for each airspeed, which results in having the variable pitch propeller presenting better n_{global} values in all airspeeds.
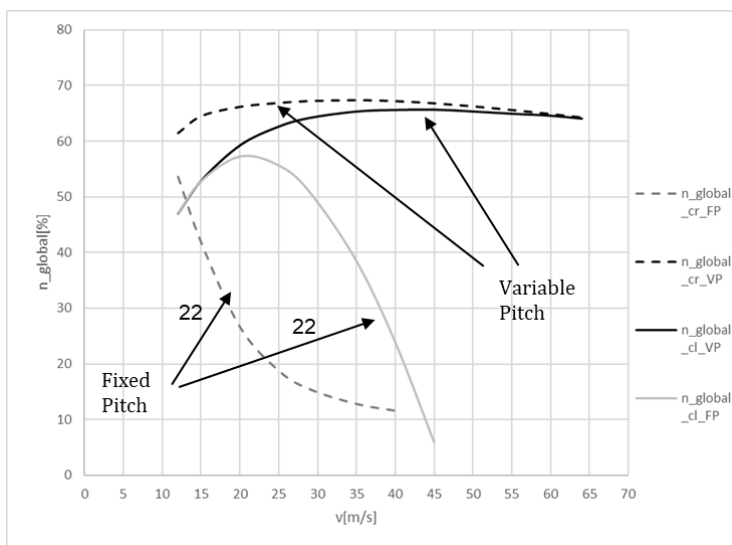
Figure 4.12: Global efficiency in cruise and climb vs airspeed

66

4.4 Performance

The performance study seeks parameters such as the ROC, Endurance, and others. These parameters are the product of aerodynamics and propulsion interactions, defining the mission profile for this aircraft.

At this point it is defined that the aircraft in cruise has about a 29 m/s airspeed with the variable ptich propeller. That is achieved arranging the tail deflection of 1.5, so that neutral point occurs at 0.3. This corresponds to an increase of the global efficiency of the propeller since the 45 cm disc diameter is better around this airspeed (see Figure 4.8).

The ROC study will determine the points where the climb for the fixed wing flight mode condition is effective. The ROC for the propeller fixed-wing mode is formulated in Equation (4.1) as:

$$ROC = \frac{(F - D)V_\infty}{W_{MTOM}} \tag{4.1}$$

The available and required thrust in the airspeed range is plotted in Figure 4.13 for both fixed ptich and variable pitch propeller. The fixed pitch propeller generates more thurst at lower speed since is limit to fine pitch values. The $P_b = 7cm$ represents the case where the best pitch for hover lift performance is adopted.

The fine pitch propeller cannot increase above 22 cm because the blades encounters themselves close to stall. As the airspeed increases, the pitch set becomes insufficient to generate thrust at higher speeds with a 45 cm diameter. Hence, a variable pitch propeller proves superior because it can operate effectively in all speed ranges. Solid dark curve in Figure 4.13 represents the variable pitch propeller optimize for best η_{global}, while the interrupted curve is the case where is to select pitches that maximize the thrust available for all airspeeds. And is shown that with a variable pitch propeller optimize to maximized T_a, does achieved best T_a results in all speed range, and that also reflects in better rate of climb as follows (see Figure 4.15).

Figure 4.14 represents both curves of power required and power available of the aircraft with a fixed ptich and variable pitch propeller. For a propeller-driven aircraft, the thrust comes from the power output produced by the engine torque at a given rotational speed(ω), then $Q\omega = FV/\eta_p$. For the variable pitch propeller the power available is considerably superior to the power required in fixed-wing mode at minimum airspeed. Since the power demand for hovering and climbing in VTOL mode is so great, the motor selected has enough power to operate smoothly in those stages. As airspeed increases, the power available has a small variation until the airspeed surpasses the max speed of around 64

m/s. By then, the required power is increasing sharply with airspeed due to the parasite drag value increase.
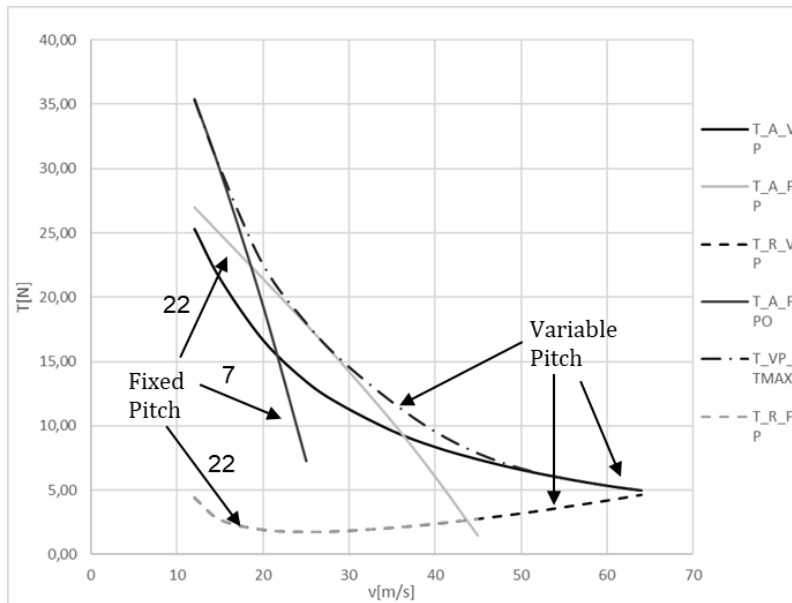
Figure 4.13: Thrust Required and Thrust Available
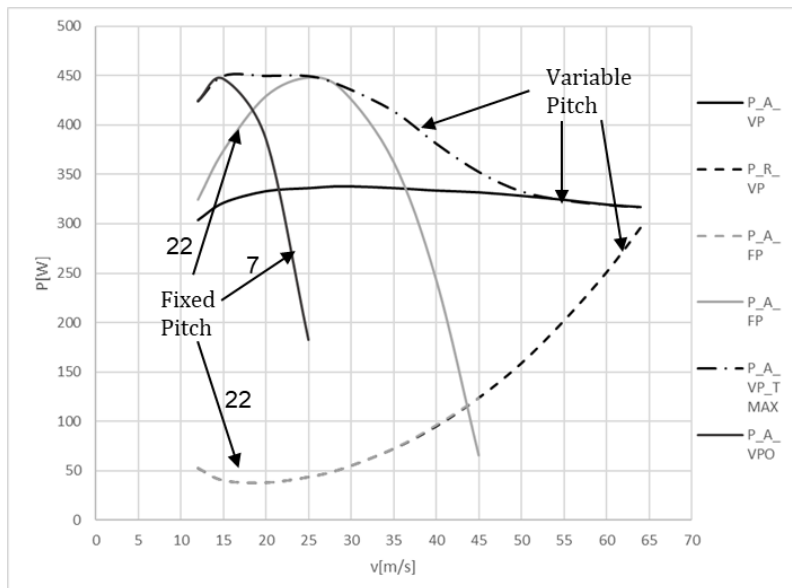
Figure 4.14: Power Required and Power Available

The rate of climb in fixed-wing mode is presented in Figure 4.15 for the fixed pitch propeller and variable pitch propeller. The variable pitch propeller optimized for maximum η_{global} has better result as speeds increases resulting in the best rate of climb near 3 m/s at 20 m/s airspeed. The fixed-pitch cases presents better results due to having a finer pitch, which generates more thrust at lower airspeeds but cannot operate at higher airspeed because they lose thrust and suffer "windmilling". The interrupted curve presents the best rate of climb for all range of speeds since was optimized for maximum T_a.

68
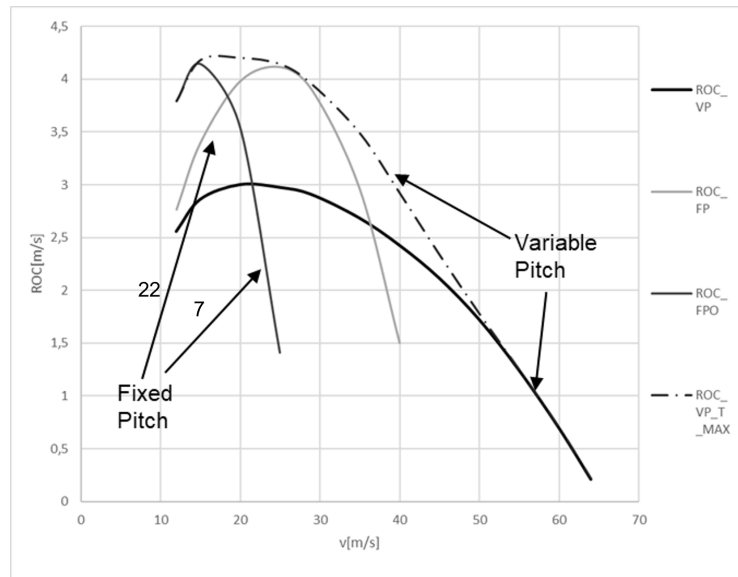
Figure 4.15: ROC Performance
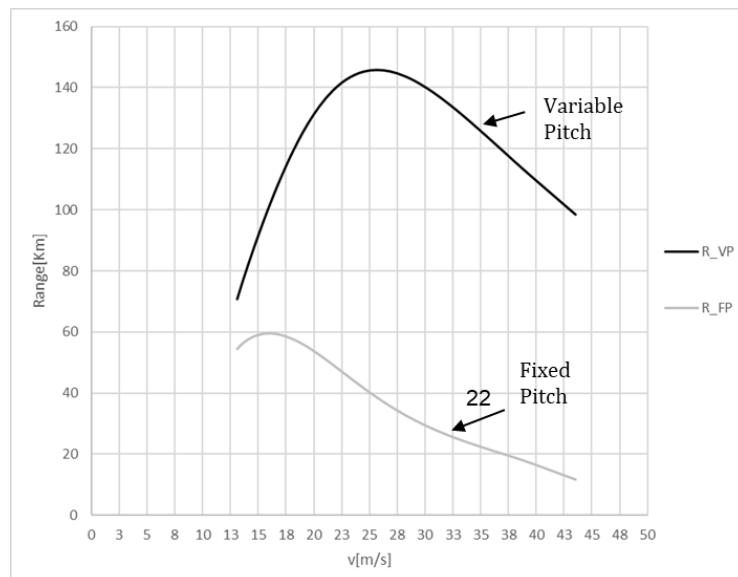
Figure 4.16: Range performance

The range is crucial for mission planning and performance, especially for a transport role aircraft. An electric aircraft does not lose weight during flight, and the power available does not change with flight altitude. Therefore, estimating this performance parameter for this project requires a different approach than the general for engine propeller-driven aircraft. The battery is the sole energy reservoir for the flight, thus, Equation (2.20) is proposed for the range estimation presented in Figure 4.16 for this electric aircraft. About 67 % of battery is reserve for cruise condition with a variable pitch propeller, moreover, battery fraction for cruise, $\frac{m_{batcr}}{m_{MTOM}}$ = 0.267.The maximum range for the variable pitch propeller occurs at 25 m/s cruise, very close to the minimum drag condition. That happens because the lift to drag ratio changes significantly among the speed ranges and does a higher contribution into the range equation when compared to the global efficiency, which

at speeds between 20 to 40 m/s does not vary considerably(see Appendix A.15). Figure 4.16 also shows that the variable pitch propeller is always better in range in all airspeeds because is optimized for best pitch for every airspeed.

4.4.1 Mission Profile

Generally, the mission profile definition is one of the first steps for a conceptual and preliminary design of the aircraft. However, designs such as eVTOL are unique and present features unclear in the initial phase. Furthermore, the designed aircraft's goal is concept testing, thus, they are no defined initial requirements for a specific mission profile and the main driving objective was prototype cost. Hence, in this dissertation, the mission profile is proposed as the last step when the aircraft was already sized. The mission profile is then adapted for the aircraft's capabilities and limitations.

At this stage, performance parameters such as range, cruise speed, global efficiency, and power are introduced for planning the flight phases of the mission profile.

The Flight phases must fulfil the policies demanded by civil aviation authorities to operate. Since 2021, EASA has introduced recommendations for the national civil aviation authorities to operate UAM aircraft. The aircraft designed follows open category A3 in EASA regulations which means uncertified aircraft below 25 kg that must fly far from people, and be operated by a certified remote pilot[101]. Further operation requirements from 14 CFR Part 107 include[102]:
-Keep your drone within line of sight. If you use First Person View or similar technology.
-Fly during daylight (30 minutes before official sunrise to 30 minutes after official sunset, local time) or in twilight if your drone has anti-collision lighting
-The maximum allowable altitude is 122 m above the ground, higher if your drone remains within 400 feet of a structure. Maximum airspeed is 100 mph (44.44 m/s).

The aircraft design fulfils the operational restrictions since its cruise speed is slightly above 27.78 m/s, and the ceiling is considered slightly above 100 m. Therefore after observing the restrictions from civil aviation authorities the pathline to follow for the mission planning is clear.

Table 4.2 gives the time for each operation phase and energy consumption. E_{con} is the consumption over each flight stage , E_{con}/E_{conT} is the ratio between the E_{con} and the total energy consumption of the mission. A battery mass corresponding to 40 % of the aircraft MTOM, is assumed.

The eVTOL presents two flight modes, over which the VTOL mode consumes a significant amount of energy despite the short time it operates. That is the case since it is responsible to lift and sustain the aircraft until the transition phase. Hereafter, the fixed-wing mode relies upon the wing for lift, and from climb to cruise condition occurs a huge drop in consumption since the aircraft is flying in a steady condition at optimised cruise speed and global efficiency for the propulsion system. A decrease in endurance results in

a higher relative energy consumption at the VTOL mode shortening the range, and the battery mass fraction for the fixed wing flight mode diminishes.

Table 4.2: Mission Profile Flight Phases and Energy Consumption

| Mission	Description	t[s]	E_{con}[J]	E_{con}[Wh]	E_{con}/E_{conT}
0	TAXI: Multi-rotor	10.00	13937.3682	3.871	0.805
1	Hovering : Multi-rotor	40.00	55749.4727	15.486	3.221
	Climb : Multi-rotor	24.07	39554.6342	10.987	2.285
2	Climb : Fixed wing	10.32	11799.6335	3.278	0.682
3	Cruise	5051.2	835246.9	232.013	48.255
4	Descent : Fixed wing	10.32	1705.964	0.474	0.099
5	Descent: Multi-rotor	24.07	33551.26	9.320	1.938
	Hovering : Multi-rotor	40.00	55749.4727	15.486	3.221
6	TAXI: Multi-rotor	10.00	13937.3682	3.871	0.805
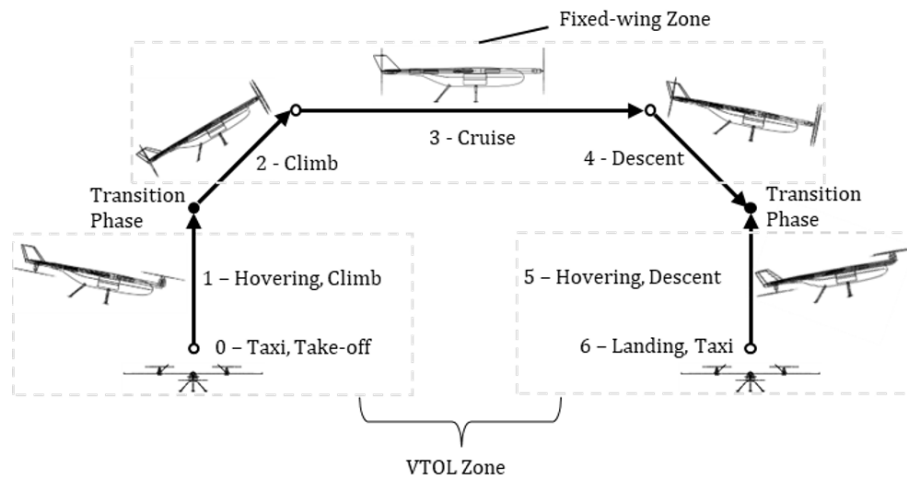
Figure 4.17: Mission Profile

Chapter 5

Conclusion

5.1 Overview

This dissertation encompass the development of an eVTOL prototype considering 10kg as MTOW. This prototype aims to be used as a proof of concept for further developments.

A morphing aerofoil model allowed to predict that the optimal wing mean chord value is too small to implement due to structural limitation of the wing. A 150 % higher than the optimal mean chord was selected as a suitable compromise with a penalty of 13 % lower value in the optimal objective function.

The propulsion system capable of operating efficiently in all flight modes was found to have a variable pitch propeller. Based on the propulsion system global efficiency optimization, the implemented method showed that since blade pitch increases from the VTOL mode to the fixed-wing mode significantly, a fixed-pitch propeller could not work efficiently in all modes in the same mission profile.

The morphing aerofoil is replaced by Selig 9000 in the later stage of the design to perform aerodynamics and static stability simulations in XFLR5. The static margin is 10 % when the C.G is placed around 32 % of the mean aerodynamic chord. Hence, the designed eVTOL is capable of efficient cruise flight in airplane mode with a cruise speed in the range 22 m/s for C_L=0.6 to 29 m/s for C_L=0.3.

The MTOM is 10 kg, with a battery mass fraction close to 0.4. By reducing battery mass fraction for more payload room results in a higher objective function. That does not significantly decrease the range when less than 5 % of its value is taken.

The mission profile shows that most energy consumption occurs in the VTOL mode for short time flights (below 25 minutes mark) with E_S = 120 Wh/kg, nevertheless, for the planned mission 67 % of the battery is spent for 82 minutes in cruise flight and a total 87 minutes of flight time and range close to 148 km.

5.2 Future Work

In this dissertation although its objectives were achieved, a detailed design is still missing. For a start, the transition flight phase needs to be studied for a clear understanding of how the aircraft behaves throughout such phase in terms of aerodynamics and stability,

propulsion for further optimization. Furthermore, the thrust tilt mechanism designed in CAD must be 3D printed and tested for structural integrity, effectiveness and reliability for the approval of the design.

The propulsion system must accommodate a variable pitch mechanism with significant pitch changes through the flight modes. Thus, such a mechanism must be developed and tested to compare with the results of the predictions realized in the present work. Moreover, the blade sizing of such a propeller must have its geometry related to the variable pitch mechanism efficient results and flight operation. The possibility of performing autorotation can be studied for this propulsion configuration as the aircraft could benefit from this safety feature and increase the aircraft survivability.

Bibliography

[1] D. M. D. Francesco, "Is the Urban Air Mobility Industry ready for Take-Off?" 2019. [Online]. Available: https://www.airborne.com/urban-air-mobility-the-rise-of-evtol-vehicles/ 1, 28

[2] B. L. Hinman, "Hang in There: Why Hovering Matters in eVTOL Design," 2019. [Online]. Available: https://brian-is-flyin.medium.com/hang-in-there-why-hovering-matters-in-evtol-design-bf60aa5b69db 1

[3] M. an Markets, "eVTOL Aircraft Market by Lift Technology (Vectored Thrust, Multirotor, Lift plus Cruise), Propulsion Type (Fully Electric, Hybrid Electric, Hydrogen Electric), System, Range, MTOW, Mode of Operation, Application, and Region-Forecast to 2030," Tech. Rep., 2021. [Online]. Available: https://www.marketsandmarkets.com/Market-Reports/evtol-aircraft-market-28054110.html?gclid=Cj0KCQiA0eOPBhCGARIsAFIwTs4ajja7eKnKPETiZ50jGhoBe0VZ9kZnlpXkPFJ2SrRGNsLAfDJUxVIaApXbEALw{_}wcB 1, 29

[4] R. H. Barnard and D. R. Philpott, *Aircraft Flight: A Description of the Physical Principles of Aircraft Flight*, 4th ed. Pearson Education Limited, 2004. [Online]. Available: http://books.google.com/books?id=t9UI9UBZ2PgC{&}pgis=1 5, 11

[5] J. D. Anderson, *Fundamentals of Aerodynamics (6th edition)*, 2011, vol. 1984, no. 3. xi, 6

[6] D. F.Anderson and S. Eberhardt, *Understanding Flight*. McGraw-Hill, 2001. 6, 11

[7] Y. B. Liang, L. X. Zhang, E. X. Li, X. H. Liu, and Y. Yang, "Design considerations of rotor configuration for straight-bladed vertical axis wind turbines," *Advances in Mechanical Engineering*, vol. 2014, 2014. xi, 6

[8] E. Prof and D. Scholz, "Project Department of Automotive and Aeronautical Engineering Mach number , relative thickness , sweep and lift coefficient of the wing - An empirical investigation of parameters and equations Author : Simona Ciornei," *Engineering*, 2005. 7

[9] D. Ma, Y. Zhao, Y. Qiao, and G. Li, "Effects of relative thickness on aerodynamic characteristics of airfoil at a low Reynolds number," *Chinese Journal of Aeronautics*, vol. 28, no. 4, pp. 1003–1015, 2015. [Online]. Available: http://dx.doi.org/10.1016/j.cja.2015.05.012 xi, 7

[10] V. Brederode, *Aerodinâmica Incompressível : Fundamentos*. 7

[11] Selig, Donovan, and Fraser, "Airfoils at Low Speeds," pp. 1–408, 1989. 8

[12] P. B. S. Lissaman, "Low-reynolds-number airfoils," *Fluid Mechanics*, pp. 223–239, 1983. xi, 8

[13] B. Vanderhoydonck, G. Santo, J. Vierendeels, and J. Degroote, "Optimization of a Human-Powered Aircraft Using Fluid–Structure Interaction Simulations," *Aerospace*, vol. 3, p. 26, aug 2016. xi, 8

[14] D. Raymer, "Aircraft Design: A Conceptual Approach, Sixth Edition," *Aircraft Design: A Conceptual Approach, Sixth Edition*, 2018. xi, 9, 10, 11, 12, 13, 44, 47, 48, 49

[15] M. H.Sadraey, *Aircraft Performance - An Engineering Approach*, 2017. 11

[16] M. Drela, "Wing Taper Considerations," Tech. Rep., 2006. [Online]. Available: https://ocw.mit.edu/courses/aeronautics-and-astronautics/16-01-unified-engin eering-i-ii-iii-iv-fall-2005-spring-2006/systems-labs-06/spl8a.pdf 11

[17] T. Hamid, M. Z. Babar, M. Uzair, and M. Hussain, *Pitch Attitude Control for an Aircraft using Linear Quadratic Integral Control Strategy*, nov 2019. xi, 12

[18] M. V.Cook, "Flight Dynamics Principles," in *Flight Dynamics Principles*, 2nd ed. Butterworth-Heinemann, 2007, pp. 1–491. 12

[19] S. Gudmundsson, *The Anatomy of the Tail*, 2014. 12

[20] W. Johnson, *Helicopter Theory*, 1994. 14, 16, 23

[21] J. Seddon and S. Newman, *Basic Helicopter Aerodynamics*, 3rd ed. Jonh Wiley & Sons,Ltd., 2011. 14

[22] W. Johnson, *Rotorcraft aeromechanics*, 2006, vol. 9781107028. xi, xv, 14, 15, 16, 22

[23] S. Gudmundsson, *The Anatomy of the Propeller*, 2014. 16, 17

[24] "basicpropellerprinciples @ avstop.com." [Online]. Available: http://avstop.com /ac/flighttrainghandbook/basicpropellerprinciples.html xi, 16

[25] J. A. Guerrero, R. Lozano, G. Romero, D. Lara-Alabazares, and K. C. Wong, "Robust control design based on sliding mode control for hover flight of a mini tail-sitter unmanned aerial vehicle," *IECON Proceedings (Industrial Electronics Conference)*, pp. 2342–2347, 2009. xi, 18

[26] J. D. Anderson, *Aircraft Performance and Design*, 1999. 19

[27] H. Martin, "Electric Flight - Potential and Limitations," *AVT-209 Workshop, Lisbon*, pp. 1–30, 2012. xi, 19, 27, 29, 34

[28] Avstop, "straightandlevelflight2 @ avstop.com." [Online]. Available: http://avstop.com/ac/flighttrainghandbook/straightandlevelflight2.html xi, 20

[29] E.Torenbeek and H.Wittenberg, *Flight Physics.* Springer, 2008. 21

[30] A. Murrieta Mendoza, "Vertical and lateral flight optimization algorithm and missed approach cost calculation," Ph.D. dissertation, jun 2013. xi, 21

[31] M. D. Maisel, D. J. Giulianetti, and D. C. Dugan, "The History of The XV-15 Tilt Rotor Research Aircraft: From Concept to Flight," *NASA Special Publication 4517*, p. 194, 2000. xi, 23, 24, 25

[32] J.-p. Harrison, "The Cierva Autodynamic Rotor," p. 66, 2015. xi, 23, 24

[33] John Watkinson, *Art of the Helicopter.* Elsevier Butterworth-Heinemann, 2004. xi, 24

[34] A. Bacchini and E. Cestino, "Electric VTOL configurations comparison," *Aerospace*, vol. 6, no. 3, mar 2019. 24, 31

[35] Verticalmag, "AW609 crash: final report points to oscillations and flight control laws," 2017. [Online]. Available: https://verticalmag.com/news/aw609-crash-final-report-points-oscillations-flight-control-laws/ 25

[36] ——, "Fourth AW609 (AC4) moved to Italy from Leonardo's Philadelphia facility," 2021. [Online]. Available: https://verticalmag.com/press-releases/fourth-aw609-ac4-moved-to-italy-from-leonardos-philadelphia-facility/ xi, 25

[37] R. Vepa, *Electric aircraft dynamics:A Systems Engineering Approach*, 1st ed., 2020. 26, 28

[38] T. Placke, R. Kloepsch, S. Dühnen, and M. Winter, "Lithium ion, lithium metal, and alternative rechargeable battery technologies: the odyssey for high energy density," *Journal of Solid State Electrochemistry*, vol. 21, no. 7, pp. 1939–1964, 2017. 26, 28

[39] G. Benveniste, H. Rallo, L. Canals Casals, A. Merino, and B. Amante, "Comparison of the state of Lithium-Sulphur and lithium-ion batteries applied to electromobility," *Journal of Environmental Management*, vol. 226, no. October 2017, pp. 1–12, 2018. [Online]. Available: https://doi.org/10.1016/j.jenvman.2018.08.008 26, 28

[40] V. Beggi, L. Loisel, and X.-T. Nguyen, "Microgrid in USTH campus : Architecture and Power Management Strategies," Ph.D. dissertation, jul 2018. xi, 27

[41] T. M.Letcher, Ed., *Improved , Sustainable and Clean Options for our Planet Third Edition*, 3rd ed. Elsevier, 2020. 27

[42] A. Dobley, *Catalytic Batteries.* Elsevier B.V., 2013. [Online]. Available: http://dx.doi.org/10.1016/B978-0-444-53880-2.00001-6 28

[43] M. an Markets, "Helicopters Market by Point Of Sale (OEM, Aftermarket), OEM Type (Light, Medium, Heavy), OEM Application (Military, Civil & Commercial), OEM Number of Engine, OEM Component & System, Aftermarket by Component & System, and Region - Global Forecast to 2025," Tech. Rep., 2020. [Online]. Available: https://www.marketsandmarkets.com/Market-Reports/helicopters-market-253467785.html 28

[44] A. S. Media, "SPECIAL FEATURE: GLOBAL HELICOPTER MARKET OVERVIEW YE2018," 2018. [Online]. Available: https://www.asianskymedia.com/news/2019/1/30/special-feature-global-helicopter-market-overview-part-1 xi, 29

[45] R. Dive, "EVTOL Aircraft Market Report," p. 329, 2020. [Online]. Available: https://www.researchdive.com/166/evtol-aircraft-market xi, 30

[46] W. Tan, Y. Li, Y. Miao, and H. Lv, "The analysis of airworthiness issues influence to the development of tiltrotor aircraft," *Procedia Engineering*, vol. 80, pp. 602–608, 2014. [Online]. Available: http://dx.doi.org/10.1016/j.proeng.2014.09.116 30

[47] M. Hirschberg, "The Electric VTOL Revolution," *Vertical Flight Society*, no. March, pp. 1–34, 2018. xi, 31

[48] "www.opener.aero." [Online]. Available: https://www.opener.aero xi, 32, 33

[49] "kittyhawk.aero." [Online]. Available: https://kittyhawk.aero/heaviside/ xi, 32, 33

[50] "lilium.com." [Online]. Available: https://lilium.com/jet 32, 33

[51] "Lilium @ evtol.news." [Online]. Available: https://evtol.news/lilium/ xi, 32, 33

[52] "www.xtiaircraft.com." [Online]. Available: https://www.xtiaircraft.com/{#}Air-mobility-revolutionized 33

[53] "www.jobyaviation.com." [Online]. Available: https://www.jobyaviation.com/news/ 33

[54] "joby-s4 @ evtol.news." [Online]. Available: https://evtol.news/joby-s4 33

[55] "wisk.aero." [Online]. Available: https://wisk.aero/aircraft/ 33

[56] "bell-nexus-4ex@ evtol.news." [Online]. Available: https://evtol.news/bell-nexus-4ex/ 33

[57] "bell-nexus @ www.bellflight.com." [Online]. Available: https://www.bellflight.com/products/bell-nexus 33

[58] "maker @ www.archer.com." [Online]. Available: https://www.archer.com/maker 33

[59] "www.beta.team." [Online]. Available: https://www.beta.team/aircraft/ 33

[60] "alia-250-electric-vertical-take-off-and-landing-evtol-aircraft @ www.aerospace-technology.com." [Online]. Available: https://www.aerospace-technology.com/projects/alia-250-electric-vertical-take-off-and-landing-evtol-aircraft/ 33

[61] Ö. Dündar, M. Bilici, and T. Ünler, "Design and performance analyses of a fixed wing battery VTOL UAV," *Engineering Science and Technology, an International Journal*, vol. 23, no. 5, pp. 1182–1193, 2020. [Online]. Available: https://www.sciencedirect.com/science/article/pii/S2215098619316489 34

[62] M. Tyan, N. V. Nguyen, S. Kim, and J.-W. Lee, "Comprehensive preliminary sizing/resizing method for a fixed wing – VTOL electric UAV," *Aerospace Science and Technology*, vol. 71, pp. 30–41, 2017. [Online]. Available: https://www.sciencedirect.com/science/article/pii/S1270963817300871 34

[63] KapetAir, "KapetAir VTOL UAV," 2022. [Online]. Available: https://diydrones.com/profiles/blogs/kapetair-vtol-test-flight 34

[64] A. Ascend, "ASCEND," 2020. [Online]. Available: https://www.ssass.co.za/alti-ascend 34

[65] Q. Systems, "Trinity F90Plus mapping drone," pp. 1–36, 2021. [Online]. Available: https://www.quantum-systems.com/project/trinityf90plus-mapping-drone/ 34

[66] D. VOLT, "HELIPLANE HYBRID VTOL UAV v.2," Tech. Rep., 2019. [Online]. Available: https://metatronus.com/wp-content/uploads/2019/10/heliplane{_}brochure{_}2019{_}en.pdf 34

[67] Q. Systems, "VECTOR The 2in1 Vertical Take-off Reconnaissance UAV," 2022. [Online]. Available: https://www.quantum-systems.com/project/vector/ 34

[68] A. I. C. Ltd, "CW-20." [Online]. Available: https://www.aerotechinnovation.co.nz/cw15 34

[69] C. Technologies, "SENTAERO v2BVLOS," Tech. Rep. [Online]. Available: https://censystech.com/wp-content/uploads/2021/04/Censys-Sentaero-v2BVLOS-Flyer.pdf 34

[70] L. Landle Technology Co., "Ct-05 Vtol Fixed Wing Hybrid Drone Uav For Surveillance And Inspection." [Online]. Available: http://www.industrial-drone.com/ct-05-vtol-fixed-wing-hybrid-drone-uav-for-surveillance-and-inspection-6492416.html 34

[71] Geo-matching, "SatLab SLA-2 VTOL Drone Mapping." [Online]. Available: https://geo-matching.com/uas-for-mapping-and-3d-modelling/sla-2-vtol-drone-mapping 34

[72] T. Systems, "EOS C VTOL," Tech. Rep. [Online]. Available: https://threod.com/wp-content/uploads/2020/06/EOS-C-VTOL-UAS-datasheet.pdf 34

[73] A. R. Serrano, "Design methodology for hybrid (VTOL + Fixed Wing) unmanned aerial vehicles," *Aeronautics and Aerospace Open Access Journal*, vol. 2, no. 3, 2018. 34

[74] U. RC., "Swift Full Composite Material VTOL Mapping UAV." [Online]. Available: https://unmannedrc.com/products/swift-full-compiste-material-vtol-mapping-uav 34

[75] Electrofluidsystems, "PLASMA (FALCON) FLYER 1.11 / 6 - 11 kg MTOW," 2021. [Online]. Available: https://www.electrofluidsystems.com/Systems/Unmanned-Systems 34

[76] D. Engr, "eVTOL Electric Vertical Take-Off and Landing UAV for survey can carry Lidar with 7 KGS for 1.5 hours endurance." [Online]. Available: https://www.droneassemble.com/product/evtol-electric-vertical-take-off-and-landing-uav-for-survey-can-carry-lidar-with-7-kgs-for-1-5-hours-endurance/ 34

[77] ——, "electric vtol vertical takeoff aircraft 3 meter Angel Wings fixed wing KIT for UAV building." [Online]. Available: https://www.droneassemble.com/product/electric-vtol-vertical-takeoff-aircraft-3-meter-angel-wings-fixed-wing-kit-for-uav-building/ 34

[78] A. I. C. Ltd, "CW -20." [Online]. Available: https://www.aerotechinnovation.co.nz/cw-20 34

[79] Xi'an MH Electronics And Technology, "VTOL Drone With Military Thermal Imager." [Online]. Available: https://www.alibaba.com/product-detail/VTOL-Drone-With-Military-Thermal-Imager{_}60649986865.html 34

[80] A. Solutions, "Tron F90+ 2KG payload in a fixed-wing PPK capable UAV, ideal for LiDAR use cases," 2020. [Online]. Available: https://aeca-solutions.com/tronf90plus/ 34

[81] M. Ball, "New Long-Endurance VTOL Drone Released," 2021. [Online]. Available: https://www.unmannedsystemstechnology.com/2021/06/penguin-b-long-endurance-vtol-drone-released/ 34

[82] U. Systems, "PD-2 Unmanned Aerial System One stop UAS solution for military and civil applications," Tech. Rep. [Online]. Available: https://www.unmannedsystemstechnology.com/wp-content/uploads/2016/06/PD{_}2.pdf 34

[83] Wingtra, "WingtraOne GEN II drone Technical specifications," Zurich, Tech. Rep. [Online]. Available: https://wingtra.b-cdn.net/wp-content/uploads/Wingtra-Technical-Specifications.pdf 34

[84] Foxtech, "FOXTECH Great Shark 330 VTOL," 2022. [Online]. Available: https://www.foxtechfpv.com/foxtech-great-shark-330-vtol.html 34

[85] H. M. de Almeida, "Induced Drag Reduction with a Wing Tip Tail Configuration," Ph.D. dissertation, Universidade da Beira Interior, 2018. [Online]. Available: https://ubibliorum.ubi.pt/handle/10400.6/8738 40

[86] A. Deperrois, "xflr5," 2021. [Online]. Available: http://www.xflr5.tech/xflr5.htm 40

[87] M. Drela, "XFOIL," 2013. [Online]. Available: https://web.mit.edu/drela/Public /web/xfoil/ 40

[88] NASA, "About OpenVSP," 2012. [Online]. Available: http://openvsp.org/learn.sh tml 41

[89] B. R. Gyles, "Prop Selector." [Online]. Available: http://www.hoppenbrouwer-h ome.nl/ikarus/software/propselector.htm 41

[90] E.P.Lesley, "NACA Technical Notes No.698," 1931. [Online]. Available: http: //acversailles.free.fr/documentation/08{~}Documentation{_}Generale{_}M {_}Suire/Helice/Rapports{_}NACA/NACA{_}TN{_}698.pdf 41

[91] M. Ângelo and R. Silvestre, "Aero @ UBI-HPA-1 The Great Human Powered Aircraft English Channel Crossing Race 2022," no. October 2021, 2022. xii, 41, 42, 45, 47

[92] Hoerner, *Fluid- Dynamic Drag*, 1965. 43

[93] S. Gudmundsson, *Aircraft Drag Analysis*, 2014. 43

[94] G. Fujiwara, L. Martinez Stefanini, and O. Silvares, "Design of a human-powered aircraft applying multidisciplinary optimization method," *SAE Technical Papers*, vol. 7, no. September, 2013. 43

[95] G. E. Dorrington, "Drag of spheroid-cone shaped airship," *Journal of Aircraft*, vol. 43, no. 2, pp. 363–371, 2006. 43, 44

[96] F. Götten, M. Havermann, C. Braun, M. Marino, and C. Bil, "Improved form factor for drag estimation of fuselages with various cross sections," *Journal of Aircraft*, vol. 58, no. 3, pp. 549–561, 2021. 44

[97] F. N. Espíndola and E. Aeron, "Design of a Long Range Wing Solution for the Fixed Wing UAS30 Platform," Ph.D. dissertation, Universidade da Beira Interior, 2020. xii, 48

[98] Paul E. Pusher and Jonh P.Campbell, "NACA REPORT No. 823," no. 823, pp. 1–21. [Online]. Available: https://ntrs.nasa.gov/api/citations/19930091901/do wnloads/19930091901.pdf 48

[99] AeroToolbox, "Horizontal and Vertical Tail Design," 2017. [Online]. Available: https://aerotoolbox.com/design-aircraft-tail/ 49

[100] N. LIU, Z. CAI, Y. WANG, and J. ZHAO, "Fast level-flight to hover mode transition and altitude control in tiltrotor's landing operation," *Chinese Journal of Aeronautics*, vol. 34, no. 1, pp. 181–193, 2021. [Online]. Available: https://doi.org/10.1016/j.cja.2020.09.041 49

[101] EASA, "Easy Access Rules for Unmanned Aircraft Systems (Revision from September 2021)," 2021. [Online]. Available: http://eur-lex.europa.eu/, 70

[102] FAA, "small-unmanned-aircraft-systems-uas-regulations-part-107 @ www.faa.gov," 2020. [Online]. Available: https://www.faa.gov/newsroom/small-unmanned-aircraft-systems-uas-regulations-part-107 70

Appendix A

Appendix

This appendix includes information and data about the motor, empty mass model, wing sizing, aircraft Computer Aided Design(CAD), extra propulsion graphs.

A.1 Motor

Figure A.1: AXI 2835/10 GOLD LINE V2 LONG

Table A.1: Motor Specifications

Electric Motor	AXI GOLDLINE 2835/10 V2 LONG Brushless Outrunner Motor
Mass$[g]$	257
$kV[rpm/V]$	690
$R[\Omega]$	0.027
$I_0[A]$	2.8
$I_{max}[A]$	69
$P_{max}[W]$	1190
Shaft Diameter$[mm]$	5
Can Diameter$[mm]$	35
Lenght$[mm]$	75,5
Cost $[EUR]$	142

A.2   Empty Mass Model Parameters

Table A.2: Empty mass parameters values

Parameters	
$m_{ref}[kg]$	0.3
$m_{systems}[kg]$	2
$b_{ref}[m]$	0.2
$c_{ref}[m]$	1.4
e_b	1.2
e_c	1.2

A.3   Wing Sizing

Figure A.2: Wing Parametric Study Spreadsheet

|	MTOM[kg]	m_systems[kg]	V_inf[m/s]	c_mean[m]	b[m]	W_TO[N]	Oswald Factor	m_asa[kg]	_fuse+emp[kg]	m_empty[kg]	n_container[kg]	m_pay[kg]	m_pay*C_L/C	C_L	C_L/C_D	D[N]	CD_i	C_D0	C_D
-	10	2	61,548	0,1975	2,14	98,067	0,80	0,6572	0,49098	3,1482	6,8518	2,8518	21,445	0,1	7,520	13,041	0,0003672	0,012931	0,01330
1	10	2	49,043	0,1975	2,14	98,067	0,80	0,6572	0,49098	3,1482	6,8518	2,8518	30,116	0,1575	10,560	9,286	0,0009109	0,014003	0,01491
2	10	2	41,976	0,1975	2,14	98,067	0,80	0,6572	0,49098	3,1482	6,8518	2,8518	37,060	0,215	12,995	7,546	0,0016974	0,014847	0,01654
3	10	2	37,285	0,1975	2,14	98,067	0,80	0,6572	0,49098	3,1482	6,8518	2,8518	42,470	0,2725	14,892	6,585	0,0027268	0,015571	0,01830
4	10	2	33,881	0,1975	2,14	98,067	0,80	0,6572	0,49098	3,1482	6,8518	2,8518	46,532	0,33	16,317	6,010	0,0039989	0,016226	0,02022
5	10	2	31,267	0,1975	2,14	98,067	0,80	0,6572	0,49098	3,1482	6,8518	2,8518	49,442	0,3875	17,337	5,656	0,0055139	0,016837	0,02235
6	10	2	29,177	0,1975	2,14	98,067	0,80	0,6572	0,49098	3,1482	6,8518	2,8518	51,393	0,445	18,021	5,442	0,0072717	0,017421	0,02469
7	10	2	27,457	0,1975	2,14	98,067	0,80	0,6572	0,49098	3,1482	6,8518	2,8518	52,565	0,5025	18,432	5,320	0,0092723	0,017990	0,02726
8	10	2	26,009	0,1975	2,14	98,067	0,80	0,6572	0,49098	3,1482	6,8518	2,8518	53,116	0,56	18,635	5,265	0,0115157	0,018551	0,03007
9	10	2	24,768	0,1975	2,14	98,067	0,80	0,6572	0,49098	3,1482	6,8518	2,8518	53,183	0,6175	18,—	5,265	0,0140019	0,019110	0,03311
10	10	2	23,690	0,1975	2,14	98,067	0,80	0,6572	0,49098	3,1482	6,8518	2,8518	52,878	0,675	18,542	5,289	0,0167310	0,019673	0,03640
11	10	2	22,741	0,1975	2,14	98,067	0,80	0,6572	0,49098	3,1482	6,8518	2,8518	52,293	0,7325	18,337	5,348	0,0197028	0,020244	0,03995
12	10	2	21,898	0,1975	2,14	98,067	0,80	0,6572	0,49098	3,1482	6,8518	2,8518	51,502	0,79	18,059	5,430	0,0229175	0,020827	0,04374
13	10	2	21,142	0,1975	2,14	98,067	0,80	0,6572	0,49098	3,1482	6,8518	2,8518	50,562	0,8475	17,730	5,531	0,0263750	0,021426	0,04780
14	10	2	20,459	0,1975	2,14	98,067	0,80	0,6572	0,49098	3,1482	6,8518	2,8518	49,519	0,905	17,364	5,648	0,0300753	0,022043	0,05212
15	10	2	19,839	0,1975	2,14	98,067	0,80	0,6572	0,49098	3,1482	6,8518	2,8518	48,408	0,9625	16,975	5,777	0,0340185	0,022683	0,05670
16	10	2	19,272	0,1975	2,14	98,067	0,80	0,6572	0,49098	3,1482	6,8518	2,8518	47,256	1,02	16,571	5,918	0,0382044	0,023350	0,06155
17	10	2	18,750	0,1975	2,14	98,067	0,80	0,6572	0,49098	3,1482	6,8518	2,8518	46,083	1,0775	16,159	6,069	0,0426332	0,024046	0,06668
18	10	2	18,269	0,1975	2,14	98,067	0,80	0,6572	0,49098	3,1482	6,8518	2,8518	44,905	1,135	15,746	6,228	0,0473048	0,024776	0,07208
19	10	2	17,823	0,1975	2,14	98,067	0,80	0,6572	0,49098	3,1482	6,8518	2,8518	43,733	1,1925	15,335	6,395	0,0522192	0,025543	0,07776
20	10	2	17,409	0,1975	2,14	98,067	0,80	0,6572	0,49098	3,1482	6,8518	2,8518	42,574	1,25	14,929	6,569	0,0573764	0,026353	0,08373
21	10	2	17,021	0,1975	2,14	98,067	0,80	0,6572	0,49098	3,1482	6,8518	2,8518	41,436	1,3075	14,530	6,749	0,0627765	0,027210	0,08999
22	10	2	16,659	0,1975	2,14	98,067	0,80	0,6572	0,49098	3,1482	6,8518	2,8518	40,322	1,365	14,139	6,936	0,0684193	0,028120	0,09654
23	10	2	16,319	0,1975	2,14	98,067	0,80	0,6572	0,49098	3,1482	6,8518	2,8518	39,235	1,4225	13,758	7,128	0,0743050	0,029088	0,10339
24	10	2	15,999	0,1975	2,14	98,067	0,80	0,6572	0,49098	3,1482	6,8518	2,8518	38,176	1,48	13,387	7,326	0,0804335	0,030123	0,11056
25	10	2	15,697	0,1975	2,14	98,067	0,80	0,6572	0,49098	3,1482	6,8518	2,8518	37,147	1,5375	13,026	7,529	0,0868048	0,031230	0,11804
26	10	2	15,411	0,1975	2,14	98,067	0,80	0,6572	0,49098	3,1482	6,8518	2,8518	36,146	1,595	12,675	7,737	0,0934189	0,032420	0,12584
27	10	2	15,141	0,1975	2,14	98,067	0,80	0,6572	0,49098	3,1482	6,8518	2,8518	35,174	1,6525	12,334	7,951	0,1002759	0,033702	0,13398
28	10	2	14,884	0,1975	2,14	98,067	0,80	0,6572	0,49098	3,1482	6,8518	2,8518	34,230	1,71	12,003	8,170	0,1073756	0,035088	0,14246
29	10	2	14,640	0,1975	2,14	98,067	0,80	0,6572	0,49098	3,1482	6,8518	2,8518	33,313	1,7675	11,681	8,395	0,1147182	0,036592	0,15131
30	10	2	14,407	0,1975	2,14	98,067	0,80	0,6572	0,49098	3,1482	6,8518	2,8518	32,420	1,825	11,368	8,626	0,1223036	0,038229	0,16053
31	10	2	14,186	0,1975	2,14	98,067	0,80	0,6572	0,49098	3,1482	6,8518	2,8518	31,551	1,8825	11,064	8,864	0,1301318	0,040018	0,17015
32	10	2	13,974	0,1975	2,14	98,067	0,80	0,6572	0,49098	3,1482	6,8518	2,8518	30,704	1,94	10,767	9,108	0,1382028	0,041981	0,18018
33	10	2	13,771	0,1975	2,14	98,067	0,80	0,6572	0,49098	3,1482	6,8518	2,8518	29,877	1,9975	10,477	9,360	0,1465167	0,044145	0,19066
34	10	2	13,577	0,1975	2,14	98,067	0,80	0,6572	0,49098	3,1482	6,8518	2,8518	29,068	2,055	10,193	9,621	0,1550733	0,046540	0,20161
35	10	2	13,391	0,1975	2,14	98,067	0,80	0,6572	0,49098	3,1482	6,8518	2,8518	28,273	2,1125	9,914	9,892	0,1638728	0,049206	0,21308
36	10	2	13,213	0,1975	2,14	98,067	0,80	0,6572	0,49098	3,1482	6,8518	2,8518	27,491	2,17	9,640	10,173	0,1729151	0,052191	0,22511
37	10	2	13,041	0,1975	2,14	98,067	0,80	0,6572	0,49098	3,1482	6,8518	2,8518	26,718	2,2275	9,369	10,467	0,1822002	0,055552	0,23775
38	10	2	12,876	0,1975	2,14	98,067	0,80	0,6572	0,49098	3,1482	6,8518	2,8518	25,952	2,285	9,100	10,776	0,1917281	0,059365	0,25109
39	10	2	12,717	0,1975	2,14	98,067	0,80	0,6572	0,49098	3,1482	6,8518	2,8518	25,187	2,3425	8,832	11,103	0,2014989	0,063725	0,26522
40	10	2	12,564	0,1975	2,14	98,067	0,80	0,6572	0,49098	3,1482	6,8518	2,8518	24,421	2,4	8,563	11,452	0,2115125	0,068754	0,28027
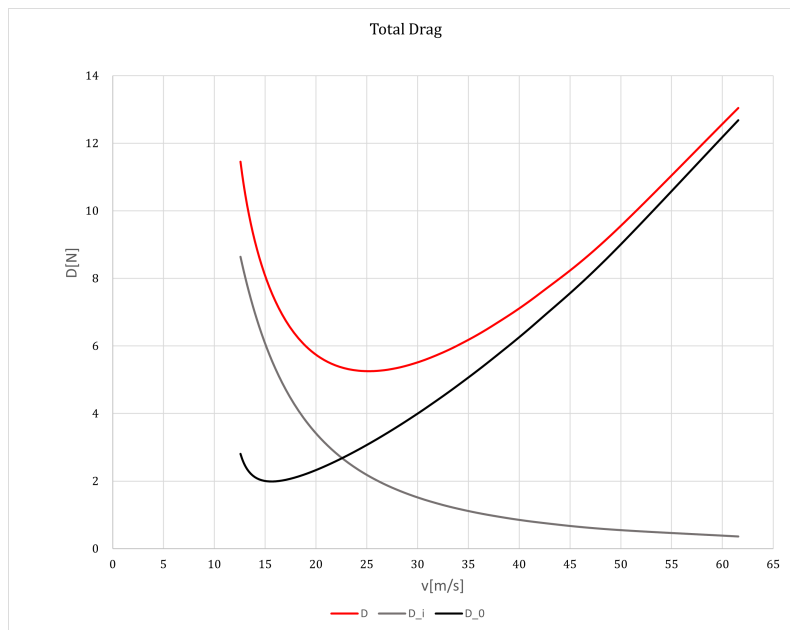
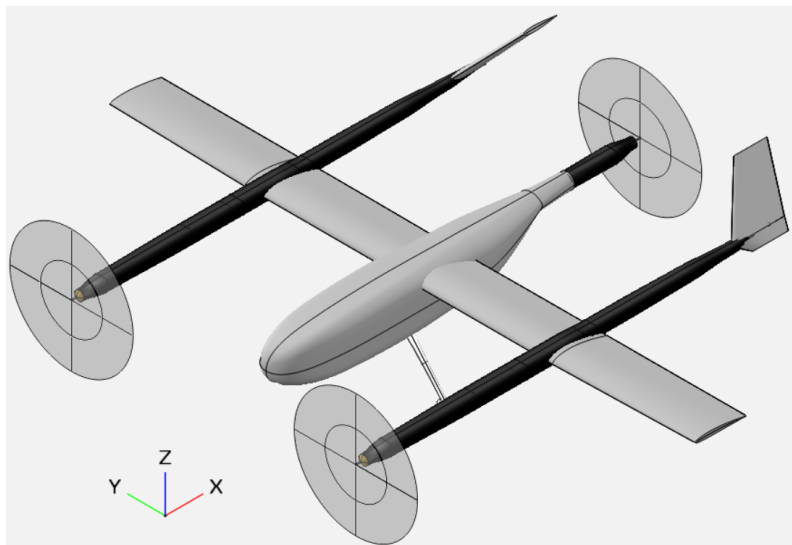Figure A.3: Aircraft Drag

A.4   AeroeVTOL CAD

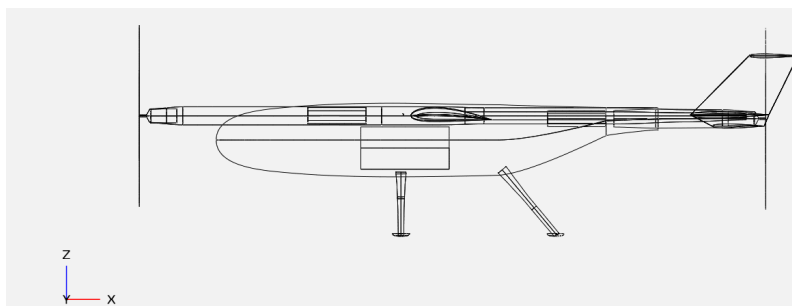Figure A.4: Aero eVTOL UAV ISO View in Fixed-Wing

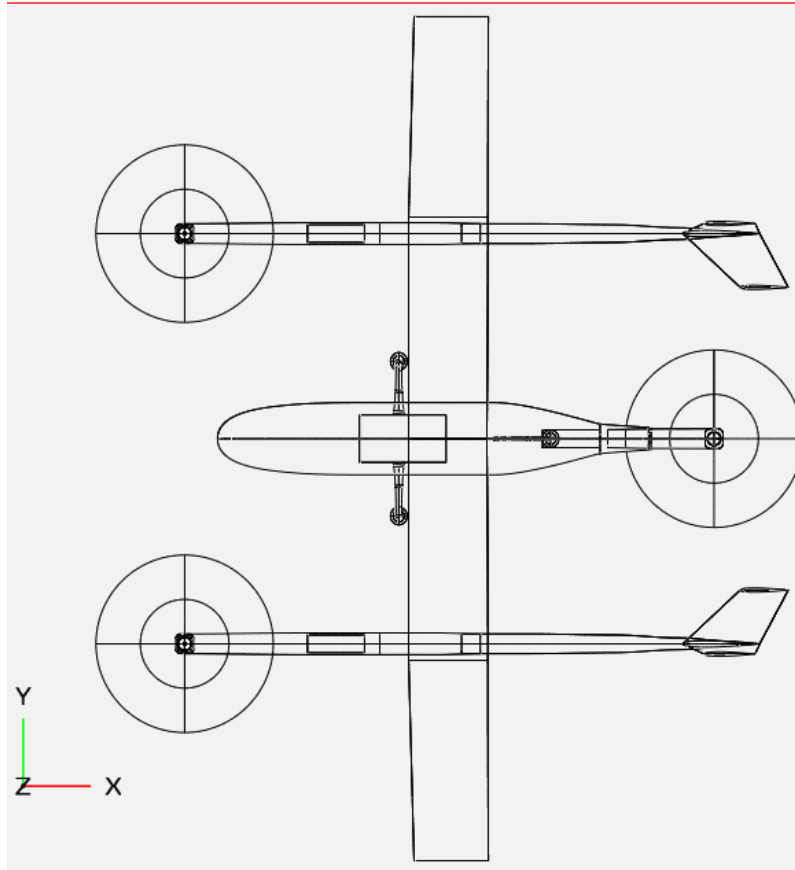Figure A.5: AeroeVTOL UAV Lateral View in Fixed Wing
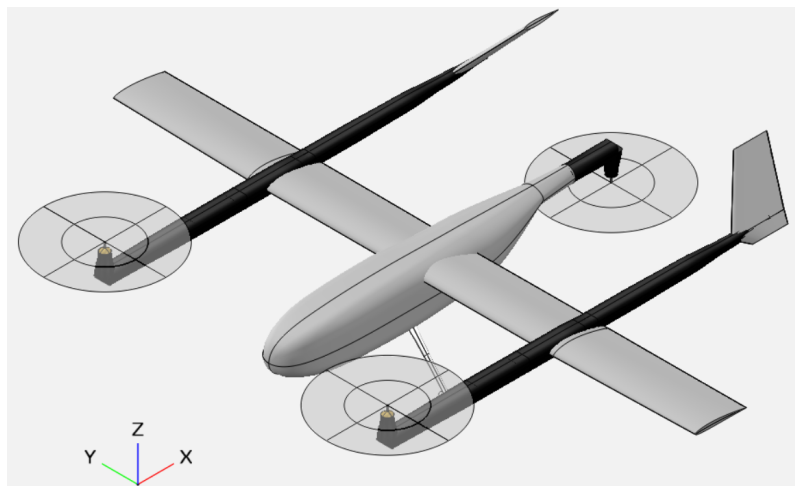
Figure A.6: AeroeVTOL UAV Top View in VTOL

Figure A.7: AeroeVTOL UAV ISO View in VTOL
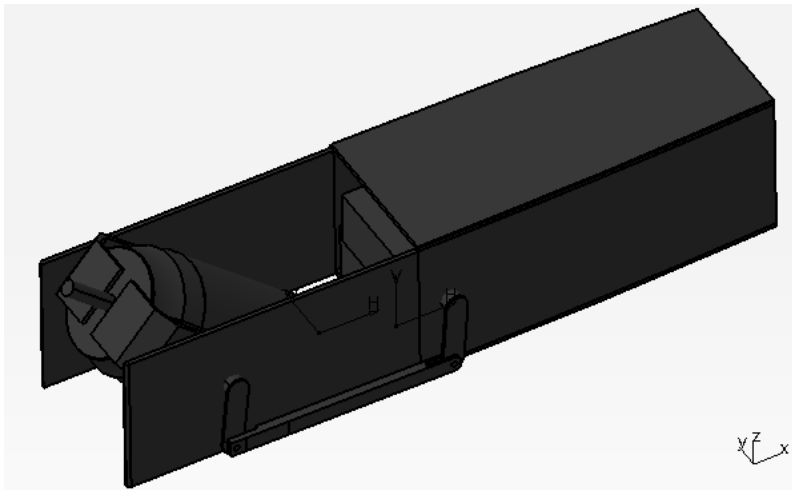
A.5   Tilt Rotor Mechanism CAD
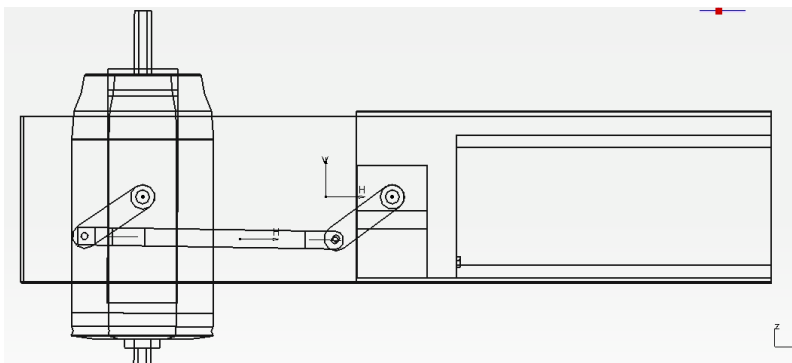

Figure A.8: Tilt Rotor Mechanism ISO View

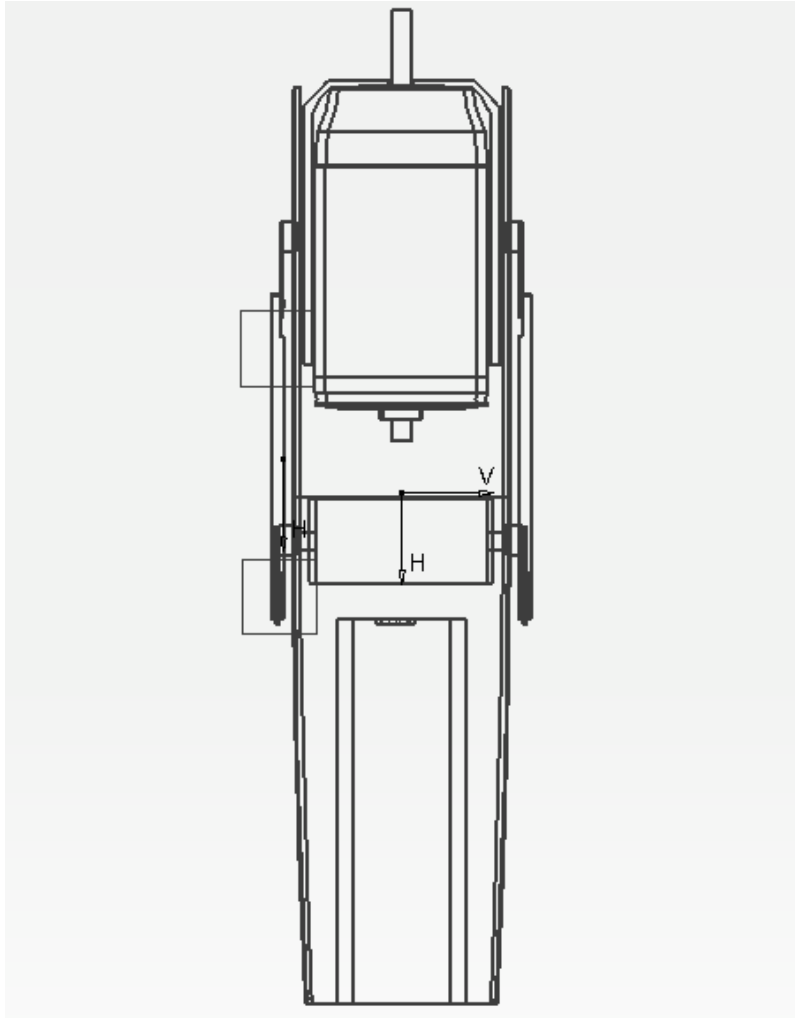Figure A.9: Tilt Rotor Mechanism Lateral View

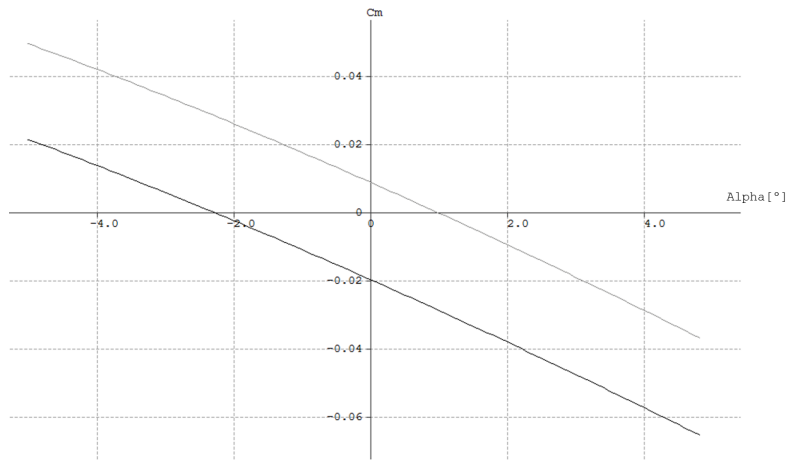Figure A.10: Tilt Rotor Mechanism TOP View

A.6 Static Stability

Figure A.11: C_m vs α plot from XFLR5.Cm = 0 at C_L = 0.6 (gray curve), Cm = 0 at C_L = 0.3 (black curve).
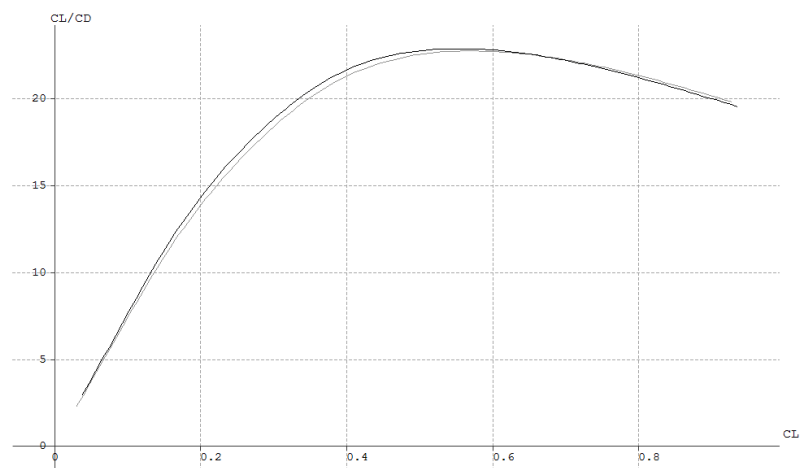
Figure A.12: C_l/C_d vs c_l plot from XFLR5.Cm = 0 at C_L = 0.6 (gray curve), Cm = 0 at C_L = 0.3 (black curve).

A.7   Propulsion Plots and Battery Mass Fraction
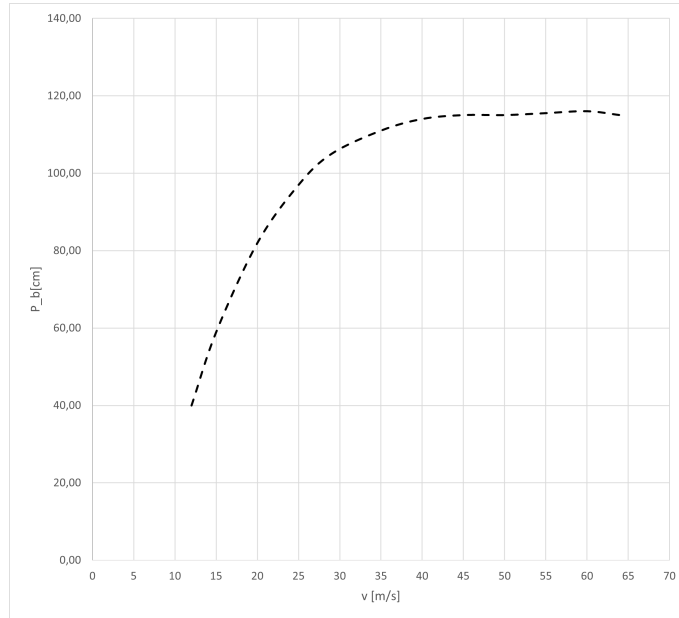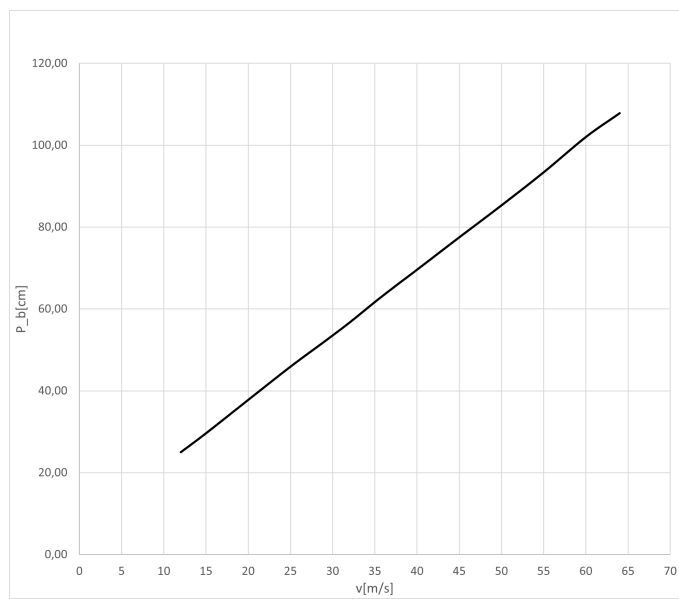

Figure A.13: Blade Pitch Required vs Airspeed
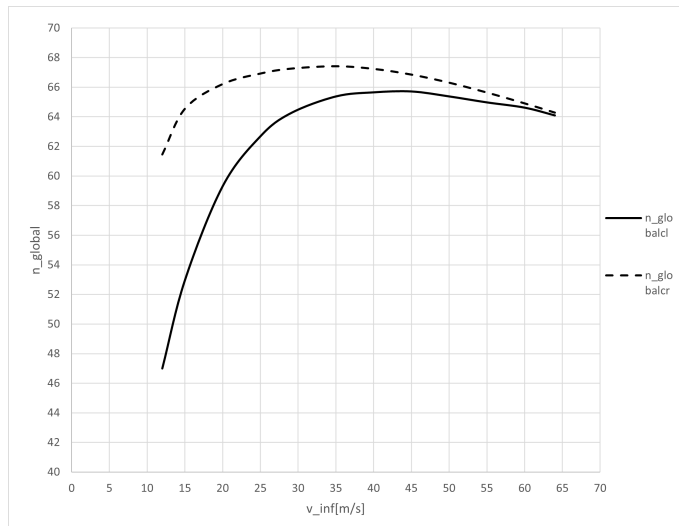

Figure A.14: Blade Pitch Available vs Airspeed

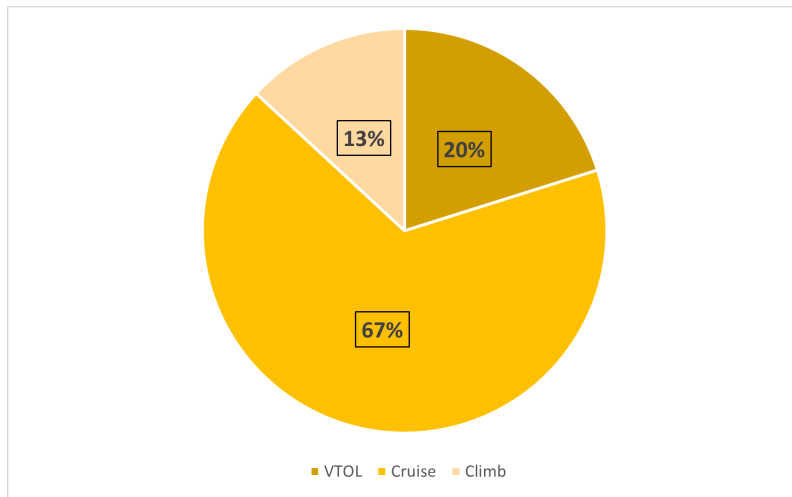Figure A.15: Variable Pitch global efficiency in cruise and climb vs airspeed

Figure A.16: Battery Fraction for every flight condition